Plasticity of neuron-OPC synapses, changes in OPC intrinsic properties and OPC morphology during development of corpus callosum.

Dissertation

zur Erlangung des Grades eines
Doktors der Naturwissenschaften

der Mathematisch-Naturwissenschaftlichen Fakultät
und
der Medizinischen Fakultät
der Eberhard-Karls-Universität Tübingen

vorgelegt
von

Bartosz Kula
Mikołów, Poland

2023

Tag der mündlichen Prüfung: 20 November 2023

Dekan der Math.-Nat. Fakultät: Prof. Dr. Thilo Stehle
Dekan der Medizinischen Fakultät: Prof. Dr. Bernd Pichler

1. Berichterstatter: Prof. Dr. Marlies Knipper

2. Berichterstatter: Prof. Dr. Maria Kukley

Prüfungskommission: Prof. Dr. Maria Kukley

Prof. Dr. Ingrid Ehrlich

Prof. Dr. Marlies Knipper

Prof. Dr. Olga Garaschuk

Erklärung / Declaration:

Ich erkläre, dass ich die zur Promotion eingereichte Arbeit mit dem Titel:

„**Plasticity of neuron–OPC synapses, changes in OPC intrinsic properties and OPC morphology during development of corpus callosum.**“

selbständig verfasst, nur die angegebenen Quellen und Hilfsmittel benutzt und wörtlich oder inhaltlich übernommene Stellen als solche gekennzeichnet habe. Ich versichere an Eides statt, dass diese Angaben wahr sind und dass ich nichts verschwiegen habe**.** Mir ist bekannt, dass die falsche Abgabe einer Versicherung an Eides statt mit Freiheitsstrafe bis zu drei Jahren oder mit Geldstrafe bestraft wird**.**

*I hereby declare that I have produced the work entitled „**Plasticity of neuron–OPC synapses, changes in OPC intrinsic properties and OPC morphology during development of corpus callosum.**“, submitted for the award of a doctorate, on my own (without external help), have used only the sources and aids indicated and have marked passages included from other works, whether verbatim or in content, as such. I swear upon oath that these statements are true and that I have not concealed anything. I am aware that making a false declaration under oath is punishable by a term of imprisonment of up to three years or by a fine.*

Tübingen, den ....

Datum / Date ***Unterschrift /Signature***

Contributions

Multiple people contributed to the data acquisition, analyses or writing presented in this work. Their contribution is listed below in detail:

All of the experiments included in this work were designed by me and Dr. Maria Kukley.

There are 44 cells from 27 animals included in the analysis of OPC morphology. Tissue sections containing 37 cells were immunostained and acquired at a confocal microscope by me, 7 cells were immunostained and acquired by Ms. Victoria Wedler. All Neurolucida tracings and subsequent analyses were performed by me.

There are 121 cells from 101 animals included in the analysis of electrophysiological properties of OPCs. I recorded 68 cells, Dr. Ting-Jiun Chen recorded 20 cells, Dr. Balint Nagy recorded 11 cells, Dr. Anahit Hovhannisyan recorded 22 cells. I performed the electrophysiological analysis of all cells with the exception of 20 cells analyzed by Dr. Chen. Dr. Nagy performed the Non-stationary Noise Fluctuation Analyses (NSFA). Igor Pro macros and functions used to perform electrophysiological analyses were written by Dr. Maria Kukley and Dr. Ruxandra Barzan. Additional functions and scripts supplementing those were written by me.

All graphs containing the original data were prepared by me with the exception of Figure 16, panels G1-J prepared by Dr. Balint Nagy and modified by me.

All of the statistical comparisons were performed by me.

All of the writing in this work was done by me with the exception of section 3.8 Non-stationary fluctuation analysis (NSFA) in the Materials and Methods written by Dr Balint Nagy and modified by me.

Go where those others went to the dark boundary
for the golden fleece of nothingness your last prize

go upright among those who are on their knees
among those with their backs turned and those toppled in the dust

you were saved not in order to live
you have little time you must give testimony

be courageous when the mind deceives you be courageous
in the final account only this is important

and let your helpless Anger be like the sea
whenever you hear the voice of the insulted and beaten

let your sister Scorn not leave you
for the informers executioners cowards—they will win
they will go to your funeral and with relief will throw a lump of earth
the woodborer will write your smoothed-over biography

and do not forgive truly it is not in your power
to forgive in the name of those betrayed at dawn

beware however of unnecessary pride
keep looking at your clown's face in the mirror
repeat: I was called—weren't there better ones than I

beware of dryness of heart love the morning spring
the bird with an unknown name the winter oak

light on a wall the splendour of the sky
they don't need your warm breath
they are there to say: no one will console you

be vigilant—when the light on the mountains gives the sign—arise and go
as long as blood turns in the breast your dark star

repeat old incantations of humanity fables and legends
because this is how you will attain the good you will not attain
repeat great words repeat them stubbornly
like those crossing the desert who perished in the sand

and they will reward you with what they have at hand
with the whip of laughter with murder on a garbage heap

go because only in this way will you be admitted to the company of cold skulls
to the company of your ancestors: Gilgamesh Hector Roland
the defenders of the kingdom without limit and the city of ashes

Be faithful Go

The Envoy of Mr. Cogito, Zbigniew Herbert

Acknowledgments

First, I would like to thank my dearest Wife for her persistent support, against all odds. I wouldn't have come this far without you.

I would like to thank my Teacher, Dr. Maria Kukley for giving me the opportunity to pursue the doctoral study in her group. We've endured so much bad luck and still pushed through.

I would like to thank Dr. Ingrid Ehrlich for her helpful discussions and Andrea Gall for the patience and support in the early stages of the project.

I would also like to thank all the members of our group: Daniela, Nicole, Anahit, Balint, Ruxandra, Ramazan, and Friederike. Working with you was a joy.

Finally, I would like to thank my parents, my sisters, and my friends. I think I would not make it without their support.

Additionally, I would like to thank Dr. Marlies Knipper for taking the role of the First Reviewer of this Thesis.

Contents

List of Figures

List of Tables

Abstract

Oligodendrocyte precursor cells (OPC) are unique among the glial cells of the CNS due to their synaptic connections with neurons. Those synapses are also formed in white matter where OPC are the major recipients of neuronal inputs driving their proliferation and differentiation into myelinating glia. After the robust wave of myelination in the 2-4 postnatal week OPCs remain in the white matter and retain their connections with neurons. Up to date the properties of those synapses are poorly understood throughout callosal development. In this work we demonstrate, in murine callosal (CC) slices, which components of synaptic strength are altered throughout three distinct stages of callosal development (juvenility, adolescence and adulthood) to offset hyperpolarizing membrane potentials and increasing membrane leakage. We show by which mechanisms synapses transition from short term depression into potentiation and increase in reliability of transmission and signal integration. Moreover, we investigate how those properties are shaped by different patterns of activity. We supplement the electrophysiological results with whole-cell morphological reconstructions to show how the development of myelin and continuous growth of CC shapes the branching of OPC processes. Our electrophysiological results point to similarities in synaptic development between neuronal and neuron-glia synapses while providing the first comprehensive assessment of the properties of OPC synapses within a developmental framework. Our morphological results highlight the remarkable stability of OPC branching pattern, contrasting with the substantial changes in the synaptic input and OPC intrinsic properties.

1. Introduction

1.1 Appearance, distribution and progeny of OPCs

NG2-expressing cells, also known as oligodendrocyte precursor cells (OPCs) or polydendrocytes, are prevalent in the grey and white matter of the central nervous system (CNS), constituting 8-9% of the total cell population in adult white matter and 2-3% of total cells in adult grey matter, as reported by Dawson et al., 2003. This population of glial cells in the brain has been recognized to express the proteoglycan NG2 for over two decades (Levine and Card, 1987; Stallcup and Beasley, 1987). The discovery of synapse-like associations between OPCs and neurons in various areas of the developing and adult CNS brought OPCs into the spotlight (Bergles et al., 2000; Lin and Bergles, 2002; Lin et al., 2005). While significant strides have been made in understanding the development and lineage progression of OPCs, their physiological properties and function in normal and diseased brains remain relatively unexplored.

OPCs can be identified by the expression of the NG2 chondroitin sulphate proteoglycan and alpha receptor for platelet-derived growth factor (PDGF-Rα). Microvascular pericytes also express the NG2 proteoglycan (Ozerdem et al., 2001; Zhu et al., 2008; Hamilton et al., 2010); however, the two cell types have distinct morphologies, with NG2-glia being stellate cells with multiple processes, and pericytes being perivascular cells with two or more primary processes extending along blood vessels (Wigley and Butt, 2009).

Electrophysiological studies indicate that OPCs express a complex set of voltage-gated channels, including tetrodotoxin (TTX)-sensitive sodium channels and various types of potassium channels (Bergles et al., 2000; Chittajallu et al., 2004; Káradóttir et al., 2008; Kukley et al., 2008; Kukley et al., 2010; De Biase et al., 2010; Spitzer et al., 2019). Furthermore, OPCs in grey and white matter areas of the brain express α-amino-3-hydroxyl-5-methyl-4-isoxazole-propionate (AMPA)/kainate and/or γ-aminobutyric acid (GABAA) receptors and receive glutamatergic and/or GABAergic synaptic input from neurons (Bergles et al., 2000; Lin and Bergles, 2002; Lin et al., 2005; Káradóttir et al., 2005; Kukley et al., 2007; Ziskin et al., 2007). It is not clear why neurons have evolved to possess specialized release machinery at specific sites of contact with NG2 glial cells, nor whether neuron-glia synapses are dynamic. Recent studies have begun to investigate potential changes in neuron-glia synapses when OPCs divide or differentiate (Kukley et al., 2008; Kukley et al., 2010; De Biase et al., 2010; Ge et al., 2009).

Currently, it remains unclear at what stage of development the first oligodendroglial progenitors expressing NG2 emerge in the CNS. Several studies suggest that the earliest NG2-positive parenchymal cells arise after E14.5 in mice or E15-E17 in rats (Zhu et al., 2011; Trotter et al., 2010).

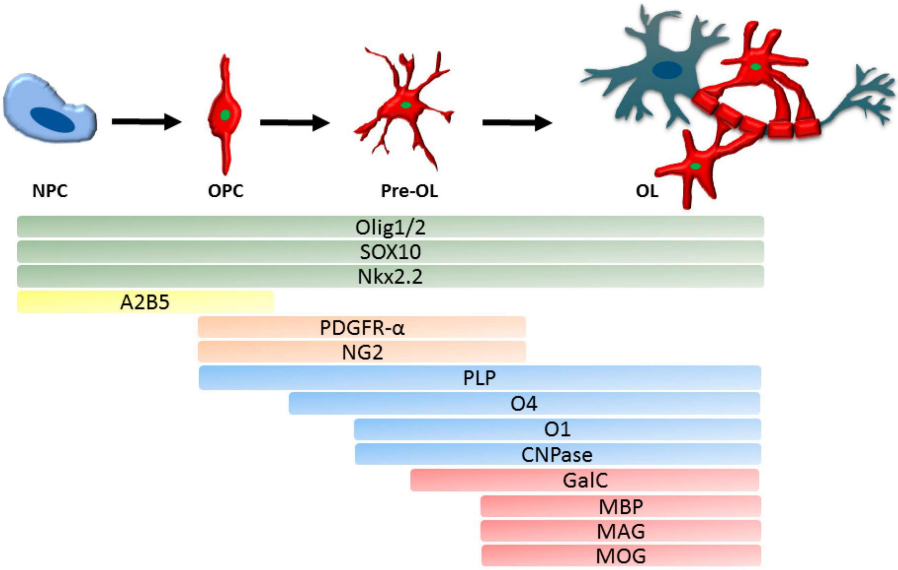

Figure 1. Oligodendroglial lineage markers that correspond to distinct stages of development from neuronal progenitor cells (NPC) to myelinating oligodendrocytes (OL).

A2B5 is expressed by neural progenitor cells, NPC, and oligodendrocyte progenitor cells (OPC) alike. Olig1 and Olig2, along with Sox10 and Nkx2.2, are expressed in all cells of the lineage. OPC and pre-oligodendrocytes (pre-OL) are characterised by PDGFR-α and NG2 expression. During the transition from progenitor to differentiated oligodendrocytes, PLP, O4, O1, and CNPase are expressed. Differentiated, axon-myelinating oligodendrocytes are characterised by myelin protein expression (MBP, MAG, MOG, GalC). NPC: neuronal progenitor cell; OPC: oligodendrocyte progenitor cell; OL: oligodendrocyte; PDGFR-α: platelet-derived growth factor receptor A; NG2: neuron-glial antigen 2; PLP: proteolipid protein; CNPase: 2',3'-Cyclic-nucleotide 3'-phosphodiesterase; MBP: myelin basic protein; MAG: myelin associated glycoprotein; MOG: myelin-oligodendrocyte glycoprotein; GalC: galactocerebroside. Adapted from Kuhn et al., 2019.

Prior to this, NG2 labeling within the CNS is observed in developing capillaries, and no regions derived from the neuroepithelium appear to be stained (Nishiyama et al., 1996; Trotter et al., 2010). All non-vascular NG2-positive cells also express PDGF-Rα. Other research indicates that the earliest oligodendrocyte progenitors are formed in the ventral telencephalon at around E11.5-E12.5 in mice, from the ventricular zone of the medial ganglionic eminence (Tekki-Kessaris et al., 2001; Kessaris et al., 2006). These oligodendrocyte progenitors express PDGF-Rα, but it is unclear whether they are also NG2-positive. In rats, the highest density of OPCs occurs during the first postnatal week. At this point, regional differences in the density of OPCs appear to be less apparent since these cells

uniformly populate the entire CNS (Nishiyama et al., 1996). From the second postnatal week, the number of NG2-immunoreactive cells begins to decline, although both NG2 and PDGF-Rα molecules continue to be expressed into adulthood.

In both the developing and adult brain, OPCs are known to develop into myelinating oligodendrocytes. However, a significant proportion of OPCs fail to differentiate beyond the stage at which they express NG2 and the lipid antigen O4, leading to their persistence in the CNS in an immature form (Dawson et al., 2003; Zhu et al., 2008; Rivers et al., 2008). Despite numerous studies, it is still not well understood whether OPCs are oligodendrocyte precursors with restricted lineage potential or multipotent progenitors.

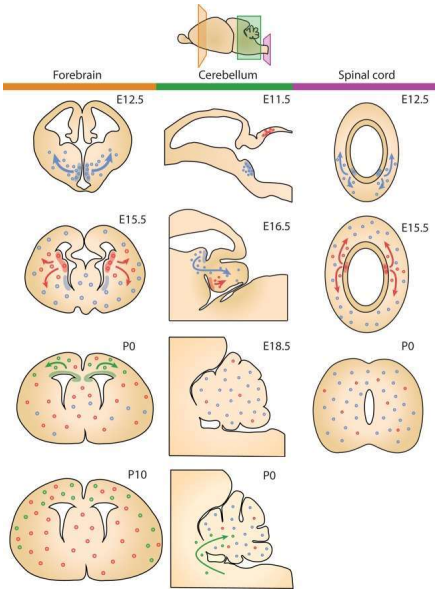

Figure 2. Distinct waves of OPC generation populate various regions of the central nervous system (CNS) during development.
The three panels (left/orange: forebrain; middle/green: cerebellum; right/purple: spinal cord) illustrate different regions of the developing brain. OPCs originating from various niches are represented by differently colored dots (blue = MGE, red = L/CGE, and green = dSVG). The data used to create this schematic were derived from several sources (Fogarty, Richardson, & Kessaris, 2005; Grimaldi, Parras, Guillemot, Rossi, & Wassef, 2009; Hashimoto et al., 2016; Kessaris et al., 2006; Ravanelli & Appel, 2015; Vallstedt, Klos, & Ericson, 2005). Adapted from van Tilborg et al., 2018.

Previous attempts to address the question of the fate of OPCs have reported that these cells (OPC or O-2A progenitors) can generate oligodendrocytes, as well as a number of neurons and/or astrocytes (Belachew et al., 2003; Aguirre and Gallo, 2004; Aguirre et al., 2004; Tamura et al., 2007). Recent advances in Cre-loxP fate mapping have allowed for further evaluation of OPC fate in the mouse CNS, in different transgenic mouse lines in vivo (Dimou et al., 2008; Rivers et al., 2008; Zhu et al., 2008; Zhu et al., 2011; Guo et al., 2009; Kang et al., 2010). These studies largely agree that OPCs are mainly responsible for generation of oligodendrocytes, while some have also reported that

OPCs are the precursors of astrocytes in ventral areas of the brain and spinal cord (Zhu et al., 2008; Guo et al., 2009). Other findings suggest that a limited number of OPCs can differentiate into principal neurons in the ventral forebrain, dorsal cerebral cortex, and hippocampus in postnatal and adult animals (Rivers et al., 2008; Guo et al., 2009; Guo et al., 2010).

However, some investigators have pointed out that OPCs remain committed to the oligodendrocyte lineage in postnatal life and even following neurodegeneration (Kang et al., 2010). Interestingly, the fate of OPCs is likely to be age-dependent, as a recent study has shown that OPCs in the postnatal brain generate only OPCs or oligodendrocytes, whereas OPCs in the embryonic brain generate protoplasmic astrocytes in addition to oligodendrocytes and OPCs (Zhu et al., 2011). Thus, while it is clear that OPCs are the precursors of oligodendrocytes, conclusions about the alternative fate of these cells remain controversial.

The investigation of this issue is complicated by several factors. First of all, NG2 proteoglycan is a surface marker that is lost before the terminal differentiation of the cells (Kukley et al., 2010; Fröhlich et al., 2011). Therefore, it is not possible to define the lineage potential of NG2-expressing cells based solely on NG2 expression, and the use of multiple markers is necessary to identify the types of progeny that OPCs can generate. Second, although Cre-loxP technology has brought many advantages, caution is needed in interpreting the results of Cre-loxP-mediated fate-mapping experiments. Even in transgenic animals designed to express Cre recombinase under a specific promoter, transient expression of Cre recombinase in cells distinct from the lineage of interest is possible, and confirmation of the fate-mapping results with other lineage-tracing methods is always desirable (Fröhlich et al., 2011; Gallo et al., 2008).

The research on fate mapping of OPCs is further complicated by the fact that pericytes also express NG2 proteoglycan and may be labeled by reporter genes in NG2 transgenic strains, leading to potential confusion in the interpretation of data obtained from transgenic strains, especially when taking into account the possible neurogenic potential of pericytes recently reported in vitro. Despite these challenges, further research into the fate of OPCs is necessary to gain a more comprehensive understanding of their role in the development and function of the CNS.

1.2 Morphology of OPCs

NG2 glial cells are a distinct group of cells characterized by a small, polygonal soma of 10-15 μm in size and a multipolar tree of fine processes. The morphology of these cells varies slightly depending on their location within the brain. In areas of grey matter, OPCs typically have a centrally located soma with long, slender primary processes that bifurcate two or more times, giving rise to a symmetrical process field (Bergles et al., 2000; Chittajallu et al., 2004).

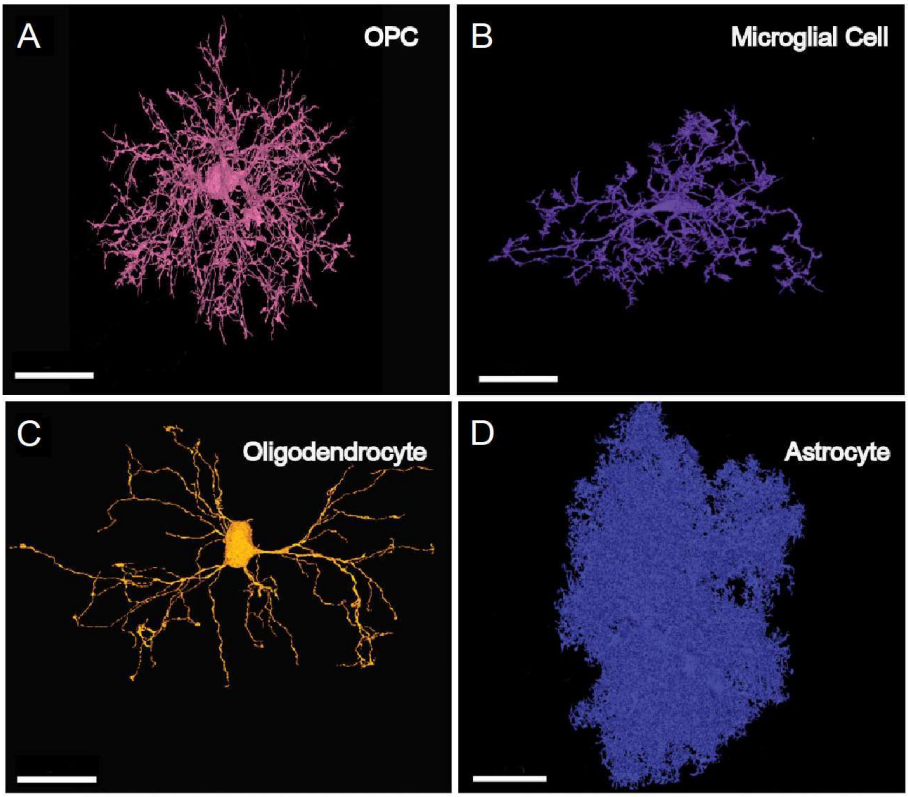

Figure 3. Distinct structural features of various glial cells in the developing visual cortex.
(A) 3D rendering of an OPC from a TEM reconstruction of 100-µm3 volume of layer 2/3 mouse visual cortex (P36) (B) 3D rendering of a microglial cell shows its thicker, less branched processes and elongated and flattened soma. (C) 3D rendering of a mature myelinating oligodendrocyte. Note, myelin sheaths are not shown, only the soma and cytoplasmic processes are displayed. (D) 3D rendering of an astrocyte. Scale bars = 20 µm. Adapted from: Buchanan et al., 2022.

On the other hand, OPCs in white matter areas of the central nervous system such as the corpus callosum and optic nerve, have a more polarized appearance. These cells extend their processes along the axonal axis (Gallo et al., 2008; Berry et al., 2002; Chittajallu et al., 2004; Kukleyet al., 2007). While some authors suggest that OPCs in white matter have a classic bipolar morphology similar to neural precursor cells, possessing only a few short processes emanating from opposing poles of the

cell body, others have shown that the process fields of white matter OPCs can ramify through the neuropil for distances up to 160-200 µm (Gallo et al., 2008). It is not clear why there are discrepancies in the reported morphologies of OPCs in white matter. It is possible that differences in age of experimental animals and/or variations in cell-labeling techniques could contribute to the observed discrepancies.

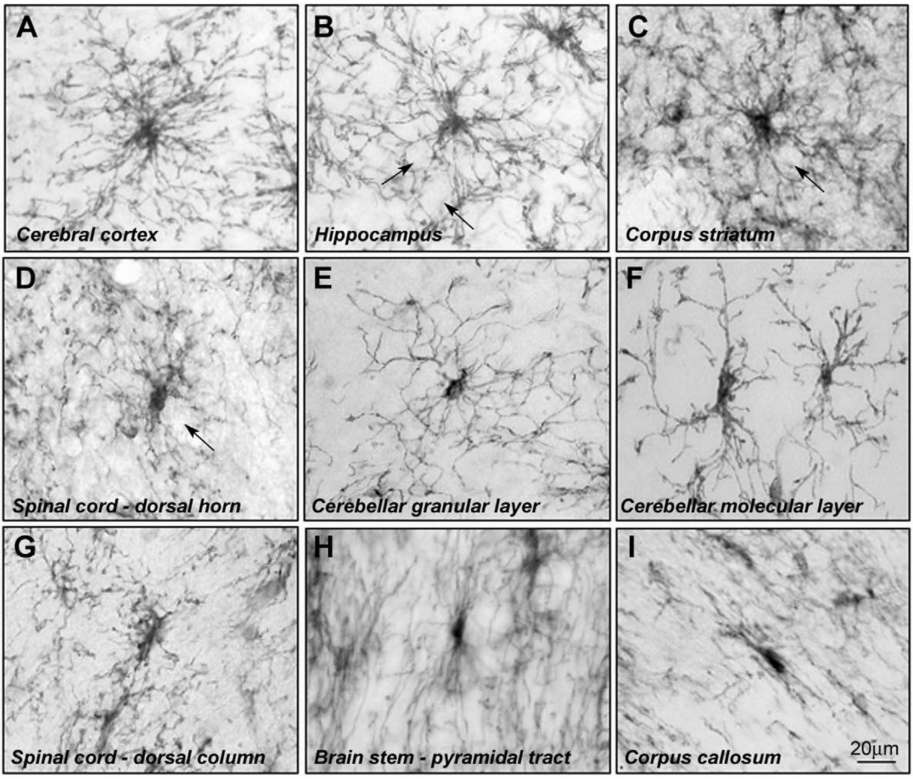

Figure 4. Morphology of OPCs in different regions of the adult rat CNS.

OPCs have a stellate morphology in gray matter regions, such as the cerebral cortex (A), hippocampus (B), striatum (C): long, fine processes extend and heavily branch all around the cell body (cell bodies are indicated by arrows). Dorsal horn of the spinal cord (D), cerebellar granular layer (E) and cerebellar molecular layer (F) have fewer processes. OPCs in white matter regions display elongated processes which align with axons: the dorsal spinal column (G), pyramidal tract (H), and corpus callosum (I). Scale bar = 20um. Adapted from Dawson et al., 2003.

NG2 glial cells exhibit a small polygonal soma measuring 10-15 µm and a multipolar tree of fine processes (Bergles et al., 2000; Chittajallu et al., 2004; Kukley et al., 2008; Kukley et al., 2010; Kukley et al., 2007; Gallo et al., 2008). The morphology of OPCs slightly differs depending on their location in the brain. In grey matter regions, OPCs have a centrally located soma that extends several long and slender primary processes that bifurcate two or more times, creating a symmetrical process field (Bergles et al., 2000; Chittajallu et al.). In white matter areas of the CNS, like the corpus callosum and optic nerve, OPCs usually appear more polarized, extending processes along the axonal axis (Berry et al., 2002; Butt et al., 2004; Chittajallu et al., 2004; Kukley et al., 2007). OPCs in white matter have a classic bipolar morphology of neural precursor cells, possessing only a few processes that are short in length and emanating from the opposing poles of the cell body (Chittajallu et al., 2004). However, other studies (Berry et al., 2002) demonstrate that the process fields of white matter OPCs can ramify through the neuropil for distances up to 160-200 µm. The reasons for these discrepancies remain unknown, but may include different age of experimental animals and/or variations in cell-labelling techniques.

OPCs, found in both grey and white matter, exhibit a fascinating morphological feature: small varicosities, or nodules, are distributed throughout the length of their processes (Berry et al., 2002; Butt et al., 2004; Jabs et al., 2005; Kukley et al., 2010). The functional significance of these structures remains unknown. It was speculated that they might represent the initiation of branching of NG2 cell processes (Chatterjee et al., 2008; Fröhlich et al., 2011). However, recently it was suggested that the nodules might be phagosomes (Buchanan et al., 2022). Alternatively, these nodules may serve as contact points between OPCs and other cell types in the brain. Interestingly, in primary oligodendrocyte cultures, NG2 and a PDZ (postsynaptic density-95/discs large/zona occludens-1) domain protein syntenin-1 co-localize at the nodules in NG2 cell processes (Chatterjee et al., 2008). PDZ domain-containing proteins are typically associated with plasma membrane proteins, and they are commonly restricted to specific sub-cellular domains, such as synapses or cell–cell contact points (Sheng and Sala, 2001; Chatterjee et al., 2008). In neurons, syntenin binds to kainate receptor subunits and all forms of AMPA receptor subunits, GluA1–4 (Hirbec et al., 2002; Hirbec et al., 2005). Notably, OPCs also express different subunits of AMPA receptors (Chen et al., 2018; Kula et al., 2019). Therefore, it is possible that by interacting with ionotropic glutamate receptors, syntenin plays a role in determining the formation and maturation of neuron-glia synapses.

Based on observations using immunohistochemical labeling in hippocampal slices and labeling individual astrocytes and OPCs with the fluorescent dye Lucifer Yellow during patch-clamp recordings, it appears that OPCs in grey matter have a distinct morphology compared to other glial cell types in the brain, such as astrocytes, microglia, and oligodendrocytes. Hippocampal astrocytes have large

soma and asymmetrically radiating processes that consist of several primary thick processes, from which emanate multiple smaller collateral branching secondary processes, giving them a bushy, spongiform appearance (Nishiyama et al., 2005). In contrast, OPCs have smaller soma and numerous irregular fine processes, but their smallest processes are not as thin as those of astrocytes, and thus OPCs clearly lack a sponge-like appearance (Nishiyama et al., 2005). Additionally, astrocyte processes often end in bulbous swellings, or terminal end-feet, which form the vascular and pial glia limitans. In contrast, NG2-glial processes taper to an end and do not appear to contribute to the glia limitants (Nishiyama et al., 2005). It is currently unclear whether these morphological differences hold true for OPCs and fibrous astrocytes in white matter. OPCs and astrocytes also differ in terms of molecular markers, as OPCs do not express glial fibrillary acidic protein (GFAP) or the glial glutamate–aspartate transporter, which are expressed by astrocytes, while astrocytes do not express NG2, PDGF-Rα, and O4 (Levison et al., 1999; Zhou et al., 2006; Fröhlich et al., 2011; Kukley et al., 2010).

Differences have been observed in the number, length, appearance, and size of cell soma between OPCs and more mature cells of the oligodendrocyte lineage. Mature oligodendrocytes bear myelin sheaths, whereas OPCs do not (Trapp et al., 1997; De Biase et al., 2010; Kukley et al., 2010). OPCs lack the molecular markers associated with more mature cells of the oligodendroglial lineage, such as proteolipid protein (PLP), myelin basic protein, 2,3-cyclic nucleotide 3-phosphodiesterase, galactocerebroside O1, and tetraspanin CD9 (Polito et al., 2005; Nishiyama et al., 2009; Kukley et al., 2010). However, some premyelinating oligodendrocytes may still carry residual amounts of NG2 proteoglycan, indicating that they are the descendants of OPCs.

OPCs likely share some morphological similarities with ramified microglial cells, but no direct comparison of their morphological properties has been performed under identical experimental conditions. Insights into the morphological structure of ramified microglia come from reconstructions of Lucifer Yellow-filled cells in brain slices of adult mice (Boucsein et al., 2003) and in vivo 2-photon imaging of microglial cells in adult EGFP-CX3CR1 transgenic mice (Davalos et al., 2005; Nimmerjahn et al., 2005). Similar to OPCs, microglial cells have small cell soma from which numerous thin and highly ramified processes extend symmetrically (Boucsein et al., 2003; Davalos et al., 2005; Nimmerjahn et al., 2005). In contrast to OPCs, microglia cell processes lack small nodules but display highly motile filopodia-like protrusions of variable shape, typically forming bulbous endings under normal conditions and/or during injury (Davalos et al., 2005; Nimmerjahn et al., 2005). Double-labelling immunohistochemical studies have established that OPCs are clearly distinct from resting or activated microglia: OPCs are negatively stained with the markers of microglial cells, such as 4H1,

CD68, F4/80, or OX42 (Nishiyama et al., 1997; Nishiyama et al., 2002; Horner et al., 2002; Kukley et al., 2010).

1.3 Passive membrane properties of OPCs

NG2+ cells in acute brain slices obtained from juvenile animals typically have a capacitance of 15-30 pF, membrane resistance of 100-500 MΩ, and a steady resting membrane potential (RMP, V_r) between −80 and −100 mV (Clarke et al., 2012; De Biase et al., 2010; Haberlandt et al., 2011; Kukley et al., 2008; Lin and Bergles, 2002; Maldonado et al., 2013). These findings suggest that K^+ channels contribute significantly to the resting membrane conductance as the V_r is near the calculated equilibrium potential for K^+ (EK). The main K^+ channels open at rest are Kir4.1 and two-pore (K2P) K^+ channels, which are inward-rectifying (Clarke et al., 2012).

Kir4.1, an inward-rectifying channel, is expressed in NG2+ cells, oligodendrocytes, and astrocytes and has been implicated in setting the V_r (Butt and Kalsi, 2006; Chever et al., 2010; Djukic et al., 2007; Kofuji et al., 2000; Neusch et al., 2006, 2001). The RNA-Seq transcriptome database shows that NG2+ cells express high levels of Kir4.1 (Kcnj10) mRNA, more than any other K^+ channel subunit. However, the expression level of Kir4.1 in NG2+ cells is only about half that observed in astrocytes (Zhang et al., 2014). This finding is consistent with data from Kir4.1-EGFP BAC-transgenic mice, which showed that EGFP intensity, reflecting promoter activity, was about three times higher in GFAP+ astrocytes than in NG2+ cells (Tang et al., 2009).

Kir4.1 subunits can combine with Kir5.1 (Kcnj16) subunits to form heteromeric channels, resulting in channels with increased single-channel conductance and greater pH sensitivity (Butt and Kalsi, 2006; Hibino et al., 2004). mRNA for Kir5.1 is found at approximately two-fold higher levels in NG2+ cells than in astrocytes, suggesting that heteromeric channels may have a relatively greater role in NG2+ cells (Zhang et al., 2014).

When the membrane potential of NG2+ cells is hyperpolarized from the V_r, inward currents are observed in whole cell recordings mediated by Kir4.1 (Djukic et al., 2007). These inward currents are specifically blocked by low concentrations of extracellular Ba^{2+}, which is an inhibitor of Kir channels. In addition, “complex glia” of Kir4.1 glia-specific conditional knockout (cKO) animals showed that these inward currents are abolished. Furthermore, “complex glia” in Kir4.1 cKO animals appear to be greatly reduced in number in the hippocampus and are significantly depolarized to ~ −40 mV with increased membrane resistance (~500 MΩ). These observations suggest that Kir4.1 plays an important role in the development, survival, or differentiation of NG2+ cells, as well as in the severe disruption of myelin in Kir4.1 knockout animals (Djukic et al., 2007; Neusch et al., 2001).

There is a possibility that NG2+ cells express additional K^+ 'leak' channels that are not sensitive to Cs^+. Two-pore domain (K2P) K^+ channels fit this pharmacological profile (Feliciangeli et al., 2014), and some studies have characterized the expression of K2P channels by passive astrocytes (Seifert et al.,

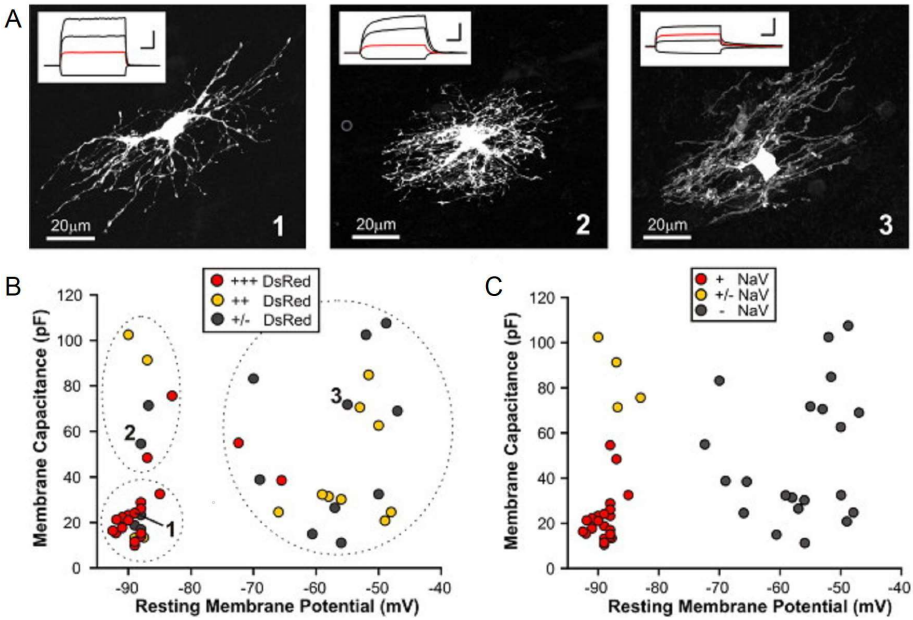

Figure 5. V_r, C_m and Na_v current in OL lineage cells at different stages of development.
(A) The morphologies of representative cells from the OL lineage and their responses to depolarizing current injection. (B) Plots of membrane capacitance versus resting membrane potential for cells with different levels of NG2 promoter-driven DsRed fluorescence. Outlines represent 3 clusters of cells (OPC, pre-OL, OL) classified based on the brightness of their NG2-DsRed and membrane properties. (C) The same as (B) but colored according to the amplitude of the NaV currents. Adapted from DeBiase et al., 2010.

2009; Zhou et al., 2009). Several K2P isoforms, including TWIK1 (Kcnk1), TREK1 (Kcnk2), and Kcnk10, are highly expressed in NG2+ cells according to the RNA-Seq transcriptome database (Zhang et al., 2014), but a recent study showed no changes in NG2+ cell current properties in a TWIK1 knockout mouse, nor was there any effect observed when isoflurane, an activator of TREK1, was applied (Maldonado et al., 2013). One possible explanation for this discrepancy between mRNA expression data and physiological data is that channels may not be heavily trafficked to the cell membrane, despite high levels of transcription and/or translation. This has been observed for TWIK1

in passive astrocytes, where the channel is mainly sequestered in the intracellular compartment (Feliciangeli et al., 2010; Wang et al., 2013).

In addition to their K^+ 'leak' channels, NG2+ cells express the Na^+ leak channel Nalcn at a level comparable to neurons and higher than mature oligodendrocytes, as shown in the RNA-Seq transcriptome database (Zhang et al., 2014). This slight baseline Na^+ permeability, along with other neuronal properties, is displayed by NG2+ cells, but the K^+ leak conductance dominates due to their hyperpolarized resting membrane potential (V_r, RMP) (Zhang et al., 2014).

NG2+ cell membrane properties change during postnatal development, transitioning from outward rectification to an increasingly linear phenotype due to an increase in Kir4.1 expression (De Biase et al., 2010; Maldonado et al., 2013). This findings are in agreement with earlier studies of the changing electrophysiological properties of complex glia in the hippocampus over time (Kressin et al., 1995; Zhou et al., 2006), as well as studies showing the broad upregulation of Kir4.1 in the CNS during postnatal development (Gupta and Kanungo, 2013; Kalsi et al., 2004; Nwaobi et al., 2014; Seifert et al., 2009). It is essential to consider the variability in channel expression when interpreting the RNA-Seq transcriptome database, which only captures NG2+ cells at one time in development (P17) (Zhang et al., 2014).

NG2+ cells exhibit regional variability in their passive membrane properties, as demonstrated by a comparison of cortical and callosal NG2+ cells. White matter NG2+ cells have smaller capacitances, higher membrane resistances, and a less negative V_r than cells in gray matter, along with much smaller Cs^+-sensitive Kir currents (Chittajallu et al., 2004; De Biase et al., 2010). However, with age NG2+ cells dramatically increase their membrane conductance making these differences less distinct (De Biase et al., 2010).

1.4 Voltage-gated K+ channels

NG2+ cells exhibit a non-linear current profile characteristic of A-type (KA) and delayed-rectifier (KDR) K^+ channels upon depolarization (Barres et al., 1990; Berger et al., 1991; Borges et al., 1995; Kettenmann et al., 1991; Sontheimer et al., 1989; Williamson et al., 1997). The rapid activation and inactivation kinetics of A-type channels contribute to the initial peak depolarization, while delayed-rectifiers activate more slowly and do not inactivate, producing the sustained steady-state current. The relative proportion of these two current components varies by region, with white matter NG2+ cells displaying higher IKDR current densities compared to cortical NG2+ cells, resulting in a higher IKDR/IKA ratio (Chittajallu et al., 2004).

Despite extensive research, the precise molecular identity of the channels underlying these currents remains unclear. The majority of studies have focused on the Shaker family of K^+ channels,

Kv1.1-1.6, with expression of Kv1.2, Kv1.4, Kv1.5, and Kv1.6 mRNA and protein detected in cultured NG2+ cells, and Kv1.5 being the most highly expressed (Attali et al., 1997). A separate study using single-cell RT-PCR found that individual cultured progenitors express varying combinations of all six Shaker-type channels, with Kv1.2, Kv1.5, and Kv1.6 being the most commonly expressed. However, only Kv1.4, Kv1.5, and Kv1.6 were detected at the protein level using immunocytochemistry (Schmidt et al., 1999). Lastly, another study utilizing immunocytochemistry found expression of Kv1.3 through Kv1.6 protein in cultured progenitors (Chittajallu et al., 2002).

Multiple studies consistently demonstrate that specific inhibition or knockdown of individual channel subunits (excluding Kv1.5 knockdown [Attali et al., 1997] and a partial effect of a toxin specific to Kv1.3 [Chittajallu et al., 2002]) has only minor effects on the current properties of cultured NG2+ cells. These findings, coupled with the heterogeneity of expression observed at the mRNA and protein levels, suggest that NG2+ cells express various heteromeric K^+ channels that can compensate for missing subunits to maintain the overall current profile (Attali et al., 1997; Chittajallu et al., 2002; Schmidt et al., 1999). Another significant trend is that mRNA and protein levels of Kv channel subunits seem to be regulated independently, which leads to variations between mRNA and protein expression, even within the same study. As a result, using mRNA levels to draw conclusions about the abundance of membrane K^+ channels necessitates exercising caution (Attali et al., 1997; Chittajallu et al., 2002; Schmidt et al., 1999).

Despite this caution, the RNA-Seq transcriptome database is the most thorough analysis of K^+ channel expression in NG2+ cells to date. In agreement with previous studies, the mRNA for the delayed rectifier Kv1.6 is highly expressed, whereas the mRNA for other previously identified Shaker type delayed rectifiers is expressed at lower levels. Kv1.2 and Kv1.3 are expressed at low but significant levels, while Kv1.5 is expressed at very low levels (0.8 FPKM). Furthermore, mRNA for several non-Shaker type delayed rectifier channels, Kv7.2 and Kv2.1, are expressed at high levels. Kv7.2 has previously been identified by RT-PCR and immunohistochemistry in at least a subset of cortical NG2+ cells. Kv2.1, abundant in numerous types of neurons, has not been discovered in NG2+ cells thus far (Du et al., 1998; Trimmer, 1991).

In the RNA-Seq transcriptome database, Kv1.4, the sole A-type Shaker channel, is expressed at low levels in NG2+ cells (0.7 FPKM). Kv4.2, Kv4.3, and Kv3.3 are highly expressed A-type channel subunits in neurons and high expression levels are maintained in OPCs. Kvβ2, Kvβ3, and Kvβ1 are the most highly expressed Kv beta subunits in NG2+ cells. KCa1.1, the large conductance Ca^{2+}-activated [BK] channel, along with its β4 subunit, is highly expressed in NG2+ cells, confirming previous findings (Buttigieg et al., 2011) and KCa2.1 and KCa2.2, the SK channel subunits, are also expressed at low but significant levels.

Voltage-gated K^+ channel expression is important for regulating NG2+ cell behavior, with Kv1.3 being upregulated during the G1 phase of the cell cycle. Blocking this channel with specific toxins prevents the cells from entering the G1/S transition, while overexpression of Kv1.3 or Kv1.4 promotes proliferation of cultured NG2+ cells without mitogens, and overexpression of Kv1.6 inhibits proliferation with mitogens. However, knockdown and overexpression of Kv1.5 have not produced any effects on NG2+ cell proliferation. Differentiation of cultured NG2+ cells into oligodendrocytes is not significantly affected by overexpression of Kv channel subunits, suggesting that proliferation and differentiation of these cells can be regulated independently.

1.5 Voltage-gated Na^+ channels

NG2+ cells, like neurons, express tetrodotoxin (TTX)-sensitive voltage-gated Na^+ (Nav) channels (Barres et al., 1990; Berger et al., 1992a; Bergles et al., 2000; Borges et al., 1995; Maldonado et al., 2011; Sontheimer et al., 1989; Williamson et al., 1997), but their expression density varies by region in the brain (Chittajallu et al., 2004) and decreases as NG2+ cells differentiate into oligodendrocytes (De Biase et al., 2010; Sontheimer et al., 1989). Together with Kv channels, the expression of Nav channels provides NG2+ cells with the necessary equipment to (potentially) generate action potentials. Early postnatal animals display NG2+ cells that generate Na^+ spikes when depolarizing current is injected, but these spikes have a high threshold for initiation, have less typical shape and slower kinetics compared to neuronal action potentials (Chittajallu et al., 2004; De Biase et al., 2010; Káradóttir et al., 2008; Tong et al., 2009). NG2+ cells have a limited ability to sustain repetitive spiking in response to tonic depolarizing current injection, with most cells exhibiting a single spike (Chittajallu et al., 2004; De Biase et al., 2010), although some studies have reported otherwise (Káradóttir et al., 2008). Nonetheless, the physiological significance of this phenomenon is unclear, since synaptic inputs produce minimal depolarization of NG2+ cells and spontaneous spiking has not been observed (De Biase et al., 2010). As the Kv/Nav ratio increases in adult animals due to an increase in K^+ channel density, NG2+ cells lose the ability to generate spikes (De Biase et al., 2010; Maldonado et al., 2011). The specific subunits of Nav channels responsible for the excitability of NG2+ cells have not been extensively studied. One research study investigated the TTX-sensitivity of Na^+ currents in hippocampal NG2+ cells and concluded that the IC50 of TTX (39.3 nM) was compatible with the expression of multiple subunit types, rather than any individual subunit (Xie et al., 2007). The expression of mRNA for Nav1.3, Nav1.2, Nav1.8, and Nav1.1, as well as beta subunits Navβ1, Navβ3, and Navβ2, was observed in the RNA-Seq database. Therefore, it is probable that a combination of Nav channel subunits with distinct properties contributes to the voltage-dependent Na^+ currents in NG2+ cells.

1.6 Voltage-gated Ca^{2+} channels

Numerous studies have demonstrated that Ca^{2+} signaling plays a critical role in regulating behavior of NG2+ cells and oligodendrocytes, including proliferation, migration, process extension, differentiation, and myelination (Cheli et al., 2015; Paez et al., 2009; Simpson and Armstrong, 1999; Soliven, 2001; Yoo et al., 1999). A number of mechanisms can cause Ca^{2+} elevation in NG2+ cells, such as direct influx through plasma membrane voltage- or ligand-gated channels and release from internal Ca^{2+} stores. The existence of voltage-gated Ca^{2+} channels in NG2+ cells is especially intriguing, as it could establish a direct link between depolarization from synaptic activity and Ca^{2+}-triggered alterations in cell behavior.

Inward currents mediated by voltage-dependent, divalent cation-selective channels, which suggest the presence of Ca^{2+} channels, were observed in "complex astrocytes" using electrophysiological recordings in a high-Ba^{2+}, low-Na^{+} bath solution (Akopian et al., 1996; Berger et al., 1992a). Subsequent studies verified that these currents existed in NG2+ cells and were sensitive to L-type and T-type Ca^{2+} channel inhibitors (Fulton et al., 2010; Haberlandt et al., 2011). Despite this, the overall current density was small.

The molecular identity of the subunits that form voltage-gated Ca^{2+} channels in NG2+ cells was analyzed in situ using single-cell RT-PCR (Haberlandt et al., 2011). mRNA for L-type (Cav1.2 and Cav1.3), T-type (Cav3.1 and Cav3.2), P/Q-type (Cav2.1), and N-type (Cav2.2) α1 subunits were found, consistent with pharmacological findings. The RNA-Seq transcriptome database supports these findings, revealing a nearly identical list of highly expressed α1 subunits as well as various β, γ, and α2δ subunits. The only discrepancy between the two datasets is Cav2.3, an R-type subunit that was not detected by single-cell RT-PCR (Haberlandt et al., 2011) but was discovered by RNA-Seq. Cav1.2 appears to be the main pore-forming subunit, as knockdown of Cav1.2 in NG2+ cells using siRNA results in a reduction of around 75% of Ca^{2+} elevation following depolarization (Cheli et al., 2015).

1.7 Voltage-gated Cl^- channels

NG2+ cells have been found to express voltage-gated Cl^- channels, in addition to cation channels. The RNA-Seq transcriptome database shows that Clc2 (Clcn2) is the only gene for plasma membrane voltage-gated Cl^- channels that is expressed in NG2+ cells. The Clc2 channel has a small unitary conductance and inward-rectifying properties, and can be activated by various factors such as hyperpolarization, cell swelling, increased intracellular Cl^- concentration, or mild extracellular acidification. Whole cell patch-clamp recordings from “complex” astrocytes in hippocampal and cortical brain slices have demonstrated a hyperpolarization-activated anion current that is absent in Clc2−/−

Gene Name	Known as	Expression level	Category	*Gene Name*	Known as	Expression level	Category
Kcnj10	Kir4.1	82.6	Inward rectifier	*Nalcn*	NaCln	19.3	Sodium leak channel
Kcnmb4	KCaβ4	45.5	BK (β subunit)	*Scn1b*	Navβ1	14.5	Voltage-gated (β subunit)
Kcnd2	Kv4.2	27	A-type	*Scn3b*	Navβ3	12.9	Voltage-gated (β subunit)
Kcna6	Kv1.6	24.1	Delayed rectifier	*Scn3a*	Nav1.3	11.4	Voltage-gated (TTX sensitive)
Kcnk1	K2P1.1/ TWIK1	24	Inward rectifier (two pore)	*Scn2a1*	Nav1.2	7.6	Voltage-gated (TTX sensitive)
Kcnd3	Kv4.3	22.3	A-type	*Scn8a*	Nav1.8	5	Voltage-gated (TTX resistant)
Kcnk2	K2P2.1/ TREK1	19.6	Inward rectifier (two pore)	*Scn1a*	Nav1.1	4.9	Voltage-gated (TTX sensitive)
Kcnq2	Kv7.2	10.9	Delayed rectifier	*Scn2b*	Navβ2	4.8	Voltage-gated (β subunit)
Kcnc3	Kv3.3	8.9	A-type	*Cacng4*	TARPγ4	275.8	γ subunit*
Kcnab2	Kvβ2	8.8	Kv (β subunit)	*Cacng7*	TARPγ7	103	γ subunit*
Kcnk10	K2P10.1	7.9	Inward rectifier (two pore)	*Cacnb3*	Cavβ3	25.7	β subunit
Kcnj16	Kir5.1	7	Inward rectifier	*Cacng8*	TARPγ8	12	γ subunit*
Kcnb1	Kv2.1	6.8	Delayed rectifier	*Cacng5*	TARPγ5	11.7	γ subunit*
Kcnma1	KCa1.1	6.3	Large conductance calcium-activated (BK)	*Cacnb4*	Cavβ4	8.4	β subunit
Kcnh2	Kv11.1/ HERG	5.5	Inward rectifier	*Cacna2d3*	Cavα2δ3	8	α2δ subunit
Kcnn1	KCa2.1	4.9	Small conductance calcium-activated (SK)	*Cacna1d*	Cav1.3	7.8	α1 subunit, L-type
Kcna2	Kv1.2	4.8	Delayed rectifier	*Cacna1g*	Cav3.1	7.7	α1 subunit, T-type
Kcnab3	Kvβ3	4.6	Kv (β subunit)	*Cacnb1*	Cavβ1	7.2	β subunit
Kcne4	MiRP3	4.5	Kv (β subunit)	*Cacna2d1*	Cavα2δ1	7	α2δ subunit
Kcnab1	Kvβ1	4.5	Kv (β subunit)	*Cacna1c*	Cav1.2	6.5	α1 subunit, L-type
Kcnc1	Kv3.1	4.1	Delayed rectifier	*Cacna1a*	Cav2.1	6.5	α1 subunit, P/Q-type
Kcnh8	Kv12.1	4.1	Slow activating/inactivating voltage-gated channel	*Cacna1e*	Cav2.3	6	α1 subunit, R-type
Kcnn2	KCa2.2	3.7	Small conductance calcium-activated (SK)	*Cacna1h*	Cav3.2	4.1	α1 subunit, T-type
Kcna3	Kv1.3	3.6	Delayed rectifier	*Cacna2d2*	Cavα2δ2	2.8	α2δ subunit
Kcnh3	Kv12.2	3.6	Voltage gated	*Cacna1b*	Cav2.2	2.2	α1 subunit, N-type
Kcnj3	Kir3.1	3.4	Inward rectifier	*Clcn2*	Clc2	9.2	Hyperpolarization-activated Inward rectifying
Kcna1	Kv1.1	3.4	Delayed rectifier	*Hcn2*	HAC1, BCNG2	14.8	Mixed Na+/K+ current
Kcnh5	Kv10.2	3.1	Outward rectifier, non-inactivating	*Hcn3*	HAC3, BCNG4	3.7	Mixed Na+/K+ current
Kcnd1	Kv4.1	2.9	A-type	*Kcnc4*	Kv3.4	2.4	A-type
Kcnq3	Kv7.3	2.8	Delayed rectifier	*Kcnf1*	Kv5.1	2.3	Modifier of Kv2 channels

Table 1. Summary of the K^+, Na^+, Ca^{2+} and Cl^- channels found in OPCs and their expression levels in RNA-Seq transcriptome database. Adapted from: Larson et al., 2016.

mice, which supports the expression of this channel by NG2+ cells. While Clc2 expression has been confirmed in GFAP+ astrocytes and CC1+ oligodendrocytes by immunohistochemistry and in situ hybridization, it is unknown whether NG2+ cells specifically express this channel. Nevertheless, Clc2−/− mice exhibit severe and progressive myelin vacuolation, indicating a crucial role in oligodendrocyte function (Blanz et al., 2007).

1.8 Hyperpolarization-activated cyclic nucleotide-gated (HCN) channels

HCN channels are part of the voltage-gated K^+ channel superfamily and are permeable to both Na^+ and K^+. These channels are activated by hyperpolarization, leading to "anomalous rectification," and many are open at the resting membrane potential in both neurons and glia. There are four HCN subunit isoforms, HCN1-4, and both homomeric and heteromeric channels can be formed in vivo. NG2+ cells display evidence of anomalous rectification that is consistent with HCN channel expression. Two HCN channel subunits are significantly expressed in NG2+ cells: HCN2 mRNA was present at higher levels than HCN3.

Early studies found HCN2 expression in a scattered population of cells in white matter tracts, suggesting its expression in glial cells in addition to neurons. Another study found that HCN2 antibody staining colocalized extensively with GST-π, a marker of mature oligodendrocytes, although not with NG2. However, the transcriptome database shows that HCN2 mRNA expression in myelinating oligodendrocytes is four to five times higher than in NG2+ cells, and it is possible that the lower level of expression in NG2+ cells may not be sufficient for antibody detection. Age differences between the studies could contribute to the discrepancy, as HCN2 protein levels increase with age during postnatal development in the hippocampus.

1.9 TRP channels

The transient receptor potential (TRP) family of cation channels is known for its wide range of activation mechanisms, including ligand binding, G-protein coupled receptor (GPCR) activation, and physical stimuli such as temperature or pressure, resulting in diversity within the family (Vennekens et al., 2012). The family is composed of three subfamilies: the classic/canonical TRPs (TRPCs), the vanilloid receptor-related TRPs (TRPVs), and the melastatin-related TRPs (TRPMs). In glial cells, several TRP channels have been identified, including TRPC1 and TRPC3 in NG2+ cells and oligodendrocytes, respectively, and TRPM3 in both cell types, all of which are nonselective cation channels activated through various signaling cascades (Fusco et al., 2004; Paez et al., 2011; Weerth et al., 2007; Hoffmann et al., 2010).

TRPM7, a nonspecific cation-permeable channel that also contains a serine-threonine kinase domain, is the most highly-expressed TRP channel subunit in NG2+ cells based on the RNA-Seq transcriptome database. This channel has been widely studied in other cell types and is involved in trace metal ion homeostasis, as well as proliferation, migration, differentiation, and cell death (Fleig and Chubanov, 2014). However, its specific role in NG2+ cells remains unknown. TRPC1, TRPM3, and TRPC2 are also expressed in NG2+ cells at lower levels in the transcriptome database, although TRPC2 is a pseudogene in humans (Clapham et al., 2005).

1.10 Synaptic signaling and OPCs

All functions of the central nervous system rely on communication between neurons. The primary mode of neuronal communication is synaptic transmission, with the majority of synapses being chemical synapses. These synapses provide high-speed and precise targeting only to connected cells, facilitated by complex structural and functional organization of pre- and postsynaptic elements. Volume transmission, on the other hand, is a different type of intercellular communication that occurs outside of synapses and involves the slow movement of released transmitters to target cells. This form of communication can involve both neurons and glial cells, in contrast to synaptic transmission which mainly involves neurons.

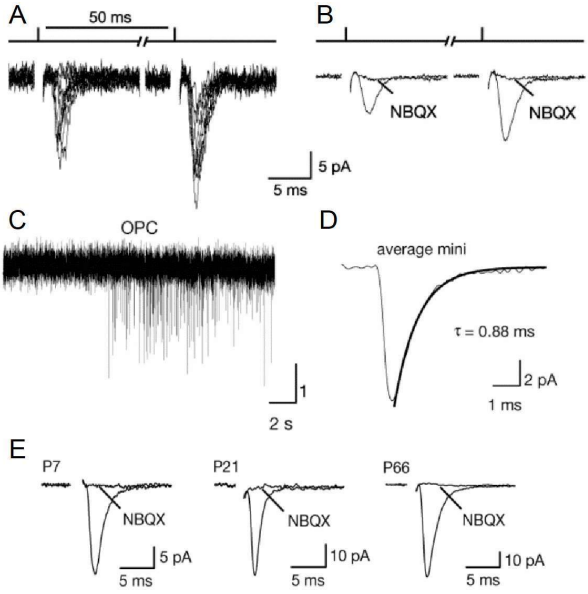

Figure 6. EPSCs in OPCs are mediated by AMPARs.
(A) Stimulation of Schaffer collaterals evokes inward currents in OPCs. (B) These currents are blocked by NBQX. (C) mEPSCs elicited in OPCs by application of pardaxin. (D) Averaged mEPSC obtained from OPCs in (C). Note the fast rise time of 295 ± 15 µs and exponential decay with tau constant of 983 ± 58 µs. (E) Stimulation of Schaffer collaterals evokes inward, NBQX-blocked currents in OPCs of P7 – P66 ages. Adapted from: Bergles et al., 2000.

Recent research has shown that synaptic junctions also exist between neurons and oligodendrocyte precursor cells (OPCs), which are one type of glial cells. It is unclear whether these junctions are true synapses with all properties of neuronal synapses or whether they are synaptic-like structures. Additionally, it is uncertain whether neuron-OPC signaling is identical to neuronal synaptic transmission or if it has different features, or if it is a form of volume transmission. It is also unclear whether OPCs differentiate into oligodendrocytes (OLs) are involved in synaptic transmission or volume transmission. Understanding whether the signaling between neurons and OPCs, or OLs, is synaptic or non-synaptic is important for further understanding the complex communication within the central nervous system. (Bergles et al., 2000; Kukley et al., 2007; Ziskin et al., 2007).

1.11 Structure and function of glutamatergic neuronal synapses

Glutamate is the most abundant excitatory neurotransmitter in the CNS, and glutamatergic chemical synapses are composed of two primary components: the presynaptic membrane with one or more active zones, and the postsynaptic membrane containing glutamate receptor complex, directly opposing the presynaptic membrane across a synaptic cleft, a 20-40 nm gap. When an action potential reaches the presynaptic bouton, the presynaptic membrane depolarizes, which in turn, opens voltage-gated Ca^{2+}-channels (VGCCs), allowing Ca^{2+} to enter, triggering the release of glutamate-filled vesicles into the synaptic cleft. Once released, glutamate binds to receptors on the postsynaptic cell, leading to ion flow, change in membrane depolarization, and/or second-messenger signaling cascade. The structural organization of glutamatergic synapses is complex, involving numerous proteins that work together in the presynaptic site for vesicle fusion and recycling and in the postsynaptic density (PSD) for synaptic input detection and transduction (Husi et al., 2000; Rosenmund et al., 2003).

1.12 Exocytosis and endocytosis of synaptic vesicles in presynaptic boutons

Exocytosis of synaptic vesicles is a highly regulated process (Sudhof, 2004). For exocytosis to occur, a synaptic vesicle must first be targeted and docked to the active zone at the presynaptic membrane. ATP-dependent processes prime the vesicle, which then becomes sensitive to Ca^{2+}. Once Ca^{2+} ions enter through the voltage-gated calcium channels located at the active zone, they trigger the fusion of readily releasable vesicles with the plasma membrane, leading to the release of the vesicle's content into the synaptic cleft.

SNARE (soluble NSF-attachment protein receptor) proteins are responsible for the formation, opening, and expansion of the fusion pore. The major SNARE proteins include the vesicular protein synaptobrevin/VAMP and two proteins anchored to the plasma membrane: syntaxin and SNAP-25. The SM (Sec1/Munc18-like) proteins interact with the SNARE proteins, resulting in the release of the

necessary energy for vesicular fusion (Rizo and Sudhof, 2012). Interestingly, SNARE proteins are insensitive to Ca^{2+} ions that are required for triggering exocytosis. Instead, the synaptotagmin family of proteins serves as the primary Ca^{2+} sensors at synapses and interacts with SNAREs (Fernandez-Chacon et al., 2001). Synaptotagmins, localized to synaptic vesicles, have a low affinity for Ca^{2+} (Sudhof, 2002). As such, a substantial increase in presynaptic Ca^{2+} is necessary for exocytosis.

The average intracellular concentration of free Ca^{2+} in mammalian cells is close to ~100 nM, while enzymatic reactions require ~1 μM Ca^{2+}. However, when an action potential invades the presynaptic bouton and triggers the opening of VGCCs, the Ca^{2+} concentration within a microdomain at the active zone can reach 200–300 μM (Llinas et al., 1992). Despite this, Ca^{2+} transients are short-lived, with a half-width of ~500 μs, due to the rapid diffusion of Ca^{2+} away from the entry site and/or its capture by fast buffers, which terminates the rise in Ca^{2+} concentration (Meinrenken et al., 2002). The short duration of Ca^{2+} transient ensures that the major component of glutamate release, referred to as "phasic release," is brief and can start 50 μs after Ca^{2+} entry initiation.

Efficient refilling of synaptic vesicles in presynaptic terminals is necessary for synapses to reliably release neurotransmitters, not only upon single action potentials, but also during repetitive neuronal firing. One well-understood pathway for synaptic vesicle recycling is clathrin-mediated endocytosis, which involves the lateral movement of the fused vesicle away from the active zone, acquisition of a clathrin coat, invagination to form a bud, fission, and loss of the clathrin coat (Sudhof, 2004). The coat of the bending vesicular membrane is generated by several adaptors and scaffold proteins, in addition to clathrin (Kaksonen and Roux, 2018). Actin filaments, various regulatory components, and scission-related proteins are involved in the scission of the endocytosed vesicle. The endocytosis machinery is disassembled by proteins responsible for removing the clathrin coat (Kaksonen and Roux, 2018). Although clathrin-mediated endocytosis is a relatively slow process, a number of faster mechanisms, including compensatory endocytosis, activity-dependent bulk endocytosis, ultrafast endocytosis, and kiss-and-run have also been proposed (Gan and Watanabe, 2018). After recapturing of vesicular membrane, acidification occurs when protons are pumped into the vesicles by vacuolar-type H^+-ATPases (V-ATPases). This proton gradient is crucial, as it is subsequently used by vesicular glutamate transporters (VGLUT1-3) to fill synaptic vesicles with glutamate. Any alterations in acidification lead to “empty” synaptic vesicles and loss of glutamate release (Wang and Hiesinger, 2013).

1.13 Postsynaptic glutamate receptors

Glutamate is released from the presynaptic bouton and quickly travels through the synaptic cleft to bind to glutamate receptors on the postsynaptic membrane. Two types of glutamate receptors exist at

synapses, ionotropic (iGluRs) and metabotropic (mGluRs), which have different functions. iGluRs are ligand-gated ion channels that facilitate fast synaptic signaling. AMPARs and KARs are quicker than NMDARs upon glutamate binding, producing transmembrane flux of K^+, Na^+, and Ca^{2+} ions and depolarization of the postsynaptic neuron. An action potential may be generated if the depolarization is strong enough. On the other hand, mGluRs are G-protein-coupled receptors with seven transmembrane helices. The mGluRs include Group I (mGluR1 and mGluR5), Group II (mGluR2 and mGluR3), and Group III (mGluR4, mGluR6, mGluR7, mGluR8) receptors, which trigger intracellular signaling cascades and can induce Ca^{2+} release from internal stores. mGluRs can also open G-protein-coupled inwardly-rectifying K^+ channels and thus modulate the cell membrane potential. Unlike iGluRs, mGluRs generate longer effects that can last from hundreds of milliseconds to several seconds or more. Moreover, mGluRs are important in synaptic transmission modulation and plasticity. (Niswender and Conn, 2010; Reiner and Levitz, 2018; Sherman, 2014).

The organization of synapses in the postsynaptic region is highly complex (Sheng and Kim, 2011). Extensive proteomic analysis has shown that the PSD contains hundreds of proteins, including glutamate receptors, kinases (such as calcium/calmodulin-dependent protein kinase II [CaMKII]), phosphatases (e.g., phosphatase 1, 2A, 5, calcineurin), adaptor and scaffolding proteins (such as PSD-95 and SAP-102), regulatory proteins (such as transmembrane AMPAR-regulatory proteins [TARPs]), adhesion molecules, cytoskeletal proteins (e.g., actin, tubulin, myosin), and various other proteins (Baucum 2nd, 2017; Collins et al., 2006; Lisman et al., 2002). The glutamate receptors interact with signal transduction proteins to form large multi-protein complexes that are crucial for cellular signaling (Husi et al., 2000). Molecular interactions within these complexes drive both structural and functional changes at synapses during synaptic transmission and plasticity. They regulate the number and/or activity of dendritic NMDARs and AMPARs, and AMPAR trafficking (Husi et al., 2000; Lei et al., 2001; Lisman et al., 2002; Sattler et el., 2000; Zhou et al., 2001).

1.14 Interaction between pre- and postsynaptic elements at neuronal synapses

Direct interactions between molecules located at the pre- and postsynaptic sites and the geometry of the synaptic cleft are crucial for synaptic signaling. Among the key proteins involved in this interaction are cell adhesion molecules of the neurexins family that bind to various postsynaptic partners, including neuroligins, LRRTM proteins, and SynCAM (Biederer et al, 2017). Additionally, trans-synaptic bridges are formed between presynaptic ephrins and postsynaptic ephrin receptors (e.g., EphB2), and between presynaptic RIM1 and postsynaptic PSD-95 proteins (Biederer et al., 2017). Recent super-resolution imaging experiments suggest that RIMs and PSD-95 form opposing nanoclusters, while AMPARs form “nanocolumns” that span the synaptic cleft (Tang et al., 2016).

These trans-synaptic interactions have various functions, including regulating the spatial arrangement between pre- and postsynaptic elements, promoting presynaptic maturation, and influencing stability of the active zone (Biederer et al., 2017; Yamagata et al., 2018). However, the functional significance of nano alignment between synaptic elements is still unknown.

1.15 Glutamatergic signaling mediated by volume transmission

The spatiotemporal features of volume transmission, which encompasses various types of non-synaptic signaling, are influenced by several factors such as the source of released glutamate, receptor types, and spatial relationship between the release site and receptors (Agnati et al., 2010; Rusakov and Kullmann, 1998; Trueta and De-Miguel, 2012). Volume transmission involves neurons and/or glial cells and can occur through three primary mechanisms: (a) fast vesicular exocytosis at synapses, followed by spill-over to activate extrasynaptic receptors; (b) ectopic vesicular release close to synapses, along axons far from synapses, from dendrites or cell soma; and (c) non-vesicular release from neurons and/or glial cells involving glutamate/cystine antiporter, reversed electrogenic glutamate transporters, purinergic P2X7 receptor pores, and other mechanisms (Massie et al., 2015; Szatkowski et al., 1990; Duan et al., 2003). It is not yet clear whether there is a difference in the firing patterns that determine whether synaptic or non-synaptic glutamate release is evoked, or if any specifically located inputs induce non-synaptic release from different cellular compartments.

Kainate receptors, NMDARs, and mGluRs are more likely to participate in volume transmission than AMPARs. This is due to the low affinity of AMPARs for glutamate, which requires high concentrations of glutamate for activation. Since millimolar concentrations of glutamate are only present within the synaptic cleft following vesicular release, AMPARs are typically located in close proximity to the active zone. However, they can also be found outside of the synapse where they are necessary for efficient trafficking in and out of the synapse. In contrast, NMDARs, KARs, and mGluRs are often located extrasynaptically and mGluRs can also be found on presynaptic terminals where they regulate neurotransmitter release. Volume transmission differs from synaptic signaling with regard to its spatiotemporal features. It is initiated more slowly and lasts longer due to the need for neurotransmitters to diffuse over greater distances to reach their receptors, higher amounts of released glutamate (albeit at lower concentrations) and lower uptake capacity. Volume transmission is also less target-specific and can affect larger groups of cells. (Agnati et al., 2010; Rusakov and Kullmann, 1998; Trueta and De-Miguel, 2012).

Various examples of volume transmission exist, including the activation of extrasynaptic NMDARs or mGluRs by synaptically released glutamate overflow in various brain regions (Papouin and Oliet, 2014; Scanziani et al., 1997), the release of glutamate from Purkinje cells in the cerebellum followed

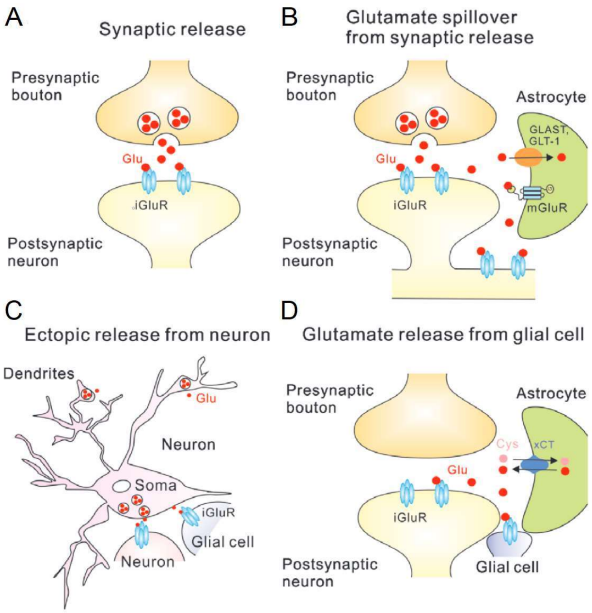

Figure 7. Glutamate release contributing to synaptic signaling and volume transmission.
(A) Synaptic release, (B-D) examples of non-synaptic (volume) transmission. (B) Spillover of glutamate from a synapse to the extrasynaptic receptors on the postsynaptic neurons and astrocytes. (C) Ectopic glutamate release from the somatodendritic compartment. (D) Release of glutamate from astrocytes via glutamate/cystine antiporter. Note that different types of glutamate release are cell and region specific. Abbreviations: Glu, glutamate; Cys, cystine; iGluR, ionotropic glutamate receptor; mGluR, metabotropic glutamate receptor; GLAST and GLT-1, excitatory amino acid transporter (EAAT) 1 and 2, respectively; xCT, glutamate/cystine antiporter. Adapted from: Kula et al., 2019.

by the activation of mGluRs and the subsequent release of endocannabinoids (Duguid et al., 2007), glutamatergic signaling within sensory ganglia where glutamate released from primary sensory neuron cell bodies activates glutamate receptors on both sensory neurons and satellite glial cells (Kung et al., 2013), and so on. The complex functional role of volume transmission is reflected in its various forms. For example, presynaptic extrasynaptic mGluRs modulate synaptic transmission (Scanziani et al., 1997), activity-dependent somatodendritic release of glutamate in the cerebellum dynamically regulates synaptic inhibition (Duguid et al., 2007), and glutamatergic transmission within sensory ganglia may be involved in nociception (Kung et al., 2013). Notably, glutamate that spills out of synapses or is ectopically released can also activate glutamate receptors and transporters on glial cells. In the olfactory bulb, vesicular glutamate release along the axons triggers mGluR-mediated Ca^{2+} transients in olfactory ensheathing glia, leading to the constriction of local blood vessels (Rieger et al., 2007; Thyssen et al., 2010). In the cerebellum, ectopically released glutamate triggers fast synaptic-like currents in Bergmann glia via AMPARs, which may be critical for synaptic integration in the cerebellum since deletion of AMPARs in Bergmann glia leads to the retraction of glial processes from Purkinje cell synapses and impaired fine motor coordination (Matsui and Jahr, 2003; Saab et al., 2012). However, whether glial cells can release molecules and contribute to the modulation of

neuronal signaling in all CNS regions remains controversial (Fiacco and McCarthy, 2018; Savtchouk and Volterra, 2018).

1.16 Glutamatergic synapses between neurons and OPCs

In the hippocampus a significant discovery has been made regarding the activation of glutamate receptors in OPCs in vivo, which involves the establishment of synaptic junctions between neurons and OPCs (Bergles et al., 2000). This neuron-OPC synaptic signaling has been observed in many regions of the brain, as well as in the human white matter (De Biase et al., 2010; Etxeberria et al., 2010; Gallo et al., 2008; Karadottir et al., 2008; Kukley et al., 2007, 2008; Lin et al., 2005; Mangin et al., 2012; Muller et al., 2009; Osterstock et al., 2018; Ziskin et al., 2007). The synaptic junctions between neurons and OPCs exhibit features similar to those found in chemical synapses between neurons. For instance, they display defined structures of pre- and postsynaptic elements, as well as the synaptic cleft. Glutamate release from vesicles at the presynaptic active zone triggers the activation of postsynaptic receptors clustered within the PSD. This process occurs rapidly, and the signaling is terminated quickly, depending on the subtype of iGluRs. These synapses can be triggered by action potentials and are capable of activity-dependent plasticity. Although neuron-OPC synapses have not been thoroughly characterized yet, electron microscopy data reveals the accumulation of synaptic vesicles at presynaptic sites and the presence of electron-dense material in the synaptic cleft, among other features (Bergles et al., 2000; Kukley et al., 2007; Lin et al., 2005; Muller et al., 2009; Sahel et al., 2015; Ziskin et al., 2007). However, the postsynaptic membrane specialization in OPCs appears to be thinner than that of nearby neuronal synapses (Bergles et al., 2000; Harris and Weinberg, 2012).

Research into the release of glutamate at neuron-OPC synapses indicates that, the same as at neuronal synapses, release occurs from vesicles. Electron micrographs of neuronal boutons facing the membrane of OPCs show clusters of vesicles (Bergles et al., 2000; Kukley et al., 2007; Lin et al., 2005; Muller et al., 2009; Sahel et al., 2015; Ziskin et al., 2007). Miniature synaptic currents with fast kinetics can be recorded in OPCs, and each represents the release of a single neurotransmitter-filled vesicle (Del Castillo and Katz, 1954, Bergles et al., 2000; Karadottir et al., 2008; Kukley et al., 2007; Kukley et al., 2010; Nagy et al., 2017; Ziskin et al., 2007). Detection of exocytosis and endocytosis of synaptic vesicles in the corpus callosum using the styryl fluorescent dye FM1-43, which is commonly used to study vesicular exo- and endocytosis at neuronal synapses, further supports this conclusion (Kukley et al., 2007). The frequency of synaptic currents in OPCs can be stimulated by various pharmacological agents that stimulate vesicular exocytosis at neuronal synapses, such as sucrose,

ruthenium red, alpha-latrotoxin, or pardaxin (Bergles et al., 2000; De Biase et al., 2010; Etxeberria et al., 2010; Kougioumtzidou et al., 2017; Wake et al., 2015; Ziskin et al., 2007).

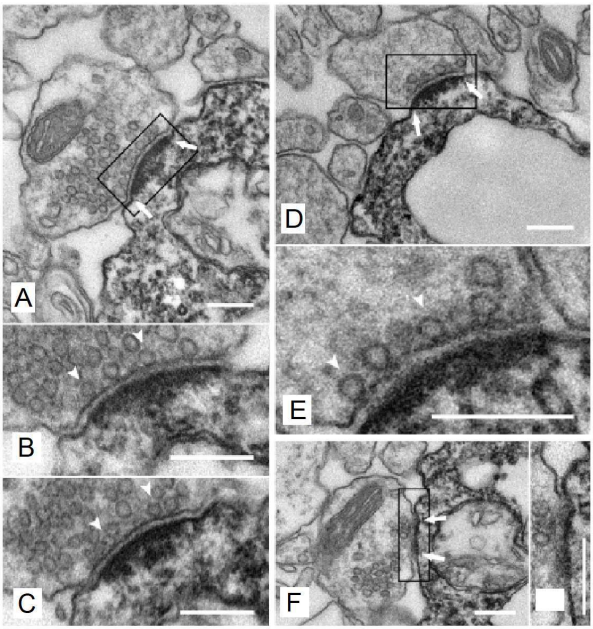

Figure 8. Electron micrographs of biocytin-DAB filled hippocampal OPCs, showing contact points between the OPCs and axons.
(A) Pre-synaptic vesicles, synaptic cleft (marked by arrows), and postsynaptic density at OPC-neuron synapse. OPC stained by DAB reaction product and appear dark in the micrograph. (B) and (C) are higher magnification consecutive sections from boxed region in (A). (D) An example of an asymmetric synapse. (E) Docked pre-synaptic vesicles (indicated by arrowheads). (F) An example of a symetric synapse. The postsynaptic OPC processes' diameter vary between ~200 nm in (A),(D) or more than 1 µm (F). The scale bars are 200 nm. Adapted from: Haberlandt et al., 2011.

Although little is currently known about the properties of the release machinery at neuron-OPC synapses, particularly the presynaptic proteins involved in priming, docking, fusion, filling, and recycling of synaptic vesicles, some proteins involved in exocytosis of synaptic vesicles, such as SNAP25, RaB3, synaptophysin, synaptotagmin-1, synaptobrevin, and syntaxin, were detected in the optic nerve axons using immunohistochemistry (Kukley et al., 2007). Some of these proteins were in close contact with OPC membranes, suggesting that they may be targeted to the release sites at neuron-OPC synapses. VGLUT1 and VGLUT2, which are responsible for pumping glutamate into synaptic vesicles in the pre-synaptic boutons, were also detected in white matter axons next to the processes of OPCs (Etxeberria et al., 2010; Gautier et al., 2015; Sahel et al., 2015; Ziskin et al., 2007).

Glutamate release at neuron-oligodendrocyte precursor cell (OPC) synapses is triggered by action potentials, similar to neuronal synapses. It relies on fast Ca^{2+} entry into the presynaptic boutons and is

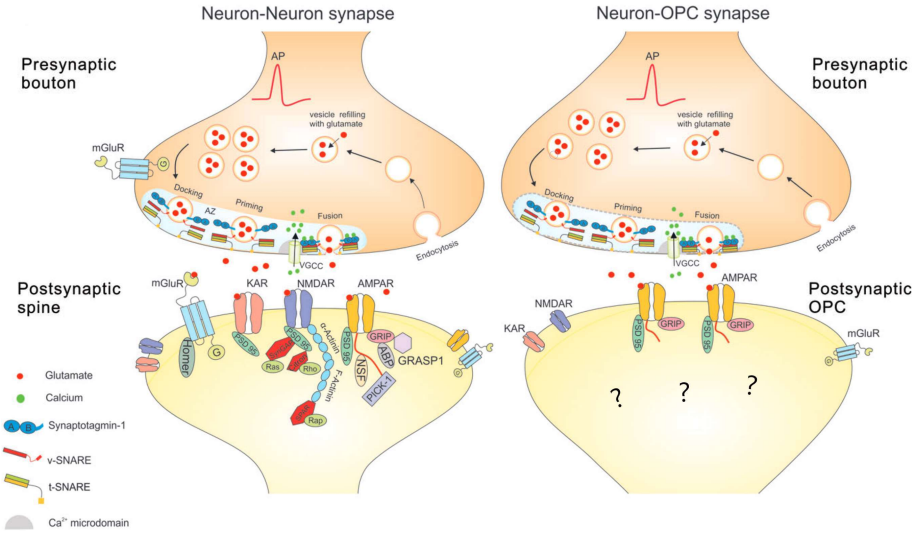

Figure 9. Comparison between neuronal and neuron-OPC synapses.

A simplified drawing of (A) neuron-neuron synapse and (B) neuron-OPC synapse. No data is currently available regarding the features of the presynaptic release machinery and endocytosis mechanisms at neuron-OPC synapses. The hypothetical drawing of the presynaptic terminal in (B) is based solely on electrophysiological findings that describe the neuron-OPC synapses. Only some proteins that interact with postsynaptic glutamate receptors are depicted for neuronal synapse in (A). There is much less information available about the proteins interacting with AMPARs at neuron-OPC synapses compared to neuronal synapses. Note the lack of NMDARs and KARs at an neuron-OPC synapse. Abbreviations: AP for action potential, AZ for active zone, AMPAR for AMPA receptor, NMDAR for NMDA receptor, KAR for kainate receptor, mGluR for metabotropic glutamate receptor, SynGAP for Synaptic Ras GTPase-activating protein, SPAR for spine-associated RapGAP, and VGCC for voltage-gated calcium channel. Adapted from: Kula et al., 2019.

blocked by tetrodotoxin (TTX), cadmium, and specific blockers of P/Q- and N-type Ca^{2+} channels, as well as the Ca^{2+} buffer ethylene glycol-bis(β-aminoethyl ether)-N,N,N',N'-tetraacetic acid (Kukley et al., 2007; Nagy et al., 2017). The amount of Ca^{2+} required for glutamate release at neuron-OPC synapses is dependent on ~2.4th power of Ca^{2+} concentration, which is comparable to values observed for neuronal synapses (Mintz et al., 1995) and suggests that similar Ca^{2+} sensors are involved in both types of synapses.

Studies using electrophysiology to describe neuron-OPC synaptic signaling mediated by AMPARs have shown that the time-course of this signaling is as fast as at neuronal synapses, indicated by the

rapid rise-time (<1 ms) of spontaneous and evoked synaptic currents in OPCs (Bergles et al., 2000; Kukley et al., 2007; Lin et al., 2005; Ziskin et al., 2007). The rise-time is determined by the time required for glutamate to be released, cross the synaptic cleft, and bind to the postsynaptic receptors, triggering the current in the postsynaptic cell. Similarly, the fact that neuron-OPC signaling is terminated quickly is reflected in the fast decay time constant (1.2–1.8 ms) of AMPAR-mediated synaptic currents in OPCs (Bergles et al., 2000; Kukley et al., 2007; Lin et al., 2005; Ziskin et al., 2007).

The distance between the release site and the receptors is small, as postsynaptic AMPARs in OPCs face the presynaptic release sites, similar to neuronal synapses. However, the proteins that compose the postsynaptic density (PSD) complexes and interact with AMPARs at neuron-OPC synapses are largely unexplored. OPCs express mRNAs for PSD-95, glutamate receptor-interacting protein 1 (GRIP1), and Homer1 (Marques et al., 2016; Zhang et al., 2014), which suggests that OPCs may express these proteins and target them to the postsynaptic sites of synapses with neurons. Two PDZ-containing proteins, GRIP1 (Stegmuller et al., 2003) and syntenin (Chatterjee et al., 2008), have been found in OPCs. At neuronal synapses, PDZ-containing proteins act as scaffolds and assemble other postsynaptic proteins, including glutamate receptors, into large complexes (Kim and Sheng, 2004). PDZ-containing proteins may play a similar role at neuron-OPC synapses.

NG2, a transmembrane proteoglycan strongly expressed by OPCs, possesses a PDZ-binding motif QYWV and can interact with various PDZ-containing proteins such as GRIP, syntenin, and MUPP1 (Barritt et al., 2000; Chatterjee et al., 2008; Stegmuller et al., 2003). GRIP is known to bind to GluA2/3-subunit-containing AMPARs, and it is postulated that the NG2-GRIP-GluA2/3 complex may play a role in regulating the clustering of AMPARs and thereby modulating synaptic signaling between neurons and OPCs. However, despite this potential function, it was found that knockout of NG2 did not affect the synaptic currents in hippocampal OPCs (Passlick et al., 2016). Thus, the functional significance of the NG2-GRIP-GluA2/3 complex at neuron-OPC synapses remains a topic of investigation.

Syntenin, another PDZ-protein found in OPCs, is believed to play a role in regulating neuronal communication by facilitating the proper localization of receptors at synapses (Beekman and Coffer, 2008). It is possible that syntenin may have a similar function at neuron-OPC synapses. MUPP1, another PDZ-containing protein that interacts with NG2 proteoglycan in vitro, is known to regulate p38 MAP kinase activity and AMPAR trafficking at neuronal synapses (Krapivinsky et al., 2004). Moreover, PSD-95 was recently identified as colocalizing with synapsin in processes of Zebrafish embryo OPCs (Li et al., 2023).

In addition to PDZ-containing proteins, OPCs also express several TARPs that play a crucial role in the delivery and regulation of AMPARs, which is also observed in neurons (Greger et al., 2017; Zonouzi et al., 2011). Despite discrepancies in the transcriptome and immunohistochemical data regarding the types of TARPs present in OPCs (Cahoy et al., 2008; Marques et al., 2016; Zhang et al., 2014; Zonouzi et al., 2011), interaction with TARPs is critical for the proper functioning of AMPARs in OPCs.

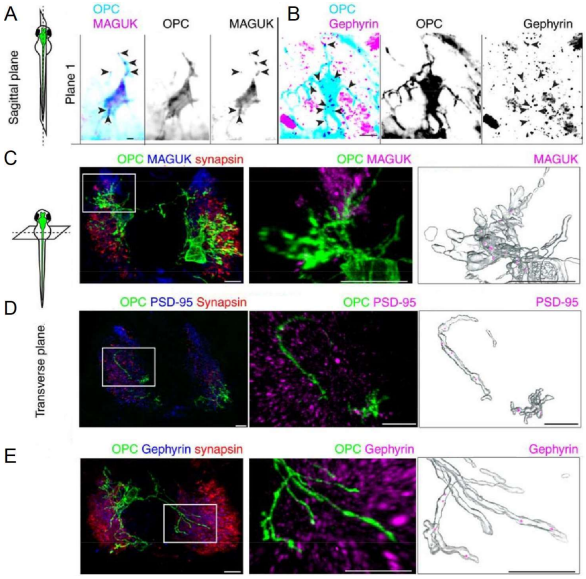

Figure 10. Synaptic markers at OPC synapses in Zebrafish. (A) IHC staining for MAGUK in a sagittal-plane spinal cord at 3 days post fertilization (3 dpf) in Tg(sox10:GFP-caax) Zebrafish embryo. Arrows indicate colocalization between GFP (cyan) and MAGUK (magenta). (B) IHC staining for gephyrin in a sagittal-plane spinal cord, as in (A). Arrows indicate colocalization between GFP (cyan) and gephyrin (magenta). (C) On the left: IHC staining for MAGUK (blue) and synapsin (red) in a transverse plane in the Tg(olig1:Kalta4,10xUAS:myrGFP) spinal cord at 3 dpf. In the center an OPC (green) with colocalizations of MAGUK (magenta) in the magnified region. On the right: 3D reconstruction of the OPC with MAGUK colocalizations. (D) On the left: IHC staining for PSD-95 (blue) and synapsin (red) in a transverse plane, as in (C). In the center an OPC (green) with colocalizations of PSD-95 (magenta) in the magnified region. On the right: 3D reconstruction of the OPC with PSD-95 colocalizations. (E) On the left: IHC staining for gephyrin (blue) and synapsin (red) in a transverse plane, as in (C). In the center an OPC (green) with colocalizations of gephyrin (magenta) in the magnified region. On the right: 3D reconstruction of the OPC with gephyrin colocalizations. Adapted from: Li et al., 2023.

Neuron-OPC synapses are similar to neuronal synapses in many respects, such as undergoing long-term potentiation (LTP) in the hippocampus (Ge et al., 2006). LTP is an activity-dependent modification of synaptic strength and involves Ca^{2+}-permeable AMPARs in OPCs. This is different from many neuronal synapses, where LTP induction is not accompanied by increased Ca^{2+}-permeability of AMPARs. Although there are likely to be differences between neuron-OPC synapses and neuronal

synapses, the diversity of the latter and the limited knowledge of the presynaptic release machinery and PSD complexes at neuron-OPC synapses makes it challenging to define specific distinctions between the two types of synapses.

1.17 KARs in OPC

According to transcriptional analysis, all five subunits of Kainate receptors (KARs) are present in OPCs (Cahoy et al., 2008; Larson et al., 2016; Marques et al., 2016; Zhang et al., 2014). KAR proteins have also been detected in oligodendrocyte-type 2 astrocytes (O-2A cells), which are thought to be OPCs (Patneau et al., 1994). Furthermore, functional KAR proteins have been identified in hippocampal OPCs. This was demonstrated by recording an inward current in OPCs in brain slices upon low concentrations of kainate application, while AMPAR and NMDAR antagonists were present (Kukley and Dietrich, 2009).

However, it is unclear whether glutamate released from neurons activates KARs in OPCs. In cerebellar OPCs, KARs do not contribute to synaptic current triggered by electrical stimulation of axons, as this current is completely blocked by the specific AMPAR antagonist GYKI53655 (Lin et al., 2005). This suggests that KARs in OPCs are extrasynaptic and may require spillover of glutamate from the synaptic cleft to become activated during prolonged neuronal firing. Alternatively, KARs in OPCs may be located away from the release sites of neuron-OPC synapses and could be activated by ectopic release of glutamate from neurons or other cells.

1.18 NMDARs in OPCs

The explant culture of O-2A cells, OPCs cultures, and OPCs isolated from the brain were found to express several NMDAR subunits, including the obligatory subunit GluN1 (Li et al., 2013; Marques et al., 2016; Wang et al., 1996; Zhang et al., 2014). Functional NMDAR proteins were detected in OPCs through patch-clamp recordings in both culture and brain slices, suggesting that they may mediate Ca^{2+} elevations in these cells (De Biase et al., 2010; Karadottir et al., 2005; Wang et al., 1996; Ziskin et al., 2007). However, NMDARs only allow minimal current flow near the resting membrane potential, which is about -90 mV in OPCs, even with the application of saturating concentrations of agonists, because Mg^{2+} blocks the channel pore and strongly reduces the current (De Biase et al., 2010; De Biase et al., 2011; Karadottir et al., 2005; Ziskin et al., 2007). Therefore, under physiological conditions in vivo, NMDARs in OPCs may only become activated when the cell is depolarized through other means, such as by prior activation of AMPARs. While NMDARs in cerebellar OPCs do not contribute to synaptic currents elicited by axonal stimulation, even when Mg^{2+} block is removed at a holding potential of +40 mV, suggesting that these receptors are located away from the release sites at

neuron-OPC synapses. It is still unknown whether NMDARs in OPCs can be activated by glutamate spillover from synapses during repetitive neuronal activity or by ectopic release of glutamate from neurons or glial cells.

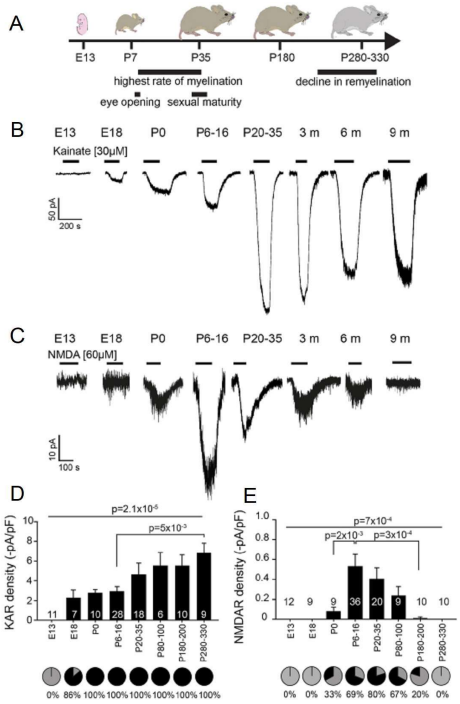

Figure 11. OPC NMDAR- and KAR-mediated currents at different developmental time-points.
(A) The developmental and myelination-related milestones in mice are represented by a schematic diagram, denoting the period of the study. (B) Currents evoked by 30 μM Kainate applied through bath, recorded in OPCs across different age groups, ranging from E13 to 9 months old. (C) Currents evoked by 60 μM NMDA applied through bath, recorded in OPCs across different age groups, ranging from E13 to 9 months old. (D) Changes in the density of KARs with age, and the proportion of OPCs exhibiting detectable KA-evoked currents. (E) Changes in the density of NMDARs with age, and the proportion of OPCs exhibiting detectable NMDA-evoked currents. Adapted from: Spitzer et al., 2019.

1.19 mGluRs in OPCs

Several mGluR subunits were detected in OPCs through transcriptional analysis (Larson et al., 2016; Luyt et al., 2003; Marques et al., 2016; Zhang et al., 2014). Immunohistochemistry, immunoblotting, and Ca^{2+} imaging have been used to detect mGluR proteins in OPCs, but the results do not always align with transcriptional analysis. In the OPC CG-4 cell line, mGluR5 and mGluR3 are expressed, where mGluR5 activation induces Ca^{2+} oscillations and mGluR3 activation inhibits cAMP formation (Holtzclaw et al., 1995; Luyt et al., 2003; Luyt et al., 2006). In primary cultures of OPCs, mGluR1, mGluR2/3, mGluR4, and mGluR5 proteins are expressed, but they all downregulate upon OPC differentiation into OLs (Deng et al., 2004; Spampinato et al., 2014). Activation of

mGluR1/mGluR5 triggers Ca^{2+} elevations in OPCs in hippocampal slices (Haberlandt et al., 2011), which is in line with the fact that Group I mGluRs promote production of IP3 via stimulation of phospholipase-C and induce Ca^{2+} release from internal stores (Niswender and Conn, 2010). mGluR-mediated Ca^{2+} signaling regulates surface expression of Ca^{2+} permeable AMPARs in OPCs and may also promote their incorporation to the postsynaptic sites of neuron-OPC synapses (Zonouzi et al., 2011). This suggests that mGluRs regulate plasticity at neuron-OPC synapses.

To date, studies on mGluRs in OPCs have utilized specific receptor agonists for activation, which were administered for extended periods ranging from several seconds to over 10 minutes (Haberlandt et al., 2011; Zonouzi et al., 2011, Spitzer et al., 2019). However, it remains unclear whether this approach accurately reflects the in vivo situation. Additionally, no experiments have been conducted to determine whether axonal stimulation can induce mGluR-mediated Ca^{2+} transients or ionic currents in OPCs, nor is it known whether mGluRs in OPCs are activated by synaptic or non-synaptic release of glutamate from axons. Notably, in neurons, postsynaptic mGluRs are typically located extrasynaptically (Lujan et al., 1996; Niswender and Conn, 2010), and repetitive neuronal activity resulting in a higher quantity of released glutamate is typically required to activate mGluRs (Sherman, 2014), although this can vary between synapses (Viaene et al., 2013). As a result, various paradigms of neuronal stimulation should be tested to determine how mGluRs are activated in OPCs. Moreover, identifying the subcellular localization of mGluRs in OPCs using electron microscopy may provide additional insights into the mechanisms of activation and functional roles of the receptors.

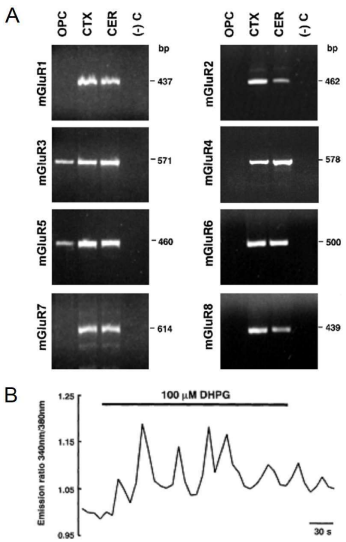

Figure 12. The first mGluR transcripts detected in CG-4 OPC.
(A) Receptor-specific primers were used to detect mRNAs of all mGluR receptor subtypes in CG-4 OPCs (OPC). mRNA prepared from rat cerebral cortex (CTX) and cerebellum (CER) served as the positive controls. PCR reactions performed without template: (–) C were negative control. Restriction enzyme digestion patterns were used to verify PCR products. The sizes of the PCR products are indicated on the right. (B) Time course of Ca^{2+} transients elicited in CG-4 OPCs by bath applications of mGluR agonist DHPG. Adapted from Luyt et al., 2003.

1.20 Functional role of glutamate receptors and glutamatergic signaling between neurons and OPCs

Glutamate is a crucial neurotransmitter that is released during neuronal activity. It has been suggested that glutamate receptors may be responsible for mediating the effects of neuronal activity on OPCs in vivo. Several studies have provided evidence that glutamate receptors play a role in the physiology of OPCs both in vitro and in vivo. However, the relationship between neuronal activity and OPC behavior is not yet fully understood. It is currently unclear whether the observed effects of neuronal activity on OPCs are indeed mediated by iGluRs and mGluRs, and which downstream mechanisms are involved in glutamate receptor activation.

1.21 Functional role of AMPARs in OPCs

OPCs' proliferation and differentiation are influenced by AMPARs. Glutamate, AMPA, or kainate added to cell and tissue cultures reduces the number of proliferating OPCs and/or halts their lineage progression (Gallo et al., 1996; Liu and Almazan, 1995; Yuan et al., 1998). The effects can be reversed or even trigger opposite effects by adding antagonists of AMPARs/KARs, alone or together with agonists (Fannon et al., 2015; Gallo et al., 1996; Liu and Almazan, 1995; Yuan et al., 1998). Hence, it can be postulated that activating AMPARs inhibits OPCs' proliferation and differentiation. However, it's surprising that dividing OPCs receive AMPAR-mediated glutamatergic synaptic input from neurons (Ge et al., 2009; Kukley et al., 2008). The discrepancy between these observations may be due to the mechanism of agonist effects on AMPARs in OPCs. When synaptic glutamate is released, AMPARs in OPCs are exposed to agonists briefly (a few milliseconds at most), while in vitro exposure is sustained (several hours), leading to AMPAR desensitization (Robert and Howe, 2003). Furthermore, prolonged exposure of OPCs and Oli-neu cells to AMPAR agonists leads to downregulation of AMPAR subunits, especially those that make AMPARs Ca^{2+}-permeable (Begum et al., 2018; Hossain et al., 2014; Jourdi et al., 2005; Mangiavacchi and Wolf, 2004). Therefore, the observed decrease in OPCs' proliferation and lineage progression upon prolonged exposure to AMPAR agonists in vitro may be due to reduced Ca^{2+} entry, which is crucial for proliferation and differentiation regulation (Hamilton, Hubbard, and Butt, 2009; Toth, Shum, and Prakriya, 2016; Yang et al., 2013). Interestingly, reducing the influx of Ca^{2+} into OPCs is feasible even if AMPARs that are Ca^{2+}-impermeable are downregulated because it prevents the opening of L-type VGCCs that are triggered by AMPAR-mediated depolarization (Sun et al., 2016). The precise functional role of AMPARs in OPCs in vivo is not well-established. However, some studies have demonstrated that boosting the Ca^{2+} permeability of AMPARs by targeting the GluA2 subunit in newly-generated OPCs at the height of myelination results in increased proliferation and reduced differentiation of OPCs (Chen et al., 2018).

On the other hand, lineage-specific deletion of GluA2 or both GluA2 and GluA4 on a germline GluA3 null background that eliminates AMPAR-mediated synaptic input to OPCs during development did not affect OPC proliferation or number but resulted in a 25-30% reduction in the number of mature OLs and myelin sheaths that were formed in subcortical white matter due to enhanced apoptosis of newly differentiating OLs (Kougioumtzidou et al., 2017). The downstream molecular pathways involved in these findings are yet to be determined, but the GluA2 subunit is of particular interest as its expression in OPCs varies depending on the animal's age and brain region, and even within the same brain region (Bergles et al., 2000; Chen et al., 2018; Ge et al., 2006; Kukley et al., 2007; Ziskin et al., 2007). Furthermore, the expression of the GluA2 subunit in OPCs is regulated by mGluRs and ATP (Zonouzi et al., 2011), implying that this subunit is modulated in an activity-dependent manner.

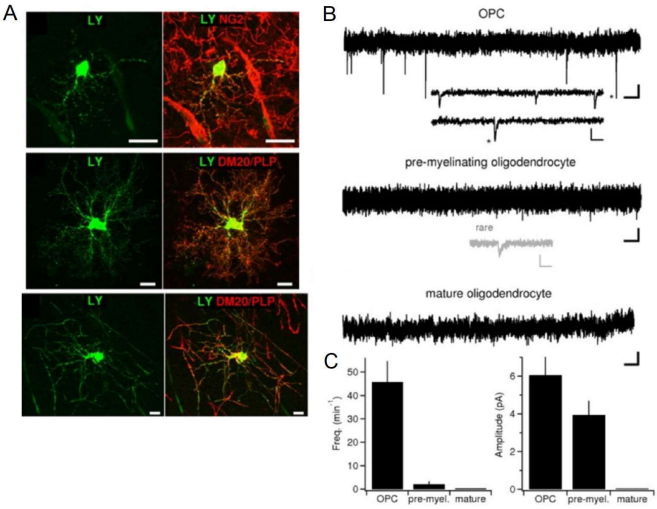

Figure 13. Synaptic currents are abolished during OPC lineage progression.
(A) Lucifer Yellow filled OL lineage cells (left), co-labeled with lineage markers (right): NG2 as a marker of OPCs, DM20/PLP marking pre-OLs and mature OLs. Mature OLs are recognized by developed myelin sheaths. (B) Ruthenium Red bath application induces mEPSCs in OPCs, rare events are visible in pre-OL and are not found in mature OLs. Scale bars: 0.2 s, 2 pA. In the insets: Expended traces showing mEPSC waveforms. Inset scale bars: 20 ms, 5 pA. The asterisks mark the same events. (C) Summary graphs comparing the mean frequencies of mEPSCs (left) and summary graph comparing the mean amplitude of mEPSCs recorded from OL lineage cells. Adapted from Kukley et al., 2010.

AMPARs not only modulate the proliferation and differentiation of OPCs but also play a crucial role in regulating their migration and cytoarchitecture. In the presence of AMPA and cyclothiazide, which prevent desensitization of AMPARs, αv integrin-dependent migration of OPCs with simple bipolar morphology is significantly increased in purified OPC cultures and organotypic cerebellar slices (Gudz et al., 2006; Harlow et al., 2015). Several mechanisms may underlie this effect, including the formation of a complex between AMPAR subunits, αv integrin, and proteolipid protein, AMPAR-mediated stimulation of phospholipase C, and internalization of the GluA2 subunit with a subsequent increase in Ca2+ permeability of AMPARs and the frequency of Ca^{2+} transients in OPCs (Gudz et al., 2006; Harlow et al., 2015). However, the relationship between Ca^{2+} level and migration is not fully understood, as some studies suggest that Ca^{2+} stimulates motility while others propose that Ca^{2+} arrests cell movement and triggers maturation (Toth et al., 2016).

Moreover, AMPARs also affect the structural appearance of OPCs with complex morphology. Blocking AMPARs with specific antagonists in cerebellar slice culture leads to a significant reduction in the total length of OPC processes and affects the number of branching points (Fannon et al., 2015). Therefore, it is likely that the morphological complexity of OPCs in vivo is supported by glutamatergic signaling involving AMPARs, as has been proposed for other cells, such as retinal microglia (Fontainhas et al., 2011).

1.22 Functional role of KARs

Functional role of KARs is unknown.

1.23 Functional role of NMDARs

The role of NMDARs in regulating OPC functionality is not well established. While some studies have found no involvement of NMDARs in OPC regulation (Fannon et al., 2015; Yuan et al., 1998), others suggest that NMDARs influence OPC behavior. For example, blocking NMDARs prevents O-2A cell migration (Wang et al., 1996), while NMDA application promotes migration of rat cortical OPCs, an effect dependent on GluN1 and GluN2A subunits (Xiao et al., 2013). Activation of NMDARs may promote an immature phenotype in OPCs due to their role in promoting migration, which is a characteristic of developing cells. However, NMDARs also play a role in promoting OPC maturation in vitro by increasing myelin basic protein expression, enhancing OPC process branching complexity, and stimulating differentiation (Li et al., 2013). Blockage of NMDARs in cerebellar slices reduces OPC differentiation (Fannon et al., 2015). Downstream of NMDARs, the mTOR pathway may play a role in promoting OPC differentiation (Li et al., 2013).

In vivo studies indicate that inducible ablation of the obligatory GluN1 subunit of NMDARs in OPCs does not affect OPC proliferation, density, or differentiation, nor does it affect myelination in the gray or white matter of the brain (De Biase et al., 2011; Guo et al., 2012). In an animal model of multiple sclerosis, deletion of the GluN1 or GluN3 subunit of NMDARs also does not affect disease severity (Guo et al., 2012). Interestingly, functional deficiency of NMDARs leads to an increase in the Ca^{2+} permeability of AMPARs in OPCs by changing the subunit composition of AMPARs (De Biase et al., 2011). This suggests that a dynamic interplay exists between NMDARs and AMPARs to ensure Ca^{2+} entry in response to neuronal activity or other mechanisms activating iGluRs in OPCs.

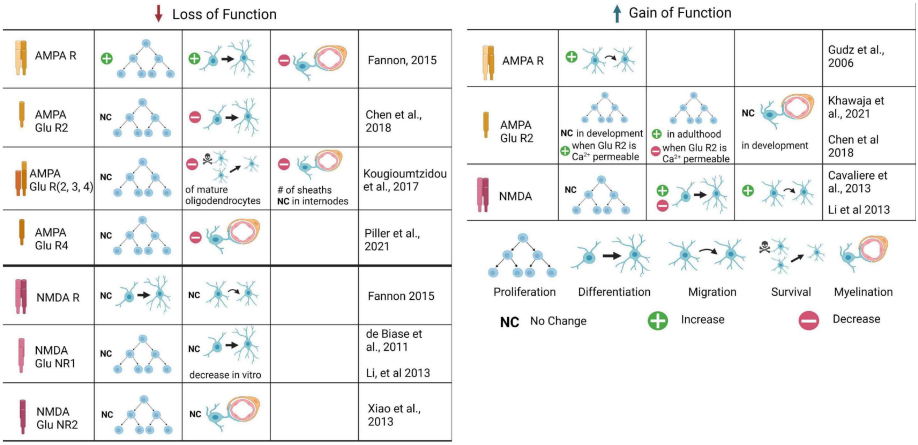

Figure 14. Summary of the role of glutamatergic receptors in OPC development and myelination.
Gain and loss of function experiments in connection to changes in OPC proliferation, differentiation, migration, survival, and myelination. Loss of function experiments have been performed on several subunits of the AMPA and NMDA receptors. Gain of function experiments are limited to AMPA, AMPA GluR2, NMDA. If the process was not tested, it is not included for that receptor, while no change is noted if the process was tested but no differences were found. In cases where conflicting results were obtained, both outcomes are listed for that particular receptor. Adapted from: Moura et al., 2022.

1.24 Functional role of mGluRs

Currently, only a few functions of mGluRs in OPCs are understood. One known function is that the activation of mGluR4 with a specific agonist promotes differentiation of OPC in vitro (Spampinato et al., 2014). Additionally, mGluRs may play a role in the regulation of molecules released by OPCs. Specifically, it was reported that mGluR-induced release of BDNF occurred in cultured cortical

oligodendrocyte lineage cells (Bagayogo and Dreyfus, 2009), although it is unclear whether these cells were OPCs or OLs. Interestingly, a complex interplay between mGluRs and iGluRs occurs in OPCs. For example, in the CG4 OPC cell line, activation of mGluR5 increases Ca^{2+} permeability and single channel conductance of AMPARs (Zonouzi et al., 2011). Similar changes in Ca^{2+} permeability of AMPARs were seen in immature OPCs isolated from the optic nerve, but not in the premyelinating OPCs (Zonouzi et al., 2011). This indicates that regulation of AMPARs by mGluRs depends on the developmental stage of the oligodendrocyte lineage cells. Downstream of mGluR5, the synthesis of new Ca2+-permeable AMPARs is induced via an increase in intracellular Ca^{2+} level in OPCs, involving PI3 kinase, PICK-1, and the JNK pathways (Zonouzi et al., 2011). mGluRs also regulate survival of OPCs under pathological conditions. For example, in vitro, activation of group I mGluRs enhances survival of OPCs upon excitotoxic kainate exposure, or during oxidative stress triggered by oxygen–glucose deprivation, and this effect is attributed to the decreased accumulation of reactive oxygen species (Deng et al., 2004; Kelland and Toms, 2001). Additionally, activation of mGluR5 prevents OPCs from undergoing staurosporine-induced apoptosis (Luyt et al., 2006).

1.25 OPCs are the major cycling population of the CNS

The presence and abundance of OPCs in various regions of the brain have been extensively studied. Studies have shown that OPCs are distributed throughout the brain from the time of birth, and are present in both gray matter and white matter (Nishiyama et al., 1996; Dimou et al., 2008; Rivers et al., 2008). Moreover, OPCs are found as proliferative cells in every region of the brain, at all studied ages (Dawson et al., 2000; Horner et al., 2002; Nishiyama et al., 2002; Aguirre and Gallo, 2004). This indicates that the role of OPCs is not limited to specific regions of the brain, but instead they are essential for brain development and function as a whole.

The fraction of actively cycling OPCs (growth fraction) is high in both young and adult animals (Kukley et al., 2008; Psachoulia et al., 2009). Kukley et al. (Kukley et al., 2008) estimated the growth fraction of NG2 glia in the mouse hippocampus at postnatal days 9 and 11, and found that it was as high as 48% and 49%, respectively. In order to estimate the growth fraction of OPCs, they performed a double staining for NG2 and the proliferating cell nuclear antigen (PCNA), which is only detected in cycling but not in resting cells. Psachoulia et al. found that the growth fraction of OPCs in the corpus callosum and cerebral cortex of 2-18-month-old mice was approximately 46% and 39% respectively, indicating that approximately half of all OPCs are constantly dividing, independently of the brain area and the age of the animals.

As animals grow into adulthood, the density of OPCs decreases (Nishiyama et al., 1996; Vélez-Fort et al., 2009) and the absolute number of cycling OPCs declines (Panagiotakos et al., 2007;

Vélez-Fort et al., 2009). However, the fraction of actively cycling OPCs changes only slightly with age, indicating that OPCs are constantly dividing throughout the lifespan of an animal (Psachoulia et al., 2009). Remarkably, recent findings indicate that all NG2+ cells in the mature brain, regardless of region, have the ability to divide (Kang et al., 2010). This suggests that the total number of cycling OPCs in the brain may be even higher than previously estimated, indicating that OPCs play a crucial role in maintaining the homeostasis of the brain throughout the lifespan of an animal.

Studies using BrdU labeling and immunohistochemistry have shown that OPCs make up approximately 70% of BrdU-positive cells in the adult cerebral cortex, hippocampus, corpus callosum, and spinal cord after a short BrdU pulse, indicating that they are the major cycling cell population in the rodent brain parenchyma (Horner et al., 2000; Dawson et al., 2003; Polito et al., 2005; Lasiene et al., 2009). Furthermore, research has found that virtually all cells (≥ 90%) incorporating BrdU in the brain parenchyma represent OPCs, based on BrdU labeling, immunohistochemistry, and/or transgenic mice where NG2 or Olig2 cells are labeled (Alonso, 2000; Dayer et al., 2005; Mori et al., 2009; Dimou et al., 2008). This cycling population of NG2+/Olig2+ cells is also prevalent in the healthy adult human brain (Geha et al., 2010).

Interestingly, OPCs display a striking discrepancy in cell cycle time, with the cell cycle time of OPCs in the hippocampus, cerebral cortex, and corpus callosum being approximately 2-3 days during the first two postnatal weeks. This means that each cycling NG2 cell divides approximately every 48-72 hours. As the animal matures, cell cycle time increases steadily, reaching over 100 days at P540. The rate of oligodendrocyte production from OPCs slows down in parallel with the increase in OPCs' cell cycle duration. For example, in the corpus callosum, the cell cycle slows down by about 10-fold between P45 and P240, while the rate of oligodendrocyte production slows down by about 20-fold during the same period (Psachoulia et al., 2009).

1.26 OPCs maintain their complex morphology and synaptic connections during cell division

OPCs in the grey and white matter of rodent brains possess complex morphology, with highly branched processes extending over 100 µm around a small cell body in radial (grey matter) or bipolar (white matter) shape. While approximately 50% of OPCs in both neonatal and adult brains are actively involved in the cell cycle, it is unclear how cell morphology changes during this process. To address this question, individual hippocampal OPCs with mitotic DNA configuration were subjected to patch-clamp recordings and filled with a fluorescent dye, Lucifer Yellow. Subsequent morphological analysis of these dye-filled cells showed that metaphase and telophase OPCs maintained a rich tree of branching processes. Similar findings were reported by Ge et al., who examined mitotic glial cells

labeled for NG2 in brain slices. Although these findings suggest that OPCs retain their complex morphology during division, it is possible that the cells retract and regrow some of their processes quickly, such as in the range of minutes, and withdraw many of their processes during chromosome separation. Time-lapse imaging of zebrafish OPCs in vivo demonstrated that cells can rapidly remove filopodia-like processes, divide, re-grow their processes, and migrate away from each other. However, time-lapse imaging of mammalian OPCs in vivo has not yet been reported. Ge et al. attempted to perform time-lapse imaging of dividing OPCs in acute mouse brain slices and observed that the soma of the mother cell split into two while all of the processes remained un-retracted, supporting the idea that OPCs retain their complex morphology during mitosis. However, this observation was based on only a single example, and further experiments involving time-lapse imaging in transgenic mice specifically labeled for NG2 cell soma and processes would be necessary to investigate this issue further.

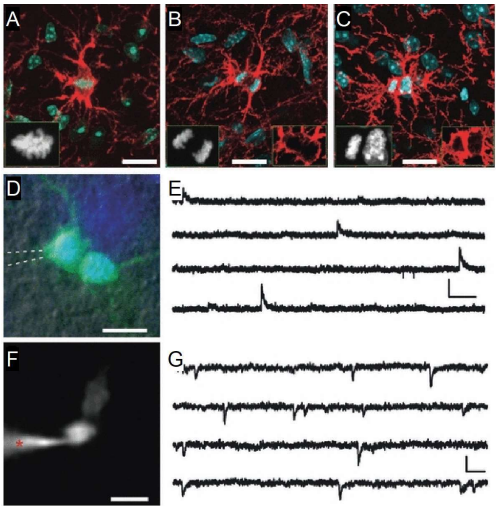

Figure 15. OPCs maintain functional synapses during mitosis.
(A–C) Three OPCs at different stages of cell division: metaphase (A), anaphase (B) and telophase (C), labeled by DAPI (blue) and NG2 antibodies (red) in brain slices prepared from P25 mouse. Note that mitotic cells possess a fully branched morphology at all mitotic stages. Scale bars = 20 µm (A–C). Insets show DAPI and NG2 only. (D) Dividing OPC filled with Lucifer Yellow (green), with mitotic chromatin configuration labeled with Hoechst 33342 (blue) in a live brain slice. Dashed white lines indicate the patch-pipette. Scale bar = 10 µm. (E) GABAergic synaptic currents recorded from the cell (Vh = +30 mV), in the presence of 30 µm CNQX and 100 µm ruthenium red. Scale bar: 400 ms, 20 pA. (F) Mitotic OPC cell filled with Cy5-conjugated dextran (10 kDa) during patch-clamp recordings. Dextran (10 kDa) does not spread through gap junctions, therefore both cells must share the cytoplasm for the filling to be successful. Asterisk indicates the patch-pipette. Scale bar = 10 µm. (G) Glutamatergic synaptic currents recorded from the cell (Vh = −80 mV), in the presence of 10 µm bicuculline. Scale bar: 20 ms, 10 pA. Adapted from: Fröhlich et al., 2011.

Patch-clamp recordings were used to investigate synaptic responses directly in proliferating cells. Mitotic OPCs in metaphase or telophase of mitosis were studied in acute hippocampal and cortical

slices from neonatal mice aged 7-12 days old. GABAergic synaptic currents were detected in OPCs with mitotic chromosome configurations in the presence of AMPA/kainate receptor antagonist CNQX. Fast rising and decaying excitatory postsynaptic currents could be recorded in OPCs during metaphase and telophase of mitosis on removal of AMPA/kainate receptor antagonists and adding GABAA receptor antagonist bicuculline. Recent data shows that grey and white matter OPCs in metaphase and telophase of mitosis receive glutamatergic synaptic input from neurons not only in young but also in older animals. Electron microscopy images show that synaptic terminals contact mitotic OPCs, suggesting that during cell division at least some synaptic contacts are maintained.

Based on this evidence, it seems likely that OPCs in the rodent brain can enter cell cycle and undergo cell division without losing functional GABAergic and glutamatergic synapses (Kukley et al., 2008). While the evidence so far is indirect, the frequency of synaptic currents is comparable between metaphase and telophase OPCs (Kukley et al., 2008), suggesting that the number of functional synaptic contacts of the parent cell is comparable with the number found in two daughter cells. In addition, the number of GAD65+ terminals in each daughter NG2 cell is roughly half of the synaptic terminals found in the parent cell (Kukley et al., 2008) If OPCs have to disassemble all synapses before cell division and reform all of them from scratch after cytokinesis, there should be a period of time equal to at least 1 h when synaptic currents are absent in OPCs. However, synaptic currents could be recorded in OPCs presumably 30 min before and after chromosome segregation.

Newly generated OPCs in the postnatal rodent brain can inherit synapses from their parent cell, which raises questions about the benefits of this process. One possible advantage of keeping synaptic contacts with dividing OPCs is that neurons may have the opportunity to directly or indirectly regulate the proliferation of OPCs. For instance, they could influence the expression of potassium channels during the cell cycle or control other intracellular signaling cascades. Additionally, inheriting synapses could enable the direct transfer of environmental interactions to clonal descendants of OPCs, which could be crucial for effective colonization and perhaps future myelination of the developing brain.

The discovery of glutamatergic innervation of dividing OPCs by Kukley et al. and Ge et al. re-opened an essential question regarding the role of glutamate and its receptors for proliferation of oligodendrocyte lineage cells. This question was first addressed more than 20 years ago by Gallo et al. and Yuan et al., who conducted work in dissociated cell cultures and organotypic slice cultures. Their studies showed that glutamate acts through AMPA/kainate receptors to inhibit O-2A progenitor (presumably OPCs) proliferation. They suggested that this effect is mediated by the increase in intracellular Na^+ concentration triggered by the opening of the AMPA channels in the O-2A membrane, and subsequent block of voltage-gated K^+ channels. However, recent research has revealed that

glutamate released from neurons activates AMPA/kainate receptors on dividing OPCs in acute brain slices.

The question that arises is how OPCs receiving glutamatergic synaptic input can divide if glutamate inhibits proliferation. In the earlier studies, agonists and antagonists of glutamate receptors were added to the culture medium for 1-48 hours, which means that cells were constantly exposed to these substances for a prolonged period of time. Glutamatergic synaptic-like signaling between neurons and OPCs under physiological conditions is a much finer 'tool' for exposing glial cells to glutamate and activating their glutamate receptors. Importantly, glutamatergic synaptic signaling can be tuned in time and space both pre- and postsynaptically, and it can perhaps be tuned during the cell cycle of OPCs.

For example, AMPA receptor expression in OPCs and/or properties of the axonal release machinery could be higher in G1 phase and decreasing in G2/M phase, thereby allowing NG2 cell division. Blocking AMPA/kainate receptors and subsequent increase in cell proliferation described by Yuan et al. would be an extreme of this situation. However, it is not yet known whether and how the surface expression of neurotransmitter receptors on OPCs, the number and properties of synapses, the location of synapses along NG2 cell processes, and the strength of synaptic input change during the cell cycle of an NG2 cell. Therefore, there is still much to be discovered regarding whether and how glutamatergic synaptic signaling between neurons and glia regulates the proliferation of OPCs.

2. Hypothesis, objectives and experimental strategy

2.1 Hypothesis

The major hypothesis of this study is that OPC synapses follow similar developmental patter to neuronal synapses. We hypothesize that juvenile OPCs have synapses with characteristics of immature neuron-neuron synapses and that during callosal development those properties change into ones typical for mature neuron-neuron synapses at adulthood. We hypothesize that synaptic development and increased synaptic activity is reflect in more complex morphology of OPC in adulthood when compared to juvenile OPCs.

2.2 Objectives

To test my hypothesis, I followed four objectives.

1) Establish an approach to probe intrinsic electrophysiological properties of OPC through whole-cell patch clamp at three distinct callosal developmental stages.

2) Establish an approach to probe properties of the synaptic input onto OPCs by investigating the quantal size (q), release probability (p) and number of release sites (N), in line with the classical theory of synaptic strength (I) : $I = pqN$.

3) Establish methodology to sparsely label callosal OPC at three distinct callosal developmental stages. Identify, acquire and reconstruct whole OPCs from confocal stacks.

4) Reconstruct whole OPC morphology and analyze branching, overall process structure, branch position in space and the effects of callosal development on morphological properties of the cell at three distinct callosal developmental stages.

2.3 Experimental strategy

1) Voltage-clamp patched callosal OPCs and subject the cells to a set of 200-300 µs square voltage steps, in +10mV increments, starting a V_h=-80. From the steps acquire values of R_m, C_m, Na_v and K_v channel currents.

2) Voltage-clamp callosal OPCs and elicit evoked, AMPA-ergic, synaptic currents by stimulating the callosal fibers with trains of stimuli, applied at different frequencies and of different magnitudes (minimal and maximal stimulation paradigms).

3) Sparsely label callosal OPCs by inducing Cre activity in postnatal ROSAmT/mG:NG2-CreERTM double-transgenic mice with injection of 4-hydroxytamoxifen. Inject 1 mg of 4-OHT per gram of body weight intraperitoneally 3 days ahead of tissue harvesting. Afterwards, prepare coronal brain sections and immunostain for NG2, GFP and DAPI. Image the sections at Zeiss LSM 710 Meta Confocal microscope and acquire stacks containing whole cells.

4) Upload confocal image stacks into Neurolucida. Manually trace the processes to generate single pixel-thick reconstructions. Analyze the cells in the Neurolucida software.

3. Materials and Methods

3.1 Ethics statement

All experiments were performed in accordance with current European Union guidelines and approved by the local government authorities for Animal Care and Use (Regierungspraesidium Tuebingen, State of Baden-Wuerttemberg, Germany). All efforts were made to minimize the suffering of the animals.

3.2 Animals

For the electrophysiological experiments heterozygous progeny of NG2DsRedBAC transgenic and C57BL/6 mice were used in this study. Breeding pairs of NG2DsRedBAC transgenic mice were originally obtained from The Jackson Laboratory (stock 008241) and C57BL/6 mice were originally obtained from Charles River.

For the immunohistochemistry (IHC) and analysis of morphology the progeny of B6.129(Cg)-Gt(ROSA)26Sor$^{tm4(ACTB-tdTomato,-EGFP)Luo}$/J (ROSA$^{mT/mG}$) and B6.Cg-Tg(Cspg4-cre/Esr1*)BAkik/J (NG2CreER^{TM}) lines was used in all experiments. Breeding pairs were obtained from The Jackson Laboratory (stocks: 007676 and 008538, respectively).

All animals were bred in house under 12/12 hour light/dark conditions with water and food available *ad libitum*.

3.3 Slice preparation for electrophysiology

For patch-clamp recordings, we used coronal brain slices containing central part of corpus callosum, prepared from P7-10 (N mice), P19-22 (N mice) or P50-53 (N mice) day old mice of both sexes, a total of N mice for all experiments. Mice were anesthetized with a mixture of isoflurane in pure O2 (3% v/v) and decapitated. The brains were dissected in the ice-cold N-methyl-D-glucamine (NMDG)-based solution containing (in mM): 135 NMDG, 1 KCl, 1.2 KH_2PO_4, 20 choline bicarbonate, 10 glucose, 1.5 $MgCl_2$, and 0.5 $CaCl_2$ (pH 7.4, 310 mOsm), gassed with carbogen (95% O_2, 5% CO_2) for at least 30 min prior to the preparation. 300-µm-thick (for P8-11 animals), 270-µm-thick (for P19-22 animals) or 250-µm-thick (for P50-53 animals) coronal brain slices were cut in the same solution using Leica VT1200S vibratome. The slices were transferred to a preheated to 32°C Haas-type interface incubation chamber and perfused with Ringer solution containing (in mM): 124 NaCl, 3 KCl, 1.25 NaH_2PO_4*H_2O, 2 $MgCl_2$, 2 $CaCl_2$, 26 $NaHCO_3$, 10 glucose; 300 mOsm/kg; 7.4 pH; gassed with

carbogen. Afterwards, the slices were left to recover for ~1 hour while the chamber was gradually cooling down to room temperature.

3.4 Patch-clamp recordings

Following the recovery period, individual slices were moved to a submerged recording chamber, mounted on an upright microscope stage (FN-1, Nikon, Japan). The microscope was equipped with infrared differential interference contrast (IR-DIC) filters and a fluorescence light source. Throughout the experiment, the recordings were conducted at room temperature (20-22°C) and the slices were consistently perfused with fresh Ringer solution carbogenated at a flow rate of about 2 ml/min. OPCs were chosen for recordings based on their bright red fluorescence (as NG2 is downregulated in oligodendrocytes resulting in weak tdTomato fluorescence) and could be differentiated from pericytes by their morphology.

Patch pipettes were made by pulling borosilicate glass capillaries (Science Products, Germany) using a vertical puller (Model PC10, Narishige, Japan). The pipettes had a resistance of 5-7 MΩ when filled with an internal solution containing (in mM): 125 K-gluconate, 2 Na_2ATP, 2 $MgCl_2$, 0.5 EGTA, 10 HEPES, 20 KCl, 3 NaCl; 280-290 mOsm/kg, titrated to pH 7.3 with KOH. During all recordings, the cells were voltage clamped at the holding potential V_h = −80 mV using an EPC-8 amplifier (HEKA, Germany). The software JPCalc for Windows (Peter H. Barry, Sydney, Australia) was used to calculate the liquid junction potential, and V_h was corrected by −13 mV before forming a seal. Series resistance was not compensated. To confirm that the selected cell was an OPC after establishing the whole-cell configuration, 10 depolarizing voltage steps were applied in +10 mV increments from V_h = −80 mV. All recordings of currents evoked in response to voltage steps were low-pass filtered at 10 kHz and digitized at a sampling frequency of 20 kHz (ITC-18, HEKA Instruments Inc, USA). Data acquisition was performed using Recording Artist software written by Dr. Rick Gerkin (Arizona State University, USA) in Igor Pro 6.3 (WaveMetrics, Lake Oswego, USA). NMDA-receptor antagonist (RS)-3-(2-Carboxypiperazin-4-yl)-propyl-1-phosphonic acid (CPP, 10 µM, Tocris) and GABA A-receptor antagonist SR95531 2-(3-Carboxypropyl)-3-amino-6-(4 methoxyphenyl)pyridazinium bromide (Gabazine, 5 µM, Sigma) were present during all recordings. Cells without a clear OPC current profile were excluded (Kukley et al., 2007; Nagy et al., 2017).

Isolated pulse stimulator (A-M Systems, Model 2100, Science Products, Germany) was used to elicit evoked synaptic currents with a pipette identical to the patching pipettes filled with Ringer solution and placed at 100 ± 25 µm from the recorded cell. Single or paired biphasic rectangular pulses (200-300 µs duration) were applied every 15 seconds, and trains of stimuli were applied every 20 seconds. Minimal stimulation was conducted as described in our previous study (Kukley et al.,

2007; Nagy et al., 2017) in brain slices where the corpus callosum was isolated from the cortex by 4 cuts: 2 parallel and 2 perpendicular to the orientation of callosal axons.

We applied a square test voltage step of −10 or −5 mV to monitor changes in the series resistance (R_s) during recordings of stimulated and spontaneous synaptic currents. The test step was applied 1-2 s before the stimulation to avoid influencing the evoked currents. All synaptic currents were low-pass filtered at 1 kHz and digitized with a sampling frequency of 10 kHz. To ensure that ionotropic glutamate receptors were responsible for synaptic currents, we utilized CNQX, a blocker of all ionotropic glutamate receptors. All drugs were dissolved in Ringer solution and applied via the bath.

The recordings were performed at room temperature. Evoked synaptic currents were elicited with isolated pulse stimulator (A-M Systems, Model 2100, Science Products, Germany) using a pipette identical to the patching pipettes filled with Ringer solution and placed at 100 ± 25 μm from the recorded cell. Single or paired (40 ms inter-pulse interval) biphasic rectangular pulses of 200–300 μs duration were applied every 15 s. Trains of stimuli were applied each 20 s. Minimal stimulation was performed as described in our previous work (Kukley et al., 2007; Nagy et al., 2017) in brain slices where the corpus callosum was isolated from the cortex by 4 cuts: 2 parallel and 2 perpendicular to the orientation of callosal axons.

The recordings included in this work had to meet three criteria or they would be discarded: 1) The offset drift at the end of the experiment could not exceed ± 5 mV. 2) R_s could not exceed 40 MΩ (all recorded cells had R_s between 20 and 40 MΩ). 3) The change in R_s could not exceed ± 30% compared with the beginning of the experiment.

3.5 I-V curve recordings

We used a Cs-based internal solution containing (in mM): 100 $CsCH_3SO_3H$ (CsMeS), 20 tetraethylammonium (TEA) chloride, 20 HEPES, 10 EGTA, 2 Na_2ATP, and 0.2 NaGTP; 280-290 mOsm/kg; titrated to pH 7.3 with CsOH, and a Ringer solution with elevated Ca containing (in mM): 119 NaCl, 2.5 KCl, 1 NaH_2PO4*H_2O, 1.3 $MgCl_2$, 2.5 $CaCl_2$, 26.2 $NaHCO_3$, 11 glucose; 300 mOsm/kg; 7.4 pH; gassed with carbogen. Spermine, a potent voltage-dependent blocker of Ca^{2+}-permeable AMPARs (Sigma, 100 μM) was included into the internal solution in all recordings of evoked EPSCs in order to test the Ca^{2+}-permeability of AMPA receptors in OPCs. V_h was corrected for a −7 mV liquid junction potential before seal formation. The cells were held at different potentials (−90, −40, 0, +20, and +40 mV) and 10-50 sweeps were recorded at each potential.

To monitor changes in the series resistance (R_s) during recordings of stimulated and spontaneous synaptic currents we applied a 200-300 μs square test voltage step of −10 or −5 mV at the beginning of each sweep. The test step was applied 1-2 s in advance of the stimulation to avoid influencing the

evoked currents. All synaptic currents were low-pass filtered at 1 kHz and digitized with a sampling frequency of 10 kHz. To verify that synaptic currents were mediated by ionotropic glutamate receptors, we used 6-Cyano-7-nitroquinoxaline-2,3-dione (CNQX, 10 μM, Abcam), a blocker of all ionotropic glutamate receptors. All drugs were dissolved in Ringer solution and applied via the bath. All recordings were performed at room temperature (20-22°C).

3.6 Calculations for intrinsic properties of OPCs

The intrinsic properties of OPCs were calculated as follows. To obtain the membrane resistance (R_m), we subtracted the series resistance (R_s) obtained from the peak of the capacitive transient from the input resistance (R_{in}) obtained from the steady-state current in response to a small voltage step: $R_m = R_{in}-R_s$. To estimate the cell capacitance (C_m), we calculated the capacitive current (IC) by subtracting the resistive current from the total current ($\Delta I(t)$) during a voltage step (ΔV) and then integrated the area under the IC curve. The resulting value of ΔQ was converted to C_m, with the resting membrane potential (RMP, V_r) set to zero current potential. To quantify the leak current density (LC), we measured the current response to a +10 mV voltage step (Δ+10 mV) from a holding potential of −80 mV to −70 mV. The values for voltage-activated Na^+ current (Na_v), voltage-activated fast A-type K^+ current (K_v A-type), and voltage-activated slow K^+ current (Kv steady-state) were obtained from the leak-subtracted current traces, and current densities were calculated by dividing the peak values of the currents by the cell capacitance (C_m) (Kukley et al., 2007).

3.7 Analysis of qEPSCs

In order to examine the quantal amplitude of synaptic currents in OPCs, we conducted an analysis of delayed EPSCs that occur after the train stimulation of callosal axons with 20 pulses at either 25 or 100 Hz. We defined delayed EPSCs as those that have an onset of more than 10 ms following the last stimulus of the train. We collected the delayed EPSCs in 20-160 sweeps, each of which was 1.73-2.3 seconds in length, for each recorded cell. To detect the EPSCs, we utilized a deconvolution-based algorithm called FBrain (Pernía-Andrade et al., 2012; Nagy et al., 2017), which is a customized program that runs under IgorPro 6 (WaveMetrics, Lake Oswego, USA) and was kindly provided by Peter Jonas Lab (IST, Klosterneuburg, Austria). Before analysis, we applied additional digital high-pass (10 Hz) and Notch (50 ± 0.5 Hz) filtering to the recorded sweeps in FBrain. The convolved trace was then passed through a digital band-pass filter at 0.001 to 200 Hz. We constructed the Pass 1 synthetic event detection template with a rise-time constant, τ of 0.5 ms, a decay time constant, τ of 4 ms, and an amplitude of −3 pA. The event detection threshold (θ) was set to 4.2 times the standard deviation of a Gaussian function fitted to the all-point histogram of the convolved trace, with

Freedman-Diaconis binning (Pernía-Andrade et al., 2012; Nagy et al., 2017). All detected events were visually inspected and those that did not exhibit the kinetics of typical excitatory postsynaptic currents were manually removed. We rejected all cells with a removal ratio of more than 30% from further analysis. The subsequent analysis was conducted using custom-written macros in IgorPro.

3.8 Non-stationary fluctuation analysis (NSFA)

To estimate the single channel conductance of synaptic AMPARs in OPCs, we utilized peak-scaled non-stationary fluctuation analysis (NSFA) (Hartveit and Veruki, 2007). We visually inspected the delayed EPSCs in each cell and only selected events with smooth rise- or decay phase for NSFA. To ensure the accuracy of our results, we applied Spearman's rank-order correlation test to check for any drift in peak amplitude, rise-time, or decay-time of the events during each experiment. We also confirmed that there was no correlation between rise-time and decay-time constant. If any correlation was found, we excluded the cell from the NSFA. We randomly selected 13 events from 8 cells in the P10 group and 26 events from 4 cells each in the P20 and P50 groups, respectively. We pooled these events within each age group, resulting in 104 events included in the NSFA for each experimental group. The events were aligned on the point of steepest rise, and the mean waveform was calculated from the aligned events. Next, the amplitude of the mean waveform was scaled to the amplitude of each individual event, and the scaled mean waveform was subtracted from each individual event to obtain the noise component. We then calculated the variance for each event by using the background variance estimated from the segment of the trace before the onset of each event. We calculated the ensemble background-subtracted variance as an average of variances of all events. The mean amplitude wave was binned into 8-10 bins, and the corresponding values of the variance wave were then obtained. We plotted the variance-mean relationship and fitted it with a parabola function to calculate the single-channel conductance (γ) of synaptic AMPAR:

$$\delta^2(I) = iI - I^2/N + \delta$$

where $\delta^2(I)$ is the variance; i is the (weighted) estimate of a mean single channel current; N is average number of channels opened at the peak, and δ_{bgr}^2 is the background variance. The single-channel conductance (γ) of synaptic AMPAR was calculated from the single-channel current i as:

$$\gamma = i/(V_m - E_{rev})$$

where $(V_m - E_{rev})$ is the driving force for AMPAR-mediated EPSC, with Vm= −80 mV (holding potential) in our study and E_{rev} = 0mV (AMPAR reversal potential) due to our internal and external solutions.

Notably, because we used the peak-scaling method for NSFA, the information on the total number of available channels is lost. Therefore, the parameter N has no meaning and is not further analyzed in our study. All routines for NSFA were custom programmed and were based on the code presented in the supplementary material of Hartveit and Veruki, 2007. Different numbers of bins were also tested, but varying the number of bins did not affect the results. Finally, the values of variance were plotted versus the corresponding values of the mean current amplitude.

All routines for NSFA were custom programmed and were based on the code presented in the supplementary material of Hartveit and Veruki, 2007.

3.9 Analysis of evoked EPSCs and I-V curve

We used custom-written IgorPro macros for the analysis of evoked EPSCs. In order to remove stimulus artifacts, the averaged sweeps that contained failures after the initial stimulus or those recorded in the presence of tetrodotoxin citrate (TTX, 1µm, Abcam) or CNQX, or recorded at holding potential of Vh = 0, were first averaged, and then the segment of the averaged sweep from time-point of the stimulation to the last point before the second stimulus was removed. This removed segment was then duplicated and concatenated with itself, resulting in a sweep containing only the averaged stimulus artifact, which was subtracted from each recorded sweep.

To measure the EPSC amplitude, the baseline of each recorded sweep was adjusted to the 500 ms segment immediately preceding the stimulation. The peak-center of each event was determined as the time-point at which the first derivative of the sweep crossed zero. The amplitude values of the current at the peak ± 2 points around it were then averaged, and the resulting value was taken as the EPSC amplitude. The threshold for event detection was determined for each recorded sweep individually, and was equivalent to three times the standard deviation of the noise. In case several EPSCs occurred after a given stimulus, the amplitude of the first event was measured.

Although paired-pulse stimulation was used in all experiments, only the EPSCs occurring after the first pulse were considered in order to generate the I-V curve. The amplitudes of all recorded sweeps at a given holding potential (−90, −40, 0, +20, +40 mV, and back to −90 mV) were measured and averaged to generate the I-V curve in each cell. To calculate the rectification index, the average value of the EPSC amplitude at +40 mV was divided by the average value of the EPSC amplitude at −90 mV. To determine the paired-pulse ratio, the average amplitude value of the EPSC occurring after the second pulse was divided by the average amplitude value of the EPSC occurring after the first pulse at a holding potential of −90 mV.

3.10 Estimation of the fraction of rectifying AMPARs (FRR) based on rectification measurements

To obtain the FFR, we used the equation developed by Stubblefield and Benke, , which allows for estimation of the FRR based on rectification measurements. Their rectification indexes were calculated as a ratio of EPSC amplitudes recorded at −70 mV and at +40 mV. To match their approach, we took the inverse of our RI values (1/RI) and adjusted their equation to model our results as follows:

$$FFR = (1 - 1/RI * F3)/1/RI * (F1 - F3),$$

where F1 is the maximal block of inwardly rectifying receptors (EPSC at +40 mV/ EPSC at −90mV), extrapolated to be 0.035 (Stubblefield and Benke, 2010). F3 is the value for linear relationship (F3 = 40/90 = 0.444). This analysis assumes that there is no change in presynaptic function.

3.11 Analysis of the events during the train

For the analysis of events during trains we started by subtracting the stimulus artifacts in the same manner as in *Analysis of evoked EPSCs and I-V curve*, with the following exception: cut piece of the train containing failures was concatenated n times, in which n = number of stimuli in the original train and thus generated "train of failures" was subtracted from each recorded sweep.

We detected events in the stimulus-artifact–subtracted sweeps containing a 1-s-long pretrain baseline using a deconvolution-based algorithm in FBrain. We identified phasic events during the train as those events for which onset was located within 6 ms after the stimulus onset. Events for which onset occurred later than 6 ms within the same interstimulus interval were defined as asynchronous events during the train and were analyzed for charge transfer.

To estimate the amplitude of each phasic event, we adjusted the baseline to the time interval from the beginning of each stimulus until the event onset. We determined the peak center of each event as a minimum within the interval of 7.5 ms after the stimulus onset, and we averaged the values of the current in the peak center and in 2 points around it to obtain the measurement of the current amplitude. In our study, a response was defined as an EPSC for which onset is located <6 ms after the stimulus and whose peak is located <7.5 ms after the stimulus.

To estimate the amplitude of each failure, we used a similar procedure, except that the peak center was determined as one point randomly selected by the algorithm within the interval of 7.5 ms after the stimulus onset. In our study, a failure was defined as a situation in which, after a stimulation pulse, we did not observe an EPSC with an onset located <6 ms after the stimulus and with peak located <7.5 ms after the stimulus.

For each stimulation paradigm in each cell, we calculated the amplitude of phasic currents after a given stimulus as the mean amplitude of all responses and all failures after this stimulus. Response probability was calculated as the number of responses after a stimulus divided by the total number of trials in the stimulation paradigm. We then averaged the corresponding mean values across all cells for a given stimulation paradigm to calculate the average amplitude and response probability after a given stimulus. To study the kinetics of phasic events, we measured the 10%–90% rise time and weighted decay time constant for each event. The latency of each phasic response was determined as the time difference between the response onset and the time point of the stimulus.

We split each inter-stimulus interval into 5-ms-long bins and performed trapezoidal integration on each bin to calculate the total charge transfer during the train. To calculate the normalized average amplitude and response probability, we divided the corresponding average value after a given stimulus by the average value after the first stimulus.

3.12 Tamoxifen injections

Cre activity in postnatal ROSAmT/mG:NG2-CreER^{TM} double-transgenic mice was induced by intraperitoneal injection of 4-hydroxytamoxifen (4-OHT, Sigma). A 10 mg/ml stock solution was prepared by dissolving 4-OHT in 19:1 autoclaved vegetable oil:ethanol. Mice were injected with 1 mg of 4-OHT per gram of body weight intraperitoneally at the age of P5-8, P16-19 and P47-50. Control animals were injected with the same volume of vehicle. P16-19 and P47-50 animals were anesthetized with a low dose of Isoflurane for the procedure.

3.13 Preparation of brain slices for immunohistochemistry

3 days after 4-OHT injection mice were anesthetized with a mixture of Isoflurane (3% v/v) in 100% oxygen and decapitated. Whole brains were removed and 300µm coronal brain sections were prepared in ice-cold carbogenated (95% O_2, 5% CO_2) N-methyl-D-glucamine (NMDG) solution containing (in mM): 135 NMDG, 1 KCl, 1.2 KH_2PO_4, 20 choline bicarbonate, 10 glucose,1.5 $MgCl_2$ and 0.5 $CaCl_2$ (pH 7.4, 310 mOsm) using Leica VT 1000S vibratome. Subsequently, the slices were transferred into 4% paraformaldehyde (PFA) in 0.01M phosphate buffered saline (PBS) and fixed for 20-24 hours at 4°C. Afterwards slices were washed in PBS, embedded into 5% agar in PBS and re-sectioned to 70µm slices at Thermo Fisher Scientific HM 650V microtome. In the initial staining trial we did not find GFP+ cells longer than 60µm along the posterior-anterior axis therefore 70µm slices were sufficient to find full cells with uncut processes. Slices were washed with 0.1M Tris-buffered saline (TBS, pH 7.6) three times. Afterwards blocking solution containing 0.1M TBS, 10% fraction V albumin (Roth) and 1% Triton-X (Roth) was applied for 1 hour at 37°C. Afterwards slices were

incubated for 48 hours with primary antibodies (1:500 concentration) in 0.1M TBS, 10% albumin V and 0.5% Triton-X at 4°C. Primary antibodies: Guinea pig and rabbit anti-mice NG2 antibodies were gifts from Dr William Stallcup (Burnham Institute, La Jolla, CA, USA). Rabbit anti-GFP antibody was obtained from Invitrogen, chicken anti-GFP antibody was obtained from Abcam. After a short wash in TBS slices were incubated with secondary antibodies (1:1000) in TBS, 10% albumin and 0.5% Triton-X for 48 hours at 4°C. Secondary antibodies: anti-chicken Alexa Fluor 488 (AF488), anti-rabbit AF488, anti-rabbit AF633 and anti-guinea pig AF633 antibodies were obtained from Invitrogen, anti-rabbit Rhodamine Red-X (RRX) and anti-chicken fluorescein isothiocyanate (FITC) were obtained from Dianova. Cell nuclei were counter-stained by 20min incubation with 0.2µg 4'6-diamidino-2-phenylindole (DAPI) in TBS. After washing with TBS slices were left to air-dry for 10min, mounted in Vectashield Antifade Mounting Medium (Vector Labs.) and sealed with nail-polish. Preparations were stored in the dark at 4°C until confocal microscope imaging.

3.14 Image acquisition

Immunostained sections were imaged at Zeiss LSM 710 Meta Confocal microscope equipped with 63x Plan Apochromat NA 1.4 oil immersive objective. Pinhole was set to 50 µm (approx. 1 Airy unit for 488nm wavelength). Whole cells were scanned under 1.1 – 1.5 zoom, pixel dwell ranging between 9.7 – 12.5µs and 0.089 x,y pixel size. The z-step between images within a stack was set to 0.37µm, resulting in a 50% overlap between optical sections (74 µm/section). Frame size was adjusted to keep identical pixel size at every zoom level. All images were acquired with 16bit color depth and 4x averaging. The following laser excitation lines and emission detection ranges were used: Alexa 488/FITC – 488nm excitation, 494 – 553nm emission; Alexa 568/RRX – 561nm excitation, 562 – 631nm emission; Alexa 633 – 633nm excitation, 641 – 729 emission; DAPI – 410nm excitation, 416 – 474 emission. Laser power of 1.5 – 3.0% was used for 488nm, 561nm and 633nm lasers. 0.3-0.5% power was used for the 405nm lasers. Laser power, gain and offset were adjusted for the best possible signal to background ratio. All acquired stacks of images were saved in Zeiss .lsm file format. The format preserves meta-data information.

3.15 Cell tracing

Previously acquired confocal image stacks in .lsm format were uploaded into Neurolucida. The voxel sizes were loaded automatically from the .lsm files by the software. Single pixel-thick cell reconstructions were created by tracing manually through the middle of the processes. Brightness/contrast and gamma were adjusted during tracing to keep similar intensity profiles at all

traced slices/sections. Every tubular or conical protrusion originating from the soma was classified as a process, regardless of length or branching.

3.16 Branch order and the positioning of process elements

In this work a branch is defined as a part of a process contained between: 1) the origin point (root) and a branching point (node); 2) between 2 br. points; 3) between a br. point and a process ending. Centrifugal ordering, which assigns numbers in an ascending order, starting from process origin, was used to mark the position of new branches along the process. In brief: A branch starting at the origin of a process (root) is assigned order 1. If the branch terminates with a br. point the br. point is also assigned order 1. All new branches starting at a the br. point are assigned order +1. Endings are ordered in the same way and receive br. order of the branch they terminate. This numeration continues until all branches, br. points and endings have an order assigned. As an example: if a branch originates from a br. point of order 3 then the branch is of order 4 and it's ending is also of order 4.

3.17 Sholl analysis

Sholl analysis was performed in Neurolucida Explorer. In brief: a set of concentric shells spaced by 2.5μm and anchored at the centroid of the soma was placed over the cell. The shells partition the brain parenchyma into volume compartments separated by the shells. The intersections of the shells with processes serve as an indication of the changes in structural over increasing distance from the soma. In addition, the number of br. points, endings, branches and the lengths of those branches, contained within individual compartments, can be quantified and an analyzed as a function of increasing distance. Please note that the plots on the relevant figures only indicate the upper radius of the shell range.

3.18 Branch direction in space and alignment with anatomical body axes

To calculate the change in direction of branches the Cartesian coordinate system used by Neurolucida was converted into a spherical coordinate system. In the spherical coordinate system position of a point is described by three values: Radial distance r, which is the distance towards beginning of the coordinate system; polar angle φ defined for x,y axes and azimuth angle θ corresponding to the z axis. For coronal slices used in this work the x,y axes are aligned with the lateral-medial (L-MA), dorsal-ventral (D-VA) anatomical axes, respectively, and the z axis aligns with the anterior-posterior axis (A-PA). φ takes values between 0° and 360°, therefore for the purpose of measuring the alignment of branches with L-MA and D-VA φ quadrants were converted to 0°-90°

where all angles approaching 0° align with L-MA while angles at 90° align with D-VA. Similarly, θ takes values from -90° to +90°, which were converted to 0°-90°, where angles at 90° align with A-PA while angles at 0° completely miss-align with A-PA. Due to the tortuosity of branches all angular measurements were performed on vectors spanning over the origin of the branch (root, br. point) and it's terminus (another br. point or ending). The lengths reported are the real lengths of the branches, not vector lengths. For graphing and statistical analyses all measurements were grouped into 15° bins, 6 in total. The radial distance was ignored and φ and θ angles were analyzed separately.

3.19 Change in branch direction after a branching point

To measure the change in direction all branches were approximated as vectors spanning over their origins and terminations. For each pair of a mother branch (terminating at a br. point) and it's daughter (originating from the br. point) the planar angle was measured as an angle between the daughter vector and a linear extension of the mother vector. In the measurement the mother and daughter vectors are assumed to share a unique 2D plane. If the daughter branch does not change direction the angle is 0° and a maximum possible angle is 180° (the daughter is parallel to it's mother, facing backwards).

3.20 Statistics

All data acquisition was randomized (cells during patch-clamp experiments, traced cells, slices selected for stainings). Throughout the study we made all efforts to avoid pseudoreplication by restricting the maximum number of cells acquired from single animal to three. The exact number of cells and animals used in each experiment is given in the figure legends.

Statistical analysis was performed in Graph Pad Prism 9.3.1. All datasets were tested for homoscedasticity and normality. If the datasets had both normal distributions and equal variances, one-way ANOVA with post hoc Holm-Šídák's test was used. If the datasets had normal distributions but unequal variances, Brown-Forsythe and Welch ANOVA with post hoc Dunnet's T3 test were used. If the datasets were not normally distributed, but had equal variances, Kruskal-Wallis test with post hoc Dunn's test were used. If the datasets were not normally distributed and had unequal variances, Brown-Forsythe and Welch ANOVA with post hoc Dunnet's T3 test were used. For all statistical comparisons, significance level was set at $p < 0.05$. Statistically significant differences are indicated on the figures by markings: $*$ represents $p \leq 0.05$, $**$ represents $p \leq 0.01$, and $***$ represents $p \leq 0.001$. The exact p values are given in the text. If the data is normally distributed the data in the text or figures is reported as scatter plots and mean ± standard error of the mean (SEM) or, if not normally distributed as a boxplot containing median and 10th, 25th, 75th, 90th or 25th, 75th percentiles.

The datasets were checked for outliers by Prism's ROUT method at Q=5%.

3.21 Power and sample size calculations

The sample sizes for all of the statistical comparisons in this work were determined based on the means and pooled standard deviations from preliminary recordings of 8-10 cells or slices per group, α = 0.05, β = 0.8, corrected for the number of pairwise comparisons (k), based on the following equations:

$$n = 2(\sigma\frac{z_{1-\alpha/(2\tau)} + z_{1-\beta}}{\mu A - \mu B})^2,$$

$$1 - \beta = \phi(z - z_{1-\alpha/(2\tau)}) + \phi(- z - z_{1-\alpha/(2\tau)}),$$

$$z = \frac{\mu A - \mu B}{\sigma\sqrt{\frac{2}{n}}},$$

Where n is the sample size; σ is standard deviation; is standard Normal distribution function; α is Type I error; is the number of pairwise comparisons; β is Type II error. During the calculations, the normality of residuals and equality of variances were assumed *a priori*.

The calculations were performed in an online calculator available at:

http://powerandsamplesize.com/Calculators/Compare-k-Means/1-Way-ANOVA-Pairwise

4. Results

4.1 Neither quantal size (q) nor other properties of qEPSCs at neuron-OPC synapses change during callosal development

The classical discovery at the neuromuscular junction by Del Castillo and Katz, 1954 has lead to a formulation of a theory, currently known as the quantal hypothesis, that the communication between the pre and postsynaptic sites rely on an all-or-none neurotransmitter release in the form of quantized packets with each packet resembling a bit of information. Therefore the strength of postsynaptic response (I) is mainly dependent on three properties: the probability of release of a vesicle loaded with neurotransmitter at the presynapse (p), triggering a response proportional to the number of receptors open at the postsynapse (quantal amplitude, q), released in response to a single action potential (AP) arriving at N release sites within the synapse. (I = pqN). Up to this day this model provides a basis for measurements of changes to synaptic strength. At the neuromuscular junction and under physiological conditions the p and N at a single synapse are high enough to ensure that almost every presynaptic impulse leads to contraction of a muscle fiber. In the CNS however, p values are usually low and most synapses have only a single release site, requiring activation of multiple synapses within a short timeframe to summarily overcome passive filtering properties of the membrane. This however is offset by the number of synapses innervating a single cell, which for an average pyramidal neuron number in tens of thousands, reaching 20-30 thousands for the large neurons of CA1 and CA3 hippocampal formations. In such a setting an individual synapse and its properties are far less influential than at the neuro-muscular junction and a collective activation and information integration throughout hundreds of connections becomes biologically relevant. Within this framework neuron-OPC synapses are one of the least understood in the CNS.

To test whether the quantal size or any other properties of quantal EPSCs (qEPSC) at the neuron-OPC synapses change during callosal development we investigated the delayed EPSCs triggered by prolonged train stimulation which arise due to elevated residual Ca^{2+} at the presynapse after the cessation of the stimulation. As we proved in our previous publication, such delayed EPSCs have quantal properties at OPC synapses.

We found no significant differences between the age groups in any of the investigated parameters: mean amplitudes [**Fig. 16C**; -3.79 +/- 0.15pA at P10; -3.93 +/- 0.11pA at P20, -4.27 +/- 0.19 pA at P50; ANOVA p=0.105], rise times [**Fig. 16D**; 0.516 +/- 0.011ms at P10, 0.539 +/- 0.0157ms at P20, 0.516 +/- 0.0168ms at P50; p=0.722], decay tau [**Fig. 16E**; 1.296 +/- 0.0734 at P10, 1.493 +/- 0.0717 at P20, 1.283 +/- 0.0756 at P50; p=0.085] and total charge transferred [**Fig. 16F**; 7.526 +/- 0.374 fC at P10, 8.651 +/- 0.3681 fC at P20, 8.469 +/- 0.412 fC at P50; p=0.0799].

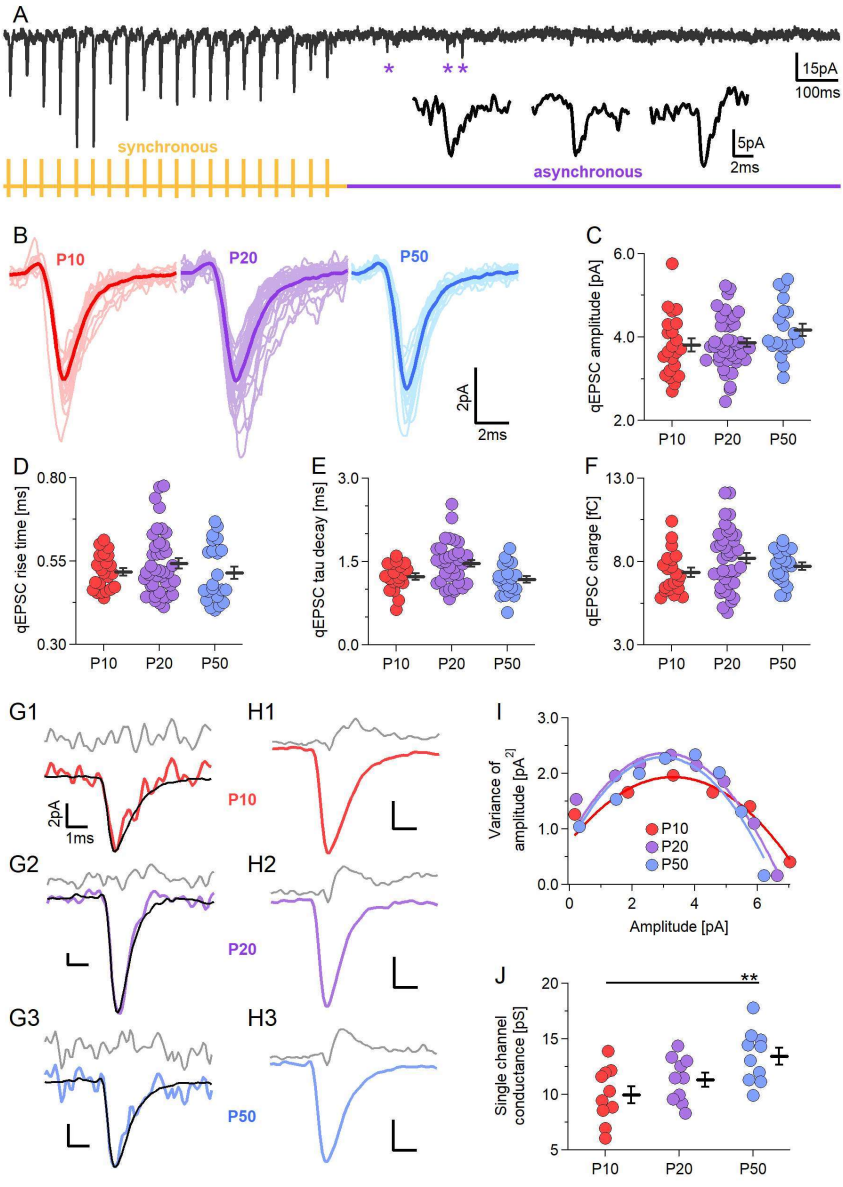
A
15pA
100ms
synchronous
asynchronous
5pA
2ms
B
P10
P20
P50
2pA
2ms
C
qEPSC amplitude [pA]
6.0
4.0
2.0
P10
P20
P50
D
qEPSC rise time [ms]
0.80
0.55
0.30
E
qEPSC tau decay [ms]
3.0
1.5
0.0
F
qEPSC charge [fC]
13.0
8.0
3.0
G1
G2
G3
H1
H2
H3
2pA
1ms
I
Variance of amplitude [pA2]
Amplitude [pA]
J
Single channel conductance [pS]
**

Figure 16. During callosal development amplitude, charge and kinetics of quantal EPSCs do not change but conductance of OPC AMPARs gradually increases.

(A): Representative trace recorded from a P20 callosal OPC (Vh=-80). Stimulation artifacts were blanked in the example for clarity. Below, in orange, a schematic representation of the stimulation paradigm applied to callosal axons: 20 pulses at 25 Hz train stimulation, in violet, the cessation of stimulation and highlights part of the trace containing delayed EPSC used in the analysis. Delayed events are marked by *. The magnified waveforms of the events are shown above the stimulation trace. They all have properties of quantal events (qEPSCs). (B): Averages of delayed events from 22 cells from the P10 group (light red), averages of delayed events from 39 cells from the P20 group (light purple), averages of delayed events from 22 cells from the P50 group and group means (P10, red; P20, purple; P50, blue). (C): Comparison of amplitudes of the averaged delayed events. Each circle represents one cell. Black bars represent group average ± SEM. P10 group: n=22 in N=21 animals; P20 group: n=39 in N=35 animals; P50 group: n=22 in N=19 animals. The same labeling and n numbers apply to graphs (D) to (F). There are no significant differences between groups. (D): Similar to (C) for 20-80% rise time of the averaged delayed events. There are no significant differences between groups. (E): Similar to (C), for tau decay of the averaged delayed events. There are no significant differences between groups. (F): Similar (C), for charge of the averaged delayed events. There are no significant differences between groups. (G): Single representative spontaneous qEPSC events; G1: P10 (red); G2: P20 (purple) and G3: P50 (blue), overlaid with the re-scaled qEPSCs average waveform (black) recorded from the same cells. Grey trace represents the residual noise for the corresponding event (black trace subtracted from the coloured trace). (H): Average EPSCs waveforms (black) from a representative random event selection from P10 (H1), P20 (H2) and P50 (H3). The gray traces represent the mean residual noise variance from across all mEPSCS for the corresponding random event selection. (I) Amplitude – variance of amplitude graphs and their parabola fits from the same random event selection as shown in H, J, L. J: Single channel conductance measurements of 10 repetition of random event selection. Coloured dots: single cell measurements, black diamonds: mean ± SEM. Black horizontal bars link significantly different groups. * = $p<0.05$; ** = $p<0.01$; *** = $p<0.001$.

A surprising result, given that the available literature shows a substitution of Ca^{2+}-impermeable GluA2 enriched AMPARs to GluA2-lacking and highly conductive AMPARs, between juvenility and adulthood. Therefore to test whether our results are consistent with the literature and this substitution indeed happened we performed Non Stationary Fluctuation Analysis (NSFA) on the qEPSCs.

We found that the AMPAR single channel conductance changed significantly during callosal development, from 9.96 +/- 0.78 pS in P10 OPCs, increased to 11.33 +/- 0.64 pS in P20 (not significant; p=0.195), and further increased to 13.42 +/- 0.75 pS in P50 OPCs [**Fig. 16I-J**; p=0.00676], strongly suggesting replacement with Ca-permeable subunits at the synapses did take place during callosal development. P20 and P50 groups did not differ significantly (p=0.099).

4.2 Substitution of AMPARs by Ca^{2+} permeable subunits at OPC synapses is almost complete in the 3rd postnatal week of callosal development

AMPARs containing the edited GluA2 subunit are impermeable to Ca^{2+} and as such show linear current-voltage (I-V) EPSCs when recorded in the intracellular presence of spermine, an internal

polyamine blocking Ca^{2+}-permeable AMPARs at positive membrane potentials. Therefore to corroborate our findings of single-channel conductance increases we recorded the I-V relationship of AMPAR-mediated EPSCs [**Fig. 17**]. We found that juvenile, P10 I-V curves show close to linear rectification (rectification index, RI) of = 0.364 +/- 0.0204, which very significantly decreases by P20 (RI = 0.157 +/- 0.0296), and decreased further by P50 (RI = 0.138 +/- 0.0302) [**Fig 17A, B**; P10 vs P20, p=0.0000318; P10 vs P50, p=0.0000242]. P20 and P50 groups did not test as different (p=0.627). However, rectification can be used to estimate the proportion of Ca^{2+}-permeable receptors. To do that we adopted a model described by Stubblefield and Benke, 2010, utilized in our previous publication (Chen et al., 2018) [**Fig 17C, D**]. Based on the model, only 19.59 +/- 4.99% of the receptors were Ca^{2+} permeable in the P10 group, whereas this percentage increased to 68.26 +/- 6.24 % by P20 and further to 73.66 +/- 6.79 % at P50 [**Fig 17C, D**; P10 vs P20, p=0.0000124; P10 vs P50, p=0.00000689], strongly suggesting that the majority of the Ca^{2+}-permeable subunits are already incorporated into synaptic AMPARs by the age of P20.

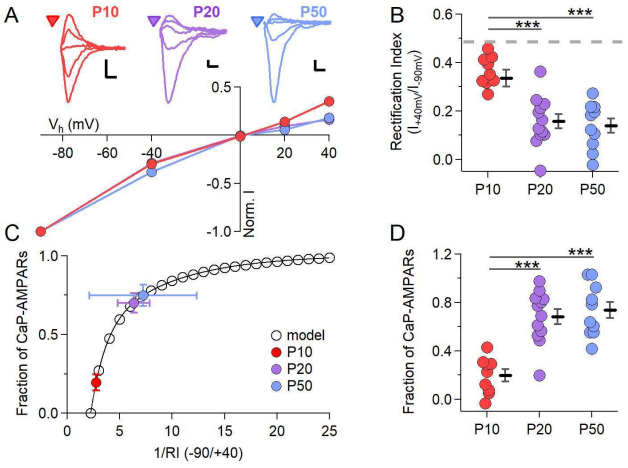

Figure 17. AMPARs become significantly more Ca2+ -permeable during callosal development.

(A): I-V relationship of the amplitudes of evoked EPSCs recorded in OPCs in all age groups. Each circle represents the mean amplitude ± SEM in the age group, recorded at Vh = -90, -40, 0, +20 or +40mV, normalized to the average amplitude recorded at Vh = -90mV. Examples of the average currents recorded at each of the holding potentials in a single cell are above the means. P10: n=9 OPCs, N=6 animals; P20 n=12, N=9; P50: n=10, N=9. (B): Summary scatter-plot showing the rectification index (RI) of evoked EPSCs recorded at Vh = +40, normalized to currents at Vh = -90, in cells from (A). Each circle represents the RI of one cell. Black diamonds represent group mean ± SEM. Grey dashed line represents the theoretical perfect, non-rectifying I-V relationship (RI = 0.44). Black horizontal bars link significantly different groups. * = p<0.05; ** = p<0.01; *** = p<0.001, n and N are identical to (A). (C): Model of the relationship between inverted rectification index (1/RI) and fraction of rectifying, Ca2+-permeable AMPARs (CP-AMPARs). Colored circles represent average 1/RI for each experimental group plotted against the mean calculated CP-AMPAR fraction ± SEM. (D): Summary of the fraction of CP-AMPARs in all age groups, based on (C). Each circle represents the CP-AMPAR

fraction in one cell. Black diamonds represent group mean ± SEM. Black horizontal bars link significantly different groups. * = p<0.05; ** = p<0.01; *** = p<0.001, n and N are identical to (A).

Taken together with the single channel conductance, these results show that OPCs continue to change their GluA subunit expression throughout development. Despite similar mEPSC kinetics across different age groups, there are fundamental differences in the properties of the AMPARs, which should lead to an overall increase in receptor conductance, higher than the one we highlighted in **Fig. 16 G1-J.** Changes in membrane resistance and various K^+ conductances are the most likely causes, as they are well documented to occur during dendrite growth and maturation (Spruston et al., 2013). Therefore, in the next step we investigated changes in the current responses to voltage commands (current profile) and other membrane properties during OPC development.

4.3 Changes in the passive properties and current pattern of OPCs explain the lack of differences in qEPSC properties

The rise times and the amplitudes of the EPSCs are influenced by various resistive and geometric limitations imposed by the structure of a process. Passive and active K^+ and Cl^- conductances dampen the signal while voltage-activated Na^+ and Ca^{2+} channels recover and amplify the EPSCs. At neuronal synapses it is well documented that magnitude and shape of the EPSCs can change dramatically between the input location and soma, with the most distal synapses producing EPSCs with the largest amplitudes, progressively filtered down as the signal travels towards the soma. Those relationships are also true for OPCs where it was proved that Ca^{2+} signals recorded in the processes are modulated by various types of K^+ channels (Sun et al., 2016).

The available literature suggests that callosal OPCs become increasingly hyperpolarized during development and also increase K^+ and Na^+ current densities. Those changes could explain why the increases in Ca^{2+} permeability and single channel conductance did not result in different mEPSC kinetics or amplitudes across the different age groups. Therefore we investigated the passive properties, Na^+, K^+ A-type and K^+ steady-state current densities of OPC during callosal development in search for the answers.

In line with the literature, we found that the passive membrane properties of OPCs changed drastically during development. OPCs at P10 had a highest membrane resistance (R_m) of 1907.88 +/- 217.95 MΩ which strongly decreased at P20 to 420.53 +/- 44.30 MΩ and continued to decrease to reach 169.53 +/- 14.18 MΩ at P50, an 8-fold change compared with P10 [**Fig. 18A**; P10 vs P20, p=0.000000335; P10 vs P50, p=0.0000000164; P20 vs P50, p=0.0000124]. In line with the changes of R_m, the resting membrane potential (V_m) of OPCs decreased from -69.21 +/- 2.89 mV at P10 to -

87.787 +/- 0.828 mV at P20 to -92.76 +/- 0.46 mV at P50 [**Fig. 18B**; P10 vs P20, p=0.00000123; P10 vs P50, p=0.000000000902; P20 vs P50, p=0.0000000232]. Furthermore, the membrane capacitance (C_m) of OPCs was significantly increased from 18.77 +/- 0.88 pF at P10 to 25.28 +/- 1.12 at P20 but

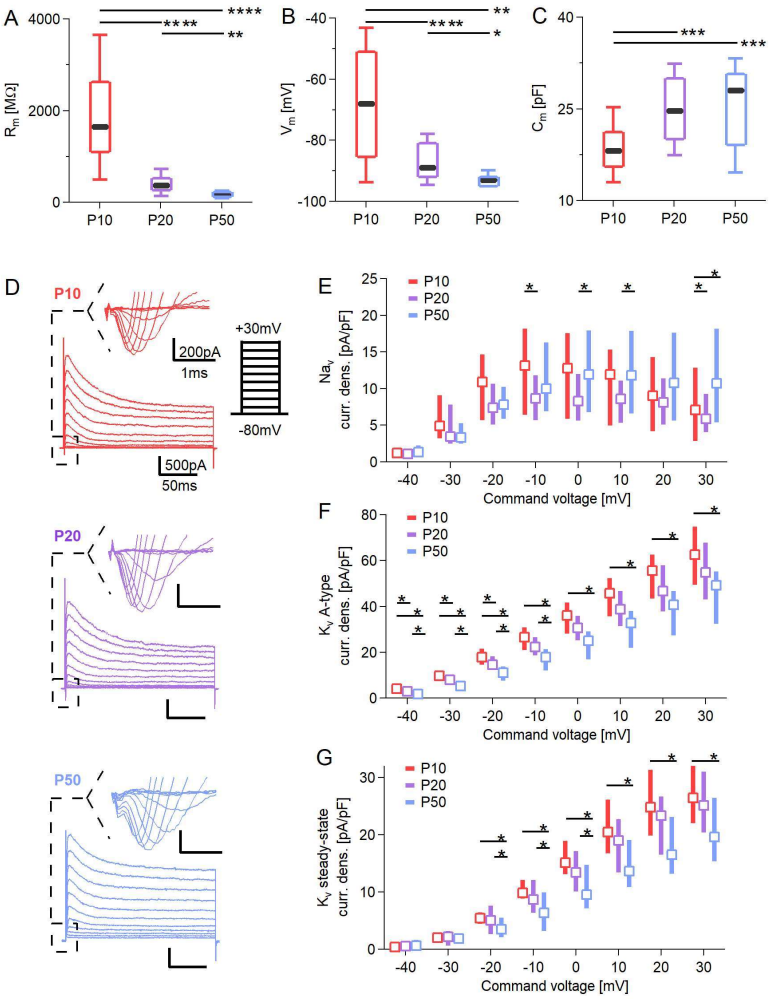

Figure 18. Basic membrane properties of OPCs (R_m, C_m, V_m) change during callosal development while most voltage-activated Na+, K+ channel currents do not.

(A): Comparison of membrane resistance (R_m) between experimental groups. Box plots represent 25th to 75th percentiles, whiskers represent 10th and 90th percentiles and the black bar is median. Black horizontal bars link significantly different groups. * = p<0.05; ** = p<0.01; *** = p<0.001. P10 group: n=34 in 27 animals. P20: n=38 in 33 animals. P50: n=27 in 25 animals. (B): Comparison of OPC resting membrane potential (V_m) between experimental groups, similar to (A). P10 group: n=43 in 31 animals. P20: n=89 in 71 animals. P50: n=37 in 29 animals. (C): Comparison of OPC membrane capacitance (C_m) between experimental groups, similar to (A). P10 group: n=34 in 27 animals. P20: n=38 in 33 animals. P50: n=27 in 25 animals. (D): Examples of OPC current responses to 11 incremental, 200ms long commanded voltage steps, increasing every 10mV from V_h = -80mV. In red, representative example for P10 group. In green, representative example for P20 group. In blue, representative example for P50 group. The examples are shown as recorded, without leak subtraction. The inset highlights fast activating Na+ current, characteristic for OPCs. The leak current was subtracted from every step shown in the inset. (E): Comparison of Na+ current responses to 11 incremental, 200ms long commanded voltage steps, increasing every 10mV from V_h = -80mV. The leak current was subtracted from every step. Currents were normalized to cell capacitance (shown in (D)). Box plots represent 25th to 75th percentiles, whiskers represent 10th and 90th percentiles and the black bar is median. Black horizontal bars link significantly different groups. * = p<0.05; ** = p<0.01; *** = p<0.001. P10 group: n=34 in 27 animals. P20: n=38 in 33 animals. P50: n=27 in 25 animals. (F): Comparison of K+ A-type current responses to 11 incremental, 200ms long commanded voltage steps, increasing every 10mV from V_h = -80mV, similar to (E). Currents were normalized to cell capacitance. P10 group: n=34 in 27 animals. P20: n=38 in 33 animals. P50: n=27 in 25 animals. (G): Comparison of K+ steady-state current responses to 11 incremental, 200ms long commanded voltage steps, increasing every 10mV from V_h = -80mV, similar to (E). Currents were normalized to cell capacitance. P10 group: n=34 in 27 animals. P20: n=38 in 33 animals. P50: n=27 in 25 animals.

remained stable at 25.42 +/- 1.52 pF at P50 [**Fig. 18C**; C_m: P10 vs P20, p=0.000214; P10 vs P50, p=0.000562; P20 vs P50, p=0.996] suggesting that decline in OPC number throughout development is compensated for by an increase in the process structure of the remaining cells and that this restructuring is largely complete by the third postnatal week.

Next, we analyzed the current patterns generated in response to 11 depolarization steps with +10mV increments (Δ) from the holding potential of -80 mV, shown in **Fig. 18D** for the three (P10, P20, and P50) ages. Typical current patterns of OPCs contain voltage-gated TTX-sensitive Na currents, transient K currents with rapid activation and deactivation kinetics (A-type), and sustained K currents with slow activation and deactivation (steady-state), when the leak (R_m) currents are subtracted. The density of Na currents remained comparable between the P10 and P20 groups with two differences at V_h = -10mV and +30mV [**Fig. 18E**; p=0.0467; p=0.0308] but no consistent trend. Surprisingly, P20 appeared as the group with the lowest Na_v density and tested as different from P50 starting from V_h = 0 till V_h = +10mV [**Fig. 18E**; p=0.0485, p=0.0317]. P10 and P50 tested as different only at V_h = +30mV [**Fig. 18E**; p=0.0372]. The inconsistencies in the trend suggest no change in subunit composition of Na_vs and are likely statistical fluctuations.

However, the A-type K^+ channels followed a different pattern, where P10 OPCs showed a consistently higher K^+ A-type density than P50 throughout all of the holding potentials [**Fig. 18F**; -40 to +30 mV, p=0.0000000301 to p=0.0258]. P10 OPC tested as having higher K^+ A-type density than P20 only throughout the early V_h of -40mV to -20mV [**Fig. 18F**; p=0.00154 to p=0.00979]. P20 and P50 showed a similar trend, with P50 testing as consistently lower at V_h = -40mV to -10mV [**Fig. 18F**; p=0.000361 to p=0.0254]. Unlike with Na_v density, P20 appeared to consistently remain between P10 and P50 groups suggesting continuous developmental downregulation of K^+ A-type channels.

The steady-stated K^+ currents observed after the K^+ A-type currents showed a pattern similar to K^+ A-types: P10 cells had the highest density of K^+ steady-state currents among all groups up to V_h = +30mV and tested as highly different from P50 OPCs throughout the V_h [**Fig. 18G**; V_h = -20mV to +30mV; p=0.0229 to p=0.000198]. P10 and P20 groups remained statistically comparable regardless of V_h, while P20 showed a significantly higher density of the currents from the earliest reasonably detectable values at V_h=-20mV to 0mV [**Fig. 18G**; p=0.0320, p= 0.0226, p=0.0336].

Overall, those changes could explain why the increases in Ca^{2+} permeability and single channel conductance did not result in different mEPSC kinetics or amplitudes across the different age groups.

4.4 Response probability at the neuron-OPC synapses is preserved during callosal development but short term plasticity of the synapses changes dramatically

Previously we established that the qEPSCs recorded at the OPC soma do not change significantly with age despite a remarkable shift in the Ca^{2+} permeability of OPC AMPARs and we discussed which mechanisms are likely responsible for this lack of change. As such, our investigation thus far showed that the first component of synaptic strength (I = pqN), quantal size (q), is preserved throughout CC development by a combination of two opposing forces: substitution of AMPAR subunits by ones with higher conductance, counterbalanced by increases in passive and active K^+ conductances. Next, we looked into the second component of synaptic strength, release probability (p).

Neuronal literature shows numerous examples of developmentally driven changes to release probability of central synapses. Based on the release probability most synapses in the CNS can be divided into 2 subcategories, serving different functions: High-release probability synapses which usually undergo short term depression (STD, as in the cerebellum), functioning as high fidelity detectors of the initial input, which desensitize if the input is present repeatedly or low release probability synapses undergoing potentiation, therefore functioning as detectors of repetitive or periodic input. Currently very little is known about resp. prob. at neuron-OPC synapses during callosal development. During adulthood the synapses tend to strongly potentiate and in gray matter may display some characteristics of long term potentiation (LTP) upon repetitive stimulation.

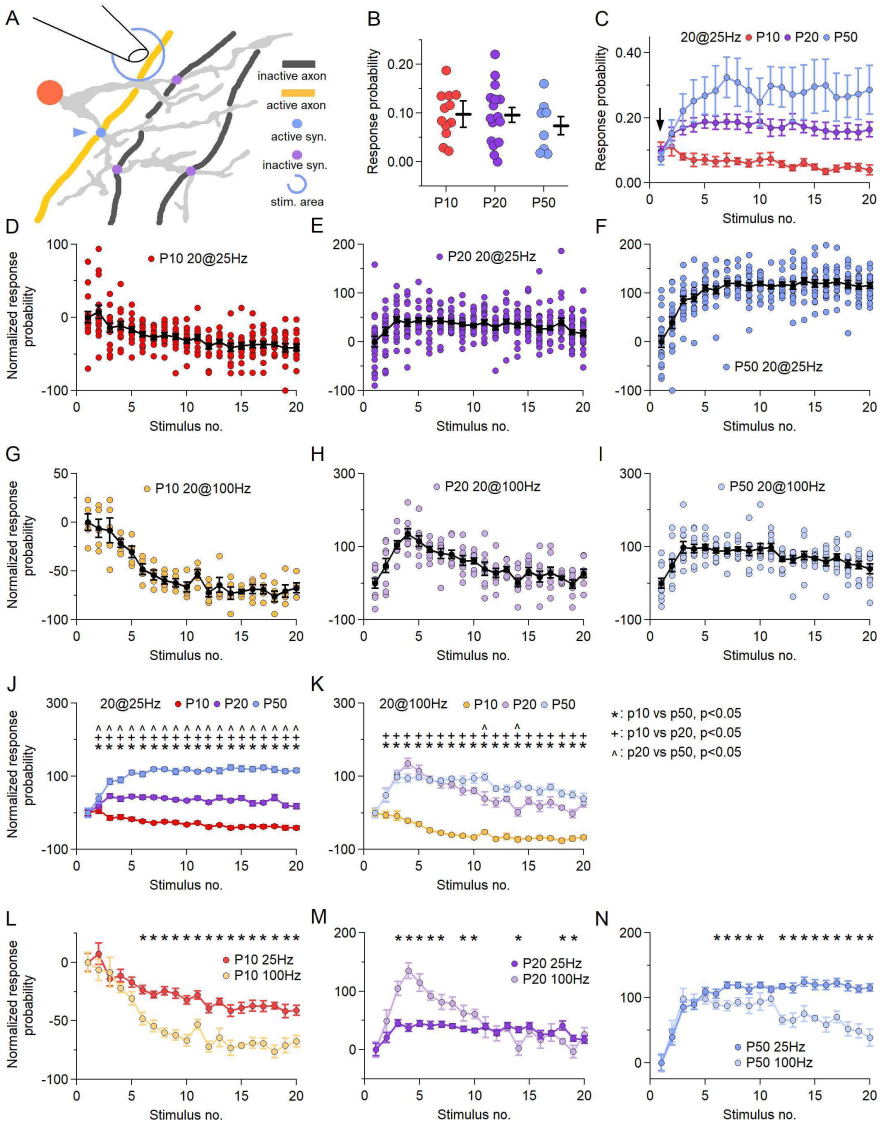
A
inactive axon
active axon
active syn.
inactive syn.
stim. area
B
Response probability
P10
P20
P50
C
20@25Hz P10 P20 P50
Response probability
Stimulus no.
D
P10 20@25Hz
Normalized response probability
Stimulus no.
E
P20 20@25Hz
Stimulus no.
F
P50 20@25Hz
Stimulus no.
G
P10 20@100Hz
Normalized response probability
Stimulus no.
H
P20 20@100Hz
Stimulus no.
I
P50 20@100Hz
Stimulus no.
J
20@25Hz P10 P20 P50
Normalized response probability
Stimulus no.
K
20@100Hz P10 P20 P50
Stimulus no.
*: p10 vs p50, p<0.05
+: p10 vs p20, p<0.05
^: p20 vs p50, p<0.05
L
P10 25Hz
P10 100Hz
Normalized response probability
Stimulus no.
M
P20 25Hz
P20 100Hz
Stimulus no.
N
P50 25Hz
P50 100Hz
Stimulus no.

Figure 19. Response probability of EPSCs evoked in OPCs during train stimulation of CC changes during callosal development.

(A): A schematic representing the principle of minimal stimulation. The drawing represents a single OPC process coming into contact with 3 axons, forming 4 synapses. Stimulation voltage used to evoke EPSC responses during minimal stimulation is low enough to activate a single axon (in orange). (B): Scatter plot of the response probability to the first stimulus in a train of 20 stimuli applied at 25Hz. Each circle represents one cell. Black bars represent group average ± SEM. P10 (red): n=12 in N=11 animals; P20 group: n=16 in N=15 animals; P50 group: n=8 in N=8 animals. None of the groups tested as significantly different (One-way ANOVA, p=0.593). (C): EPSCs response pattern evoked by minimal stimulation of callosal axons with a train of 20 stimuli applied at 25 Hz, compared between age groups. Each circle represents the probability to see a response to a single stimulus for the age group. Labels, markings, n and N are identical to (B). The arrow points to the initial response probability as plotted in (B). (D) – (F): Normalized response probability of EPSCs evoked by a train of 20 stimuli at 25 Hz stimulation of callosal axons, compared between age groups. Each circle represents a normalized averaged probability to see a response to a single stimuli recorded in a single OPC over 20-100 trials. Black circles represent group mean ± SEM. (D): n=15 OPCs in N=14 animals, recorded at P10; (E): n=23, N=18 at P20; (F): n=19, N=16 at P50. (G) – (I): EPSCs response probabilities evoked by a train of 20 stimuli at 100 Hz stimulation of callosal axons, compared between age groups. Each circle represents a normalized, averaged probability to see a response to a single stimuli recorded in a single OPC over 20-100 trials. Black circles represent group mean ± SEM. (G): n=14, N=10 at P10; (H): n=19, N=14 at P20; (I): n=9, N=9 at P50. (J): Summary of (D) – (F), EPSCs response pattern evoked by 20 stimuli at 25Hz, compared between groups: Each circle represents the group mean ± SEM. P10 in red, P20 in green, P50 in blue. * = $p<0.05$, P10 vs P50. + = $p<0.05$, P10 vs P20. # = $p<0.05$, P20 vs P50. (K): Summary of (G) – (I), EPSCs response pattern evoked by 20 stimuli at 100Hz, compared between groups: Each circle represents the group mean ± SEM. P10 in orange, P20 in lime, P50 in violet. * = $p<0.05$, P10 vs P50. + = $p<0.05$, P10 vs P20. # = $p<0.05$, P20 vs P50. (L): Comparison of the response probabilities of EPSCs during 20 stimuli at 25 Hz and 100 Hz for the P10 group. The plots are identical to group means ± SEM in (D) and (G). * = $p<0.05$. (M): Comparison of the response probabilities of EPSCs during 20 stimuli at 25 Hz and 100 Hz for the P20 group.The plots are identical to group means ± SEM in (E) and (H). * = $p<0.05$. (N): Comparison of the response probabilities of EPSCs during 20 stimuli at 25 Hz and 100 Hz for the P50 group. The plots are identical to group means ± SEM in (F) and (I). * = $p<0.05$.

We started by checking whether the initial p at single synapses changes during CC development. We used minimal stimulation technique [see **Fig. 19A**], which allows for controlled activation of a single axon (and presumably a single synaptic connection) over 50 to 150 trials to accurately judge the initial release probability. We found an almost identical p of ~0.1 preserved at all investigated ages [**Fig. 19B**; 0.0975 +/- 0.0140 at P10, 0.0956 +/- 0.0152 at P20, 0.0736 +/- 0.0186 at P50; p=0.593]. Next, we investigated whether any form of short term plasticity can be found at neuron-OPC synapses and how it changes under two different stimulation paradigms: trains of 20 stimuli applied at 25 Hz or trains of 20 stimuli applied at 100 Hz, both repeated every 20s for 20-50 repetitions.

In the youngest animals (P10) we observed a depression developing during the 20 at 25 Hz train [**Fig. 19D**; -38.51 +/- 4.43%], which was almost twice more pronounced during the 20 at 100Hz trains [**Fig.19G**; -67.36 +/- 4.92%]. However, at P20 in the majority of cells we observed potentiation rather than depression during both stimulation paradigms, although with different time-courses: During 20 at

25 Hz trains p reached the peak ~3rd stimulus [**Fig. 19E**; +45.30 +/- 5.94%] and declined to roughly half of that value by the end of the stimulation [**Fig. 19H**; stim. 20, +17.39 +/- 6.27%]. During 20 stimuli at 25 Hz trains p reached the peak ~3rd stimulus, more than doubling compared to the initial p [**Fig. 19E**; +134.98 +/- 13.59%] with a sharp decline afterwards but still remained potentiated [**Fig. 19E**; stimulus 20, +26.34 +/- 11.33%]. Interestingly, a very different pattern developed at P50 where during 20 stimuli at 25 Hz trains p continued to potentiate with subsequent pulses reaching a plateau ~stimulus 10 [**Fig. 19F**; +119.45 +/- 4.53%] and remained stable around that value till the end of the stimulation [**Fig. 19I**; stimulus 20, +115.60 +/- 5.65%]. At 20 at 100Hz changes in p partially replicated the pattern observable at P20, with a peak ~3rd stimulus [**Fig. 19I**; +98.22 +/- 15.71%] with a slightly milder decline [**Fig. 19F**; stimulus 20, +38.51 +/- 13.04%]. When we compared all of the experimental groups, at 20 at 25 Hz the P10 time-courses were different from P20 and P50 throughout the entirety of the stimulation, while P20 and P50 started to differ from stimulus 3 [**Fig. 19J**]. For the 20 at 100Hz the P10 time-courses remained highly different from P20 and P50 throughout the whole stimulation but the P20 and P50 groups did not test as consistently different [**Fig. 19K**].

When we compared the response probabilities during the trains we found consistent differences between the stimulation paradigms in all of the groups [**Fig. 19L-N**; p=0.00299 to p=0.000000330 at P10, p=0.0445 to p=0.0000000497 at P20, p=0.0131 to p=0.00000187 at P50]. This highlights the critical importance of the neuronal activity pattern in the development of different forms of short term plasticity at OPC synapses.

4.5 Priming of vesicular release changes during callosal development

Next, we investigated whether the onset of the vesicular release changed during development. We reasoned that the changes we observed in release probability should be reflected in the priming of the vesicles, resulting in a more reliable transmission with a decreased latency between the stimulus and the triggered EPSC and reduced variance of the onset. We analyzed the latency within a 5ms time frame from the start of the stimulation but due to heavy myelination of the callosal fibers resulting in fast action potential conduction velocities we normalized all of the latency values to the first stimulus in the trains, assuming they would be representative of the recovered vesicular pool at the presynapse [**Fig. 20A, B**].

At P10 we found a progressive delay in the EPSC latencies developing within the 20 stimuli at 25 Hz trains, reaching a +0.625 +/- 0.115ms delay by the end of the train [**Fig. 20C**]. In contrast, P20 synapses showed a very different trend with a brief increase in release speed at the beginning of the rain, -0.144 +/- 0.0899ms increase at stimuli 5, followed by a much milder delays, +0.150 +/- 0.0810ms at maximum, compared to P10, with P20 and P10 testing as highly different through most of

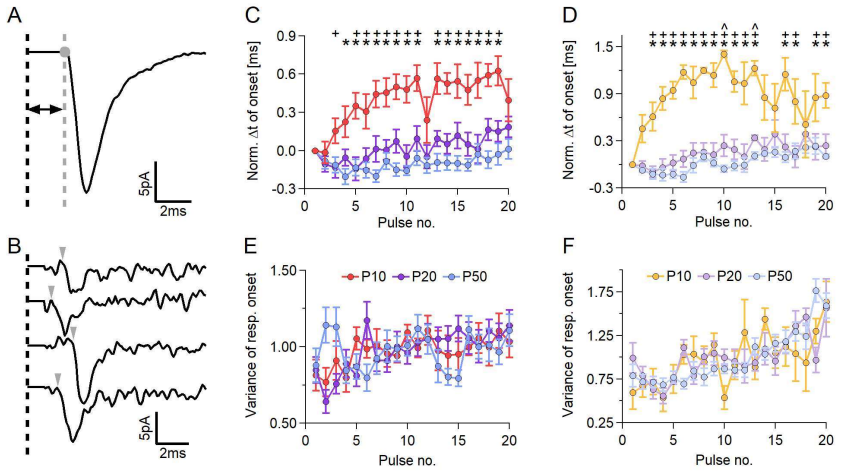

Figure 20. During callosal development the timing of responses improves during train stimulation.

(A): An example of an averaged EPSC recorded in response to the first stimuli in a train, in a single P50 OPC. The black dashed line represents the start of the stimulation (the stimulation artifact is removed for clarity). Grey dashed line and circle represent the onset of the EPSC. Black arrows mark the time between the stimuli and the onset of the EPSC. (B): A set of single EPSC with different amplitudes and onsets, triggered by the first stimuli in a train, recorded in 4 trials in a single P50 OPC, plotted together to highlight the variability in their timing. The black dashed line represents the start of the stimulation (the stimulation artifact is removed for clarity). The gray arrowheads represent the time points of the EPSC onsets. (C): The EPSC onsets measured throughout a train of 20 stimuli at 25Hz, compared between age groups. Each circle represents the normalized group mean ± SEM. P10 in red, n=15, N=14; P20 in green, n=23, N=18; P50 in blue, n=19, N=16. * = p<0.05, P10 vs P50. + = p<0.05, P10 vs P20. # = p<0.05, P20 vs P50. (D): The EPSC onsets measured throughout a train of 20 stimuli at 100Hz, compared between age groups. Each circle represents the normalized group mean ± SEM. P10 in orange, n=14, N=10; P20 in lime, n=19, N=14; P50 in violet, n=9, N=9. * = p<0.05, P10 vs P50. + = p<0.05, P10 vs P20. # = p<0.05, P20 vs P50. (E): A summary of EPSC onset variance throughout a train of 20 stimuli at 25Hz, compared between age groups. Each circle represents the normalized group mean ± SEM. P10 in red, n=15, N=14; P20 in green, n=23, N=18; P50 in blue, n=19, N=16. There were no significant differences between groups. (F): A summary of EPSC onset variance throughout a train of 20 stimuli at 100Hz, compared between age groups. Each circle represents the normalized group mean ± SEM. P10 in orange, n=14, N=10; P20 in lime, n=19, N=14; P50 in violet, n=9, N=9. There were no significant differences between groups.

the stimulation [**Fig. 20C**; p=0.000128 to p=0.0452]. P50 synapses followed a trend very similar to the one of P20 but after the initial onset alway showed increased release speed and never developed delays [**Fig. 20C**; -0.205 +/- 0.0627ms at the fastest, -0.0290 +/- 0.0836ms by the end of the train].

P50 and P10 were highly different almost throughout the whole train [**Fig. 20C**; p=0.0171 to p=0.00000236]. P20 and P50 groups did not test as different at any point [**Fig. 20C**; p=0.0954 to p=0.985].

Next, we compared the 20 pulses at 100 Hz trains and we received an almost identical result: At P10 we found a similar progressively higher delay but much stronger than for 20 at 25 Hz trains, reaching +1.409 +/- 0.0424ms at maximum. In addition, after the 10th stimulus responses became exceedingly rare and erratic (as evident from the greatly increased variance), suggesting a depletion of the pool of vesicles at the synapse [**Fig. 20D**]. To the contrary, in the P20 group we saw a pattern similar to the one visible during 25 Hz stimulation, where after a brief decrease in the onset, -0.0974 +/- 0.0735ms at peak, much milder in comparison with P10, progressive delays appeared after stimulus 6 [**Fig. 20D**; +0.0217 +/- 0.0982ms; +0.389 +/- 0.177ms at maximum]. P50 synapses, also replicated a pattern comparable with 25 Hz, decreasing the time of the onset until stimulus 6 with -0.165 +/- 0.0667ms latency, but eventually developing mild, progressive delays in the second half of the train, reaching +0.236 +/- 0.103ms at maximum. As with the 25 Hz trains, P10 synapses were highly different from P20 and P50 throughout the entire train [**Fig. 20D**; p=0.0000000512 to p=0.0418, P10 vs P20; p=0.000000000260 to p=0.0302, P10 vs P50]. P20 and P50 groups were only different incidentally at stimuli 10 and 13 [**Fig. 20D**; p=0.0242 and p=0.0223].

Finally, we analyzed the variance in the onset and we found an almost identical trend in all of the groups for both stimulation paradigms [**Fig. 20E, F**]. The individual, significant differences appeared highly incidental.

4.6 Changes in the short term plasticity indirectly translate into differences in the magnitudes of evoked EPSCs at the neuron-OPC synapses

With no changes in q and the developmentally driven differences in the time-course of p we would expect that the amplitudes of EPSCs evoked at the neuron-OPC synapses should follow a response pattern very comparable with the time-course of p. Therefore to investigate this hypothesis we measured the peak amplitudes of evoked EPSCs during both stimulation paradigms and compared the time-courses between the groups.

We found that the time-courses of EPSC amplitudes during both stimulation paradigms had similar shapes to the time-courses of response probability [**Fig. 19**] but, surprisingly, both depression and potentiation were much more prominent for time-courses of eEPSCs amplitude than for the time-courses of response probability. At P10 animals we observed that the depression during the 20 stimuli

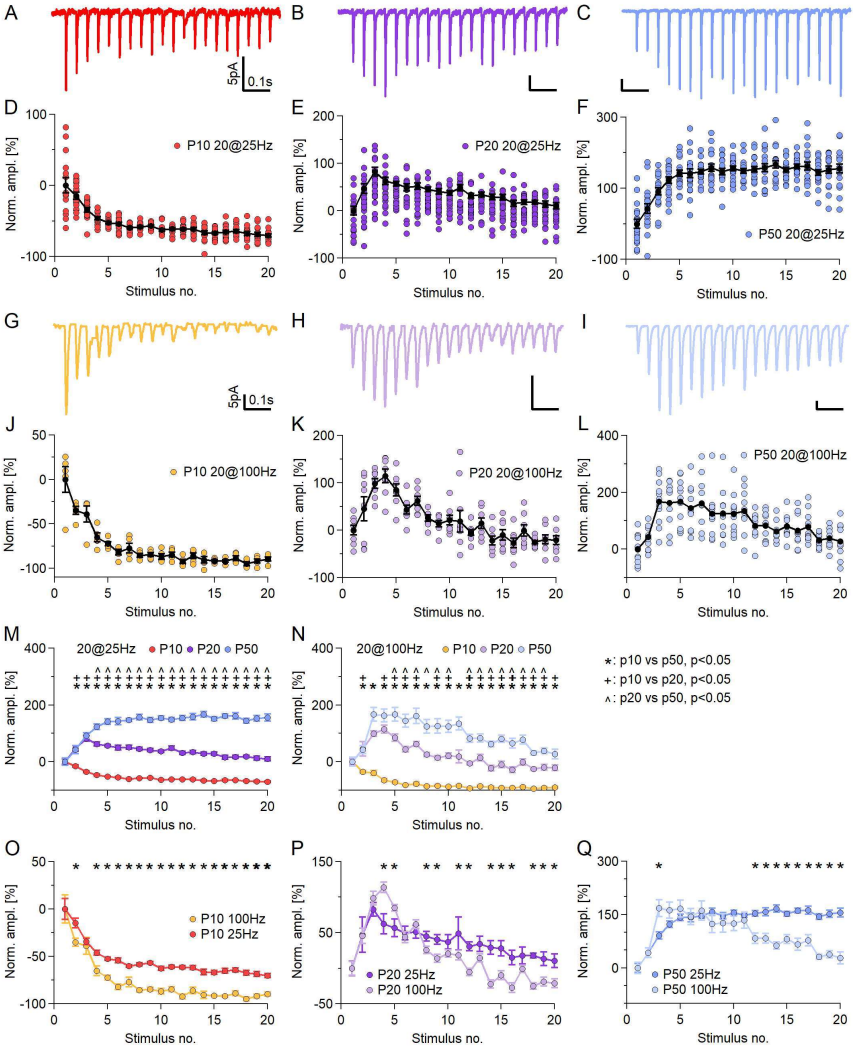
A
B
C
5pA
0.1s
D
E
F
P10 20@25Hz
P20 20@25Hz
P50 20@25Hz
Norm. ampl. [%]
Stimulus no.
G
H
I
J
K
L
P10 20@100Hz
P20 20@100Hz
P50 20@100Hz
M
N
20@25Hz P10 P20 P50
20@100Hz P10 P20 P50
*: p10 vs p50, p<0.05
+: p10 vs p20, p<0.05
^: p20 vs p50, p<0.05
O
P
Q
P10 100Hz
P10 25Hz
P20 25Hz
P20 100Hz
P50 25Hz
P50 100Hz

Figure 21. Response pattern of EPSCs evoked in OPCs during train stimulation of CC changes during callosal development.

(A) – (C): Representative response patterns of EPSCs evoked in single callosal OPCs during a 20 stimuli at 25 Hz train stimulation of callosal axons. Example shown is an average of 20-60 recorded traces. (A): P10 in red. (B): P20 in green. (C): P50 in blue. (D) – (F): EPSCs response pattern evoked by a train of 20 stimuli at 25 Hz stimulation of callosal axons, compared between age groups. Each circle represents a normalized average of EPSCs recorded in a single OPC over 20-100 trials. Black circles represent group mean ± SEM. (D): n=15 OPCs in N=14 animals, recorded at P10; (E): n=23, N=18 at P20; (F): n=19, N=16 at P50. (G) – (I): Representative response patterns of EPSCs evoked in single callosal OPCs during a 20 stimuli at 100Hz train stimulation of callosal axons. Example shown is an average of 20-60 recorded traces. (A): P10 in orange. (B): P20 in lime. (C): P50 in violet. (J) – (L): EPSCs response pattern evoked by a train of 20 stimuli at 100 Hz stimulation of callosal axons, compared between age groups. Each circle represents a normalized average of EPSCs recorded in a single OPC over 20-100 trials. Black circles represent group mean ± SEM. (J): n=10, N=14 at P10; (K): n=19, N=14 at P20; (L): n=9, N=9 at P50. (M): Summary of (D) – (F), EPSCs response pattern evoked by 20 stimuli at 25Hz, compared between groups: Each circle represents the group mean ± SEM. P10 in red, P20 in green, P50 in blue. * = $p<0.05$, P10 vs P50. + = $p<0.05$, P10 vs P20. # = $p<0.05$, P20 vs P50. (N): Summary of (J) – (L), EPSCs response pattern evoked by 20 stimuli at 100Hz, compared between groups: Each circle represents the group mean ± SEM. P10 in orange, P20 in lime, P50 in violet. * = $p<0.05$, P10 vs P50. + = $p<0.05$, P10 vs P20. # = $p<0.05$, P20 vs P50. (O): Comparison of response patterns between 20 stimuli at 25 Hz and 20 stimuli at 100Hz in the P10 age group. Labels and markings are identical to (M) and (N). * = $p<0.05$. (P): Comparison of response patterns between 20 stimuli at 25 Hz and 20 stimuli at 100Hz in the P20 age group. Labels and markings are identical to (M) and (N). * = $p<0.05$. (Q): Comparison of response patterns between 20 stimuli at 25 Hz and 20 stimuli at 100Hz in the P50 age group. Labels and markings are identical to (M) and (N). * = $p<0.05$.

at 25 Hz train was almost twice more prominent for EPSCs than what we saw in resp. prob. [**Fig. 21D**; stimulus 20, -70.37 +/- 2.29%; versus **Fig. 19D**; -38.51 +/- 4.43%], while retaining the same continuous decline. Moreover, a similar but less pronounced effect was visible for the 20 at 100Hz trains, where EPSC amplitudes declined by -89.65 +/- 2.13% by the end of the train (**Fig. 21J** compared with **Fig. 19G**; -67.36 +/- 4.92%). EPSCs in the adolescent, P20 animals reached peak at the same stimulus as what would be expected from the resp. prob. distribution but potentiated stronger [**Fig. 21E**; +82.57 +/- 9.65%, versus **Fig. 19E**; +45.30 +/- 5.94%] and declined more by the end of the train [**Fig. 21E**; stim. 20, +10.24 +/- 6.39%, versus **Fig. 19E**; +17.39 +/- 6.27%) but still remained potentiated throughout the stimulation. This trend was different for the 20 at 100Hz trains which peaked at +114.01 +/- 14.10% [**Fig. 21K** versus **Fig. 19H**; +134.98 +/- 13.59%] and eventually depressed to -21.44 +/- 9.51 at stimulus 20 [**Fig 21K** versus **Fig. 19H**, +26.34 +/- 11.33%]. At P50 we saw yet again that EPSCs reached a plateau ~stimulus 10 during 20 at 25Hz trains but with a slightly higher value than for resp. prob. [**Fig. 21F**, +154.82 +/- 7.21% versus **Fig. 19F**; +119.45 +/- 4.53%]. For the 20 at 100Hz trains the amplitudes reached the peak at the same stimulus as what would be

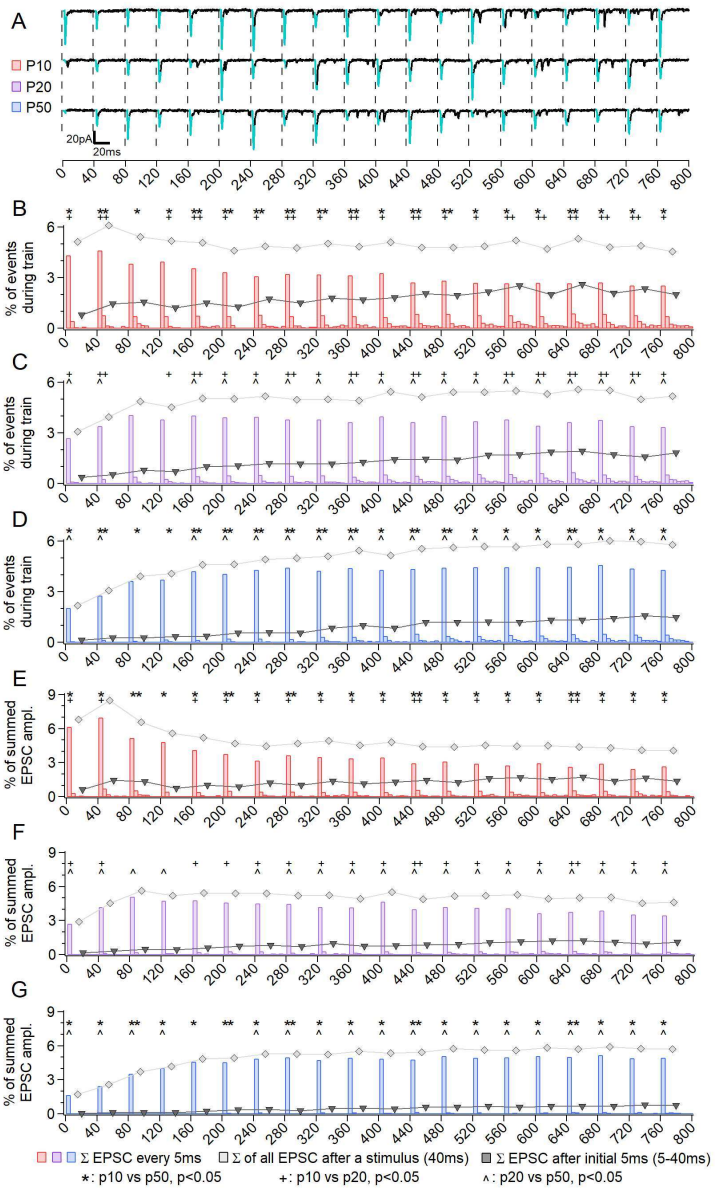
A
P10
P20
P50
20pA
20ms
B
C
D
E
F
G
% of events during train
% of summed EPSC ampl.
Σ EPSC every 5ms
Σ of all EPSC after a stimulus (40ms)
Σ EPSC after initial 5ms (5-40ms)
*: p10 vs p50, p<0.05
+: p10 vs p20, p<0.05
∧: p20 vs p50, p<0.05

Figure 22. During callosal development neurotransmitter release at OPC synapses becomes more synchronized. (A): 3 examples of EPSCs evoked in a P50 OPC by a train of 20 stimuli at 25Hz, with the whole 800ms stimulation shown. In turquoise the phasic part of the response (first 5ms post-stimulus) and in black the asynchronous part of the response (>5ms to 40ms post-stimulus). (B): The mean fraction (%) of the number of EPSCs evoked by a train of 20 stimuli at 25Hz (800ms), binned every 5ms in the P10 age group. Each colored bar represents the ratio of EPSC every 5ms to the total number of EPSCs within 800ms of the train. The black triangle is the summed percentage of EPSCs in the asynchronous part of the response (>5ms, ≤40ms). The gray diamond is the summed percentage of all EPSCs triggered by a single stimulus (40ms). (C): The same as (B) for the P20 age group. (D): The same as (C) for the P50 age group. (E): The sum of EPSC amplitudes evoked by a train of 20 stimuli at 25Hz (800ms), binned every 5ms in the P10 age group. Each colored bar represents the sum of EPSC amplitudes every 5ms divided by the total sum of all EPSC amplitudes within 800ms of the train. The black triangle is the sum of EPSC amplitudes in the asynchronous part of the response (>5ms, ≤40ms). The gray diamond is the sum of all EPSC amplitudes triggered by a single stimulus (40ms). (F): The same as (E) for the P20 age group. (G): The same as (E) for the P50 age group.

expected from the resp. prob. distribution [**Fig. 21L**; +91.45 +/- 10.37% versus **Fig. 19I**; +98.22 +/- 15.71%] but declined a little more sharply [**Fig. 21L**; stimulus 20, +27.77 +/- 17.3 versus **Fig. 19I**; +38.51 +/- 13.04%], while remaining potentiated. Therefore we can conclude that while P50 animals had the smallest differences in time-courses of resp. prob. and EPSCs, the P10 animals had the largest. When we compared all of the experimental groups, at 20 at 25 Hz the P10 time-courses (the same as for resp. prob.; **Fig. 19D-F, J-K**) were different from P20 and P50 throughout the entirety of the stimulation, while P20 and P50 again started to differ from stimulus 3 [**Fig. 21M**].

For the 20 at 100Hz the P10 time-courses remained highly different from P20 and P50 throughout the whole stimulation and the P20 and P50 groups (in contrast to resp. prob. time-course) started to test as consistently different from stim. 5 [**Fig. 21N**]. Interestingly, not only were the groups different from each other but the response patterns also tested as having different progression when we compared the 20 at 25 Hz and 20 at 100 Hz stimulations within the groups [**Fig. 21O-M**; p=0.0362 to 0.00000000197 at P10, p=0.0201 to p=0.0000000780 at P20, p=0.0122 to p=0.00000000151 at P50], similar to corresponding trends in **Fig. 19** but with stronger effects, both for depression and potentiation.

4.7 During callosal development OPC-neuron synapses increase reliability of transmission and decrease asynchronicity of release

The effects visible in eEPSC amplitudes [**Fig. 21**] are larger than ones seen in response probability [**Fig. 19**], which implies (in STD synapses) either lower number of synapses activated per stimulus or the desynchronization of the inputs. In STP synapses each subsequent stimulus either recruits more synapses or inputs synchronize better. Our analysis of changes to EPSC onsets during

stimulation shows that desynchronization/synchronization does happen. Therefore, to test the contribution of those effects to the total synaptic transmission we looked into the % of eEPSCs and the sums of eEPSC amplitudes during the whole length of a train (800ms) subdivided into 5ms blocks. [**Fig. 22**].

First, let's consider the number of EPSCs during the train. Due to differences in the number of synapses in each OPC we divided the number of EPSC every 5ms by the total number of EPSCs within the train. The first clear trend visible in all of the groups is the huge disparity between the number of EPSCs triggered within 5ms of the stimulus (synchronous, synEPSC) and the EPSCs triggered with a delay (>5ms, desynchronized, deEPSC). All of the deEPSCs combined throughout the whole train make 36.297% of the total EPSCs at P10, 25.194% at P20 and 16.530% at P50, but only 15.564% directly after the first stimulus (first 40ms) at P10, 11.923% at P20 and just 5.844% at P50 [**Fig. 22B-D**]. In all of the groups the desynchronization increases with successive stimuli, reaching 48.038% at P10, 35.256% at P20 and 26.441% at P50, roughly 3-4 times higher than the initial number. Interestingly, the groups were only statistically different within the first 10 ms after each stimulus, suggesting that strongly desynchronized release is so rare that it can be considered of low importance. Most strikingly, when both synchronous and asynchronous release is considered together the P10 OPCs show a much lower degree of depression than what we reported in **Fig. 19D.** P20 cells showed a very mild continuous potentiation while P50 cells potentiated continuously and clearly (compare with **Fig. 19E**, **F**). This points to ongoing desynchronization of vesicular release as a powerful component of short term plasticity.

Next, we looked into the amplitudes of the EPSCs to see whether the input summation is changing during development. Signals from different synapses must be efficiently integrated to become meaningful for a cell, therefore an increase in the number of EPSC would amount to merely an increase in the noise if those signals are not sufficiently large to have biological effects. To account for that we summed the amplitudes of all EPSCs released within the 5ms time windows and divided the number by the total sum within the train. The outcome was similar to the previous analysis [**Fig. 22B-D**] but progressing closer to the trends we saw in **Fig. 21.** deEPSCs amplitudes combined throughout the whole train make 27.187% of the total EPSCs at P10, 16.445% at P20 and 8.726% at P50, but 9.406% at P10, 6.499% at P20 and 3.132% at P50 after the first 40ms. In all of the groups, with successive stimuli we observed a progressive desynchronization (as in **Fig. 22B-D**), but the fractions of total amplitudes were lower [**Fig. 22 E-G**], 33.375% (compared to 48.038%, **Fig. 22B**) at P10, 24.275% (35.256%, **Fig. 22C**) at P20 and 13.149% (26.441%, **Fig. 22D**) at P50, highlighting that the desynchronized EPSC have either lower initial amplitudes and/or do not properly integrate. This conversely would mean that the early synaptic transmission (shortly after a stimulus) is much better

synchronized between different inputs. Surprisingly, the groups were only consistently statistically different within the first 5 ms after each stimulus, meaning that desynchronized release is rare and does not change significantly during CC development.

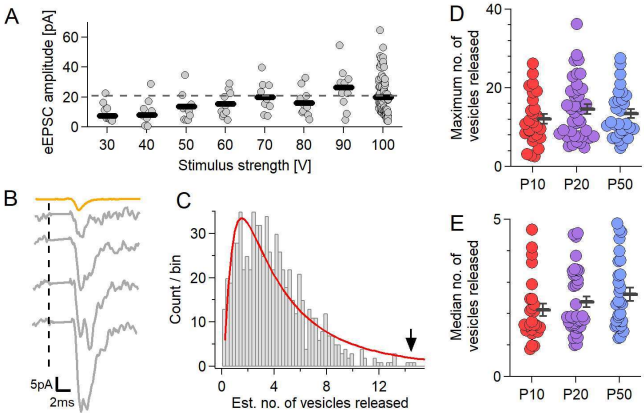

Figure 23. The number of release sites at OPC synapses does not change over callosal development.
(A): Amplitudes of EPSCs evoked in a single P20 OPC by stimulation of increasing strength, from 30V to 100V in +Δ10V increments. Each circle represents a single eEPSC amplitude, black bars represent the mean per stimulation strength. The dashed, gray line represents the maximum average amplitude reached by the end of the stimulation (70V-100V) and is considered to activate all synaptic connections (maximal stimulation). (B): Example eEPSCs recorded during maximal stimulation compared with an averaged quantal qEPSC from the same cell. The averaged qEPSC is in orange, eEPSCs are in gray, all with the same scaling. The black dashed line represents stimulus artifacts (blanked for clarity). (C): A histogram of all eEPSCs recorded during maximal stimulation in (E), scaled to the averaged qEPSC from the same cell (Q maxEPSC / Q qEPSC), used as an estimation of the released neurotransmitter vesicles during stimulation of multiple axons. The red line is the best fit of a log normal function to the skewed distribution. The black arrow points to the largest number of vesicles released during the stimulation (~15 vesicles). (D): The maximum number of vesicles released during maximal stimulation, compared between the age groups. Each circle represents the maximum in a single cell, black bars represent group mean ± SEM. P10 in red, n=27 cells; P20 in purple, n=40; P50 in blue, n=29. (E): The median number of vesicles released during maximal stimulation, compared between the age groups. Each circle represents the median of a single cell, black bars represent group mean ± SEM. P10 in red, n=27 cells; P20 in purple, n=40; P50 in blue, n=29.

4.8 The number of synaptic release sites does not change during callosal development

Lastly, we investigated whether the final component of synaptic strength, the number of release sites (N) changed during callosal OPC development. We probed the number of N by applying the

following paradigm: with increases in the stimulation strength more axons and therefore more synapses can be recruited to participate in the evoked EPSCs, resulting in gradual increase in EPSC charge/amplitude with increased stimulation strength. However, at a certain strength all available synapses are recruited and increase in stim. strength no longer produces increases in EPSC charge/amplitude [maximal stimulation is reached, **Fig. 23A**]. Moreover, all of the evoked EPSC charges can be scaled to the qEPSC charge from the same cell giving an estimate of the number of NT vesicles released. Assuming 1 vesicle released at a synapse per single stimuli, with sufficient number of repetitions the maximum N can be estimated from the distribution [**Fig. 23B, C**].

We found no significant differences in the maximum [**Fig. 23D**; p = 0.545; 12.702 +/- 1.518 at P10, 14.734 +/- 1.589 at P20, 15.630 +/- 2.265 at P50] or median [p = 0.229; 2.556 +/- 0.410 at P10, 2.517 +/- 0.337 at P20, 3.207 +/- 0.427 at P50] number of vesicles released during maximal stimulation therefore, presumably, also no differences in N.

4.9 During callosal development OPC increase in size with a complimentary increase in the number of branches but do not grow additional processes

The early works discussing OPC morphology focused mainly on general morphology with few measurements, mostly focusing on general appearance, number of processes and process length. Therefore first we focused on analyzing the general morphology of the cells. We counted the number of processes, process length, number of branches, branch length, number of br. points and endings. Our data show no significant differences in the overall number of processes between groups [**Fig 24B**; 20.15 ± 2.19 at P10; 20.33 ± 2.17 at P20; 16.62 ± 1.76 at P50; p=0.357]. However, the total length of the process structure increased by 33.07 ± 13.24% at P20 and by 27.62. ± 13.51% at P50 (compared to P10). P20 and P50 were not significantly different [**Fig. 24C**; 1340.44 ± 92.34 at P10; 2002.62 ± 152.94 at P20; 1851.85 ± 132.65; P10,P20 p=0.002; P10,P50 p=0.020; P20,P50 p=0.790]. The increase in process length could come from multiple possible mechanisms: the elongation of existing branches or an increase in the number of branches at each process or a combination of both. To test this we checked whether the branches, branch length, br. points or endings [**Fig. 25C**] changed in numbers. We found an increase in the number of branches [**Fig 25E;** 498.54 ± 36.22 at P10; 725.67 ± 70.36 at P20; 674.69 ± 40.54 at P50; P10 vs P20 p=0.009; P10 vs P50 p=0.048; P20 vs P50 p=0.855], no. of endings [**Fig 2G**; 277.54 ± 20.30 at P10; 396.67 ± 38.75 at P20; 367.23 ± 21.72 at P50; P10 vs P20 p=0.013; P10 vs P50 p=0.074; P20 vs P50 p=0.835] and br. points [**Fig 25H;** br. points: 221.00 ± 16.13 at P10; 328.92 ± 31.70 at P20; 307.46 ± 18.88 at P50; P10 vs P20 p=0.006; P10 vs P50 p=0.029; P20 vs P50 p=0.880] of ~30%, closely following the change in process lengths.

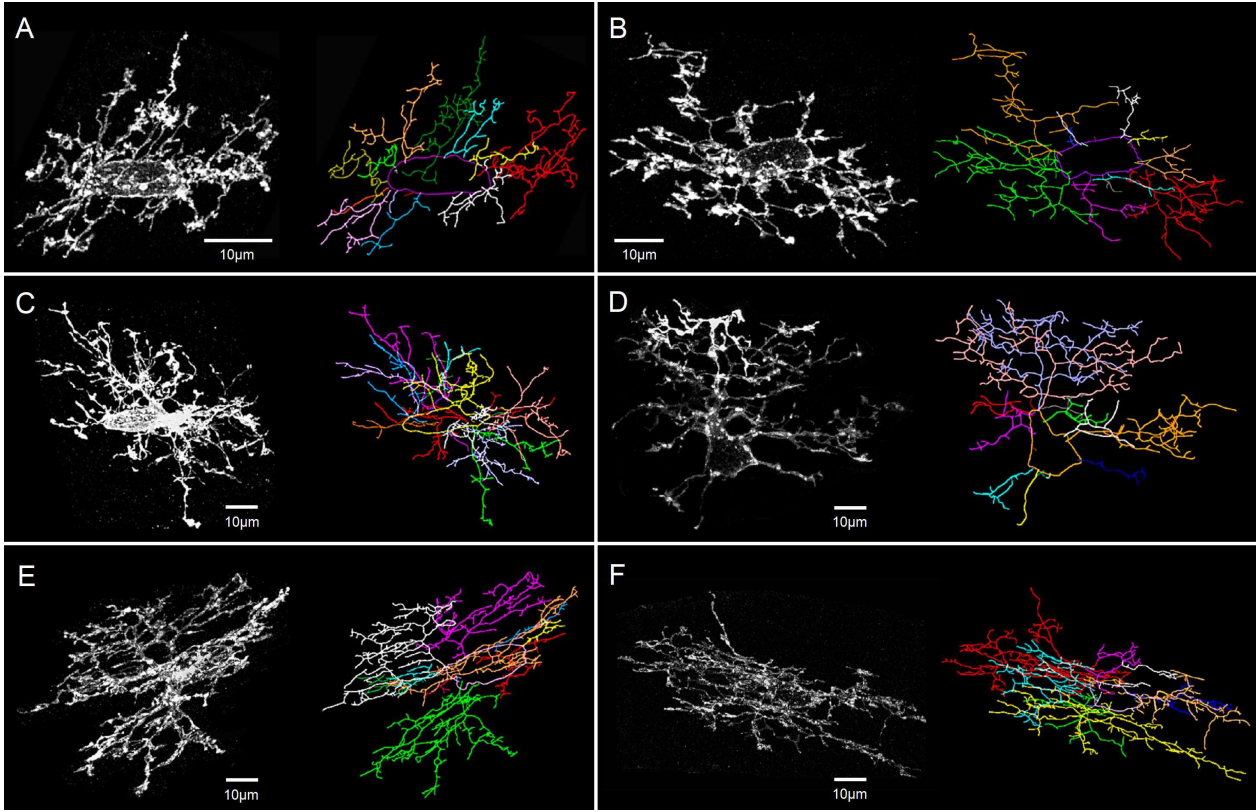
A
10µm
B
10µm
C
10µm
D
10µm
E
10µm
F
10µm

Figure 24. Callosal OPCs display greatly diverse morphologies at all investigated ages.

(A): Maximum intensity projection of a P10 OPC (left) and corresponding tracing (right). A young, very flat OPC with clearly distinct processes of mostly similar length. Each process is labeled with a different colour. Soma outline is in purple. (B): Similar to (A), a P10 OPC and corresponding tracing. In contrast to (A), this young OPC has 3 large, massive processes (green, orange, red) and multiple much shorter ones. (C): Similar to (A), a P20 OPC and corresponding tracing. Please note a remarkable change in the length of processes when compared with both P10 cells. This cell has multiple processes of comparable length which frequently intermingle. Soma outline in yellow. (D): Similar to (C), a P20 OPC and corresponding tracing. Please note irregular shape of the soma and the lack of bipolar morphology with an unusual asymmetry of process distribution. This cell has only 3 large processes (violet, pink, orange) but localized only at the top-right side from the soma. The left-bottom side has only short processes. Soma outline in orange. (E): Similar to (A), a P50 OPC and corresponding tracing. The cell does not have bipolar morphology (although soma is oval and regular) and seems to be selective towards the direction of it's processes, as in (D). In addition, clear gaps in the process coverage of the surrounding brain parenchyma are visible. Soma outline in pink. (F): Similar to (E), a P50 OPC and corresponding tracing. This cell has processes strongly aligned with callosal axons. Soma outline in pink.

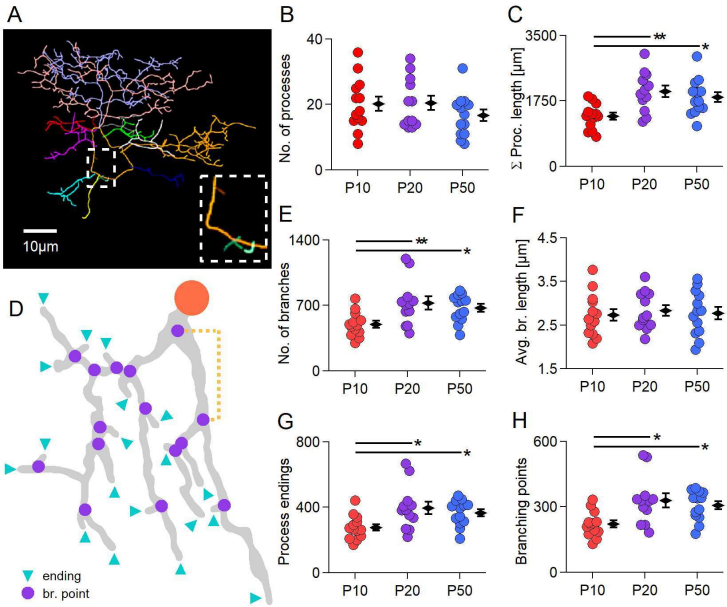

Figure 25. During development OPCs increase the size but not the number of processes, with a complimentary increase in the number of branches, br. points and endings.

(A): An example of an OPC without a bipolar morphology. Each process is labeled with a different color. Note the large diversity in process length and branching and the uneven space filling of the processes. The inset shows 3 tiny filopodial processes; larger processes were removed from the inset for clarity. (B): Comparison of the total number of processes per

cell. All processes in an individual cell were counted regardless of their length or branching. Each circle represents the count in one cell. Black diamonds represent group average ± SEM. Statistically significant differences are highlighted by horizontal bars, *=p<0.05, **=p<0.01. P10 group: n=13 in 7 animals; P20 group: n=12 in 8 animals; P50 group: n=13 in 8 animals. The same labeling and n,N numbers apply to other graphs in this figure. (C): Total length of all processes within each cell, compared between age groups. (D): Schematic drawing of a single process. The origin of the soma is represented by a large red circle. Small violet circles represent branching points of the process. Blue triangles point towards process endings. A branch is a part of the process between a branching point and another branching point or an ending. An example of a branch is marked by an orange semi-box. (E): Total number of branches within each cell, compared between age groups. Branches are counted regardless of process length or branching. (F): Average length of a single branch per cell, compared between groups. (G): Total number of endings in each cell, compared between groups. (H): Total number of branching points in each cell, compared between groups. (I): The ratio of bifurcations among all branching points, compared between groups.

Intriguingly, the average length of branches remained very similar [**Fig 25F**; 2.729 ± 0.136 at P10; 2.832 ± 0.124 at P20; 2.775 ± 0.142; P10 vs P20 p=0.934; P10 vs P50 p=0.946; P20 vs P50 p=0.946]. Moreover, the ratio of bifurcations among the br. points remains equally stable [0.853% ± 0.93 at P10; 0.873% ± 0.85 at P20; 0.872% ± 0.54 at P50; one-way ANOVA p=0.152], suggesting that the branching pattern might be developmentally preserved.

4.10 During callosal development OPCs increase in size but maintain comparable process density within their domain

In the previous section we described the general morphology of OPCs but without investigating how the processes fill the cell domain and we suggested preservation of branching pattern. To test this, we used Sholl analysis which is a well-established technique to compare branching and the distribution of processes (Sholl, 1953).

For this analysis we drew a set of concentric shells spanning over the whole volume occupied by each OPC, with the center of each shell located at the centroid of the soma. The spacing between the shells was set to 2.5µm [**Fig. 26A**, also see Materials and Methods] to roughly match the average branch lengths [**Fig. 25F**]. In the classical analysis the number of intersections between the process skeletons (single-pixel approximations preserving lengths but ignoring local thickness) is used to evaluate how the structure changes with increasing distance from the soma [**Fig. 26A**]. The shells partition the brain parenchyma into volume compartments, allowing quantification of branching points or endings as well as lengths of branches caught within a compartment [**Fig. 26B**]. The method, however, has certain assumptions and limitations: First, while the measurement is fully 3-Dimensional, it assumes that the process expansion in all possible directions is equally likely, therefore functional or micro-environment driven asymmetries, changes in cell polarity or gaps within the cell domain (such as processes avoiding blood vessels or being selective towards a direction) are ignored. In addition,

all differences in the structure, length or volume of individual processes are also ignored. Finally, the order in which the processes branch is also ignored.

First, we looked into the number of intersections plotted against the distance from the soma [**Fig. 26C**]. We found that up to the distance of ~17.5 µm from the center of cell soma the number of intersections was similar between the age groups [**Fig. 26C**; one-way ANOVA p=0.111-0.808]. Furthermore, in all of the groups the intersections reached the peaked at the distance of ~15 ± 2.5 µm and declined thereafter [**Fig. 26C**; 39.154 ± 2.275 at P10; 52.167 ± 6.882 at P20; 44.769 ± 5.876 at P50; one-way ANOVA p=0.268]. The first significant differences between groups were visible at the distance of ~20 µm, where the number of intersections in the P10 group declined rapidly, while remaining stable for both P20 and P50 cells [**Fig. 26C**; 26.539 ± 3.010 at P10; 52.500 ± 5.373 at P20; 43.615 ± 4.509 at P50; P10 vs P20, p=0.000543; P10 vs P50, p=0.0160; P20 vs P50, p=0.161]. Afterwards, within the next 5 µm both P20 and P50 OPCs also showed a fast progressing decline. The P50 cells remained significantly different from the P10 cells almost throughout the whole remaining distance range, up to the last detected intersections ~55 µm. On the other hand, P20 cells were different from P10 only throughout the distance of ~20-30 µm. Afterwards the P20 distribution remained statistically similar to P10, but became different from P50 [**Fig. 26C**], suggesting that P50 cells are more elongated.

Next, we looked into the process lenghts and the number of br. points and endings in the volumetric compartments generated by Sholl shells [**Fig. 26B**]. All of the distributions closely followed the distribution of intersections [**Fig. 26D-F**], peaked at the distance of ~15 ± 2.5 µm (17.5 ± 2.5 µm for endings, **Fig. 26F**) and tested as different throughout the same distance ranges. Moreover, the overall shape of the distributions were comparable. Branch lengths at peak [**Fig. 26D**]: 180.854 ± 11.897 at P10; 241.158 ± 32.382 at P20 (but note the high variability); 189.031 ± 22.039 at P50; P10 vs P20 p=0.209; P10 vs P50 p=0.801; P20 vs P50 p=0.229. No. of br. points at peak [**Fig. 26E**]: 30.923 ± 2.908 at P10; 39.583 ± 5.226 at P20; 31.923 ± 3.529 at P50; P10 vs P20 p=0.345; P10 vs P50 p=0.857; P20 vs P50 p=0.345. No. of endings [**Fig. 26F**]: 35.3077 ± 3.46111 at P10; 43.9167 ± 5.79637 at P20; 32.2308 ± 3.29560 at P50; P10 vs P20 p=0.301; P10 vs P50 p=0.607; P20 vs P50 p=0.174.

4.11 The order of branches on a process is developmentally preserved

As we pointed in the previous section (**4.10**) Sholl analysis ignores the structure and the position of branches of a process by focusing only on the distribution in space. Therefore, we decided to investigate whether the order of branches, or their number and length related to the order, change during development. The assumptions during the analysis are almost the opposite of Sholl's: the loca-

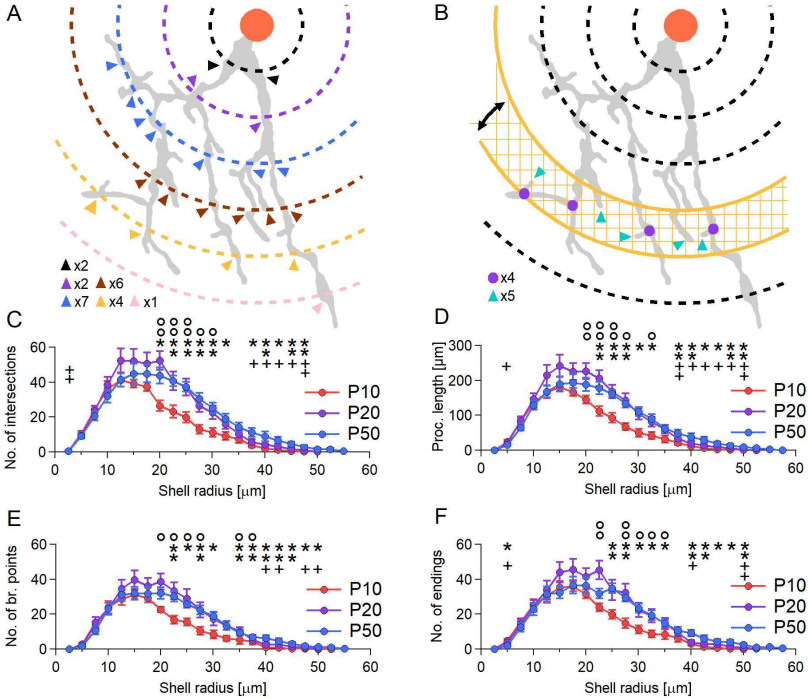

Figure 26. During development OPCs preserve the process density within the inner part of the cell domain but increase the density in its outer reaches.

(A): Example of Sholl analysis: a set of concentric shells (represented in 2D as circles), spaced every 2.5µm, is positioned over the centroid of a soma. Then, the number of intersections between the process and each of the shells is counted and plotted against the shell's distance from the soma (radius). In the example each consecutive shell has a different color. Arrowheads point to intersections with the specific shell. Bottom left: a summary of the number of intersections of the process with each shell. (B): The shells partition brain parenchyma into volumetric compartments and allow the measurement of structure lengths and/or the number of sub-structural elements contained within the shells. In the example arrows show a shell spun between 2 shells (in orange) singled for the analysis. The length of the process, the number of branching points or endings contained in the checked area (volume) is then measured and plotted against the upper radius of the shell range (i.e.: 30µm = 27.5µm to 30µm). (C): Comparison of the number of intersections with shells spaced every 2.5µm. All points on the graph represent group averages ± SEM; P10 in red, P20 in green, P50 in blue. Significant differences are marked with ° for P10 vs P20 comparisons; * for P10 vs P50 comparisons; ⁺ for P20 vs P50 comparisons. °,*,⁺ = p<0.05; °°,**,⁺⁺ = p<0.01. P10 group: n=13 in 7 animals; P20 group: n=12 in 8 animals; P50 group: n=13 in 8 animals. (D): Comparison of the length of

processes within shells spaced every 2.5µm. Data is plotted against the upper radius of the shell range (i.e.: 30µm = 27.5µm to 30µm). The labeling, n numbers and plotting radius are identical to (C). (E): The same as (D) for the number of branching points within shells. The labeling, n numbers and plotting radius are identical to (C). (F): The same as (D) for the number of endings within shells. The labeling, n numbers and plotting radius are identical to (C).

-tion in space is ignored and only the position on the process is treated as relevant, the directions of the branches are ignored as well. However, with the method we can trace the lengths and numbers of the new "building blocks" as they are appearing on the process. We used centrifugal ordering paradigm (see Materials and Methods).

First we looked into the number of branches per order. The P10 peaked at branch order 6 [**Fig. 27C**; 48.846 ± 2.396], after which the P10 group distribution declined. The P20 and P50 distributions peaked a little later, at order 7 [**Fig. 27C**; 59.917 ± 5.610 at P20; 59.077 ± 5.454]. After order 7 both distributions started to decline. Afterwards, the P20 an P50 distributions became indistinguishable from each other [**Fig. 27C**; p=0.067 to p=0.999], and continued to decline at a similar rate. The statistical differences first appeared at order 9, where the P10 group tested as different from both P20 and P50 [**Fig. 27C**; 38.6154 ± 2.68791 at P10; 54.1667 ± 5.93377 at P20; 55.3846 ± 4.45999; P10 vs P20 p=0.0395; P10 vs P50 p=0.0327; P20 vs P50 p=0.850]. Interestingly, the slope of the decline remained very comparable between the groups.

As the next step, we sought to investigate whether there might be any possible changes in the branching pattern. We looked into the ratio of bifurcations among the br. points (as in **4.9**), plotting it against br. order. We found that throughout development the ratios remained very conservative, starting ~0.85 at order 1 [**Fig. 27D**; 0.801 ± 0.0338 at P10; 0.864 ± 0.0353 at P20; 0.880 ± 0.0231 at P50] and continuing to ~0.90 [0.913 ± 0.0278 at P10; 0.893 ± 0.0271 at P20; 0.904 ± 0.0218 at P50] at order 13, where the measurements become unreliable due to very low branch numbers. The distributions were not significantly different at any point [p=0.0570 to p=0.898]. There is a small but insignificant [**Fig. 27D**; order 1 vs order 13; at P10 p=0.0717; at P20 p=0.329; at P50 p=0.255] increase in the ratio of bifurcations with ascending orders but between the groups the distributions are almost indistinguishable [p=0.0570 to 0.898].

Next we investigated whether there is any distinguishable pattern in the lengths of branches. We did not find differences in the average branch lengths. The longest branches can be found at the very beginning of the process, slowly decreasing in length with each new br. point. The order 1 branches start at ~3.3 µm (on average) [**Fig. 27E**; 3.081 ± 0.176 at P10; 3.467 ± 0.270 at P20; 3.300 ± 0.228] while the final ones at order 13 are almost 30% shorter [2.182 ± 0.188 at P10; 2.471 ± 0.111 at P20; 2.504 ± 0.172 at P50].

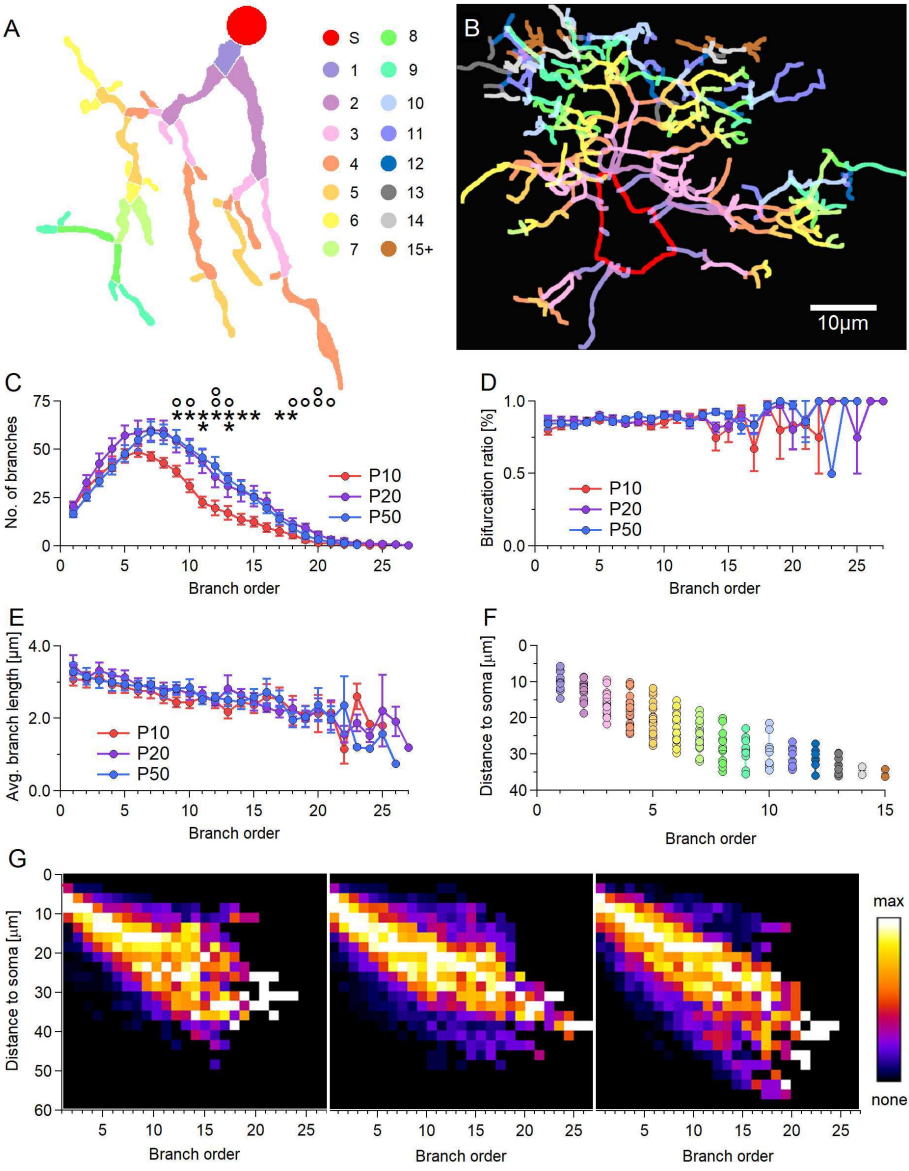
A
S
1
2
3
4
5
6
7
8
9
10
11
12
13
14
15+
B
10µm
C
No. of branches
Branch order
P10
P20
P50
D
Bifurcation ratio [%]
Branch order
P10
P20
P50
E
Avg. branch length [µm]
Branch order
P10
P20
P50
F
Distance to soma [µm]
Branch order
G
Distance to soma [µm]
Branch order
Branch order
Branch order
max
none

Figure 27. The number of process branches changes but their properties are preserved during development.
(A): Single process with each branch colored in accordance to its position on the process (branch order). The color code used in this figure, figure (B) and (F) is the same and is shown to the right of the process. Soma is labeled in red. (B): Reconstruction of a whole OPC with each branch colored in accordance with its position on the process. (C): Comparison of the number of branches at each branch order. All points on the graph represent group averages ± SEM. Significant differences are marked with ° for P10 vs P20 comparisons; * for P10 vs P50 comparisons. °,* = $p<0.05$; °°,** = $p<0.01$. There were no significant differences between P20 and P50 groups. P10 group: n=13, N=7; P20 group: n=12, N=8; P50 group: n=13, N=8 animals. The same labeling, n and N numbers apply to other graphs in this figure. (D): Comparison of the fraction of bifurcations at each branch position. (E): The average length of a single branch at each branch position. (F): Relationship between position on the process and branch's distance from cell soma. Branches from the cell shown in (B) are separated by their order and plotted against distance between their origin point and the centroid of the soma. All branches of order 15 and higher are plotted together as 1 category. Black bar shows the median. (G): Comparison of the relationship between branch position and distance from the soma. At each order the branch distance to soma is binned into 2.5μm categories generating a histogram. Those histograms are plotted in an ascending order with the peak of the histogram colored white, zeroes colored black.

Finally, we combined this analysis with Sholl analysis to visualize where the branches of ascending orders can be found. We calculated the straight line distance of each br. point to the centroid of the soma of the cell and plotted those distances against the points' order. The plot in **Fig. 27F** shows this being done for the cell in **Fig. 27B**, with the same color code. The distributions were very comparable across the age groups, showing an almost linear relationship between the order and the distance from the soma [**Fig. 27G**]. As expected, high-order branches of P20 and P50 OPCs were located at the outer parts of the cell domain [**Fig. 27G**]. The P50 group seems to have the highest variability in the location of the branches of orders 13+, consistent with their higher number of intersections at the furthest Sholl radii. Interestingly, based on the results it seems unlikely that the branches trace backwards towards the soma, explaining the lack of higher-order branches in the soma proximity. It appears that the branches of large processes tend to face outwards and sideways with smaller processes or the early branches occupying the perisomatic space.

4.12 OPC processes show preferential alignment with the lateral-medial anatomical axis and avoid aligning with the dorsal-ventral direction

During development corpus callosum continues to grow but the volume gain is not uniform. The changes in callosal growth likely influence OPC morphology therefore we investigated whether there is any preference in the alignment of branches with anatomical axes. The most common way of describing directions in 3D is by utilizing the spherical coordinate system where the direction is given by two angles: a polar angle φ defined for x,y plane and an azimuth angle θ corresponding to z axis, perpendicular to both x and y (see Materials and Methods, **3.18**).

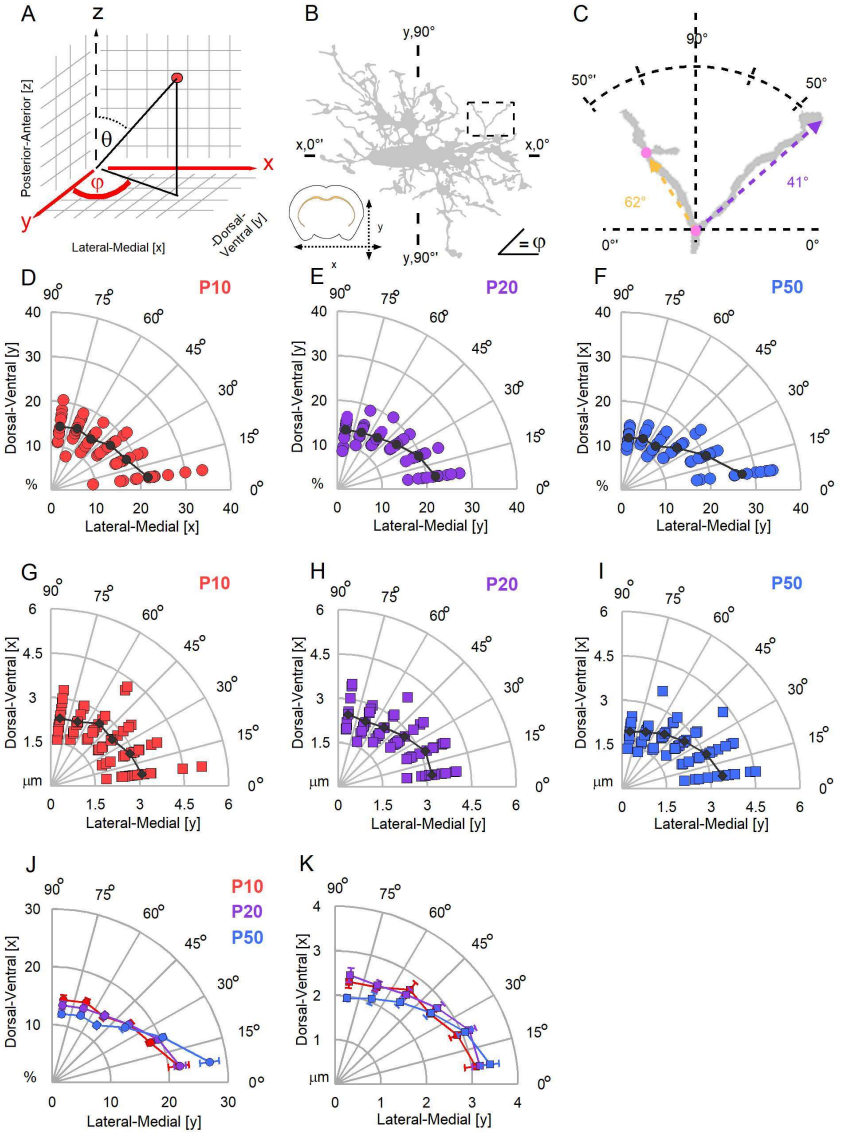
A
z
θ
φ
x
y
Posterior-Anterior [z]
Lateral-Medial [x]
Dorsal-Ventral [y]
B
y,90°
x,0°
x,0°
y,90°
= φ
C
90°
50°
50°
62°
41°
0°
0°
D
P10
E
P20
F
P50
Dorsal-Ventral [y]
Lateral-Medial [x]
Lateral-Medial [y]
G
P10
H
P20
I
P50
Dorsal-Ventral [x]
µm
J
P10
P20
P50
K

Figure 28. OPC processes preferentially align with and have longer branches when facing the medial-lateral over the dorsal-ventral body axis.

(A): Medial-lateral and dorsal-ventral axes mapped onto a spherical coordinate system correspond to the x and y axes (colored red) and the planar angle φ between those axes. Please note that the elevation angle θ is ignored in this analysis. (B): Example of a cell in the coronal view with angular values of φ added. Perfect alignment with the medial-lateral axis occurs when the value of φ=0°. Perfect alignment with the dorsal-ventral axis occurs when the value of φ=90°. (C): Inset from (B), enlarged part of the process with the φ values for 2 different branches. The direction of a branch is approximated by the direction of a vector spun between the beginning and the termination of the branch. Tortuosity of the branch is ignored. The Color of the vector corresponds to the color of the φ measurement. (D): Distribution of branches in alignment with medial-lateral or dorsal-ventral axes in the P10 age group. φ values are binned every 15° and plotted as a fraction (%) of all φ values measured per cell. Each red circle represents a % of φ values per 15° category in an individual cell. Black circle represents the group average, n=13, N=7 animals. (E): The same as (D) for the P20 age group, n=12, N=8 animals. (F): The same as (E) for the P50 age group. n=13, N=8 animals. (G): The average length of branches in alignment with medial-lateral or dorsal-ventral axes in the P10 age group. φ values are binned every 15° and branch lengths within each category are averaged. Each red circle represents the length of branches within a 15° category, measured in an individual cell. Black circle represents the group average, n=13, N=7 animals. (H): Similar to (G) for the P20 group, n=12, N=8 animals. (I): Similar to (G) for the P50 group, n=13, N=8 animals. (J): Summary of % of branches in alignment with medial-lateral or dorsal-ventral axes in all age groups. P10 in red, P20 in purple, P50 in blue. Each circle represents the group average ± SEM. Binning and fractions are identical to (D) – (E). (K): Summary of the lengths of branches in alignment with medial-lateral or dorsal-ventral axes in all age groups. P10 in red, P20 in purple, P50 in blue. Each circle represents the group average ± SEM. Binning and fractions are identical to (G) – (I).

First we investigated how many branches faced lateral-medial axis and dorsal-ventral axis [**Fig. 28A-C**]. The values were normalized to the total number of branches in each cell and averaged for the group. In all investigated ages, the largest number of branches was closely aligned with the lateral-medial axis (0°-15°). The P10 and P20 had comparable distributions, both with significantly less branches than P50 OPCs [**Fig. 28D-F, J**; 21.7065 ± 1.753% at P10; 21.9833 ± 0.985% at P20; 27.0575 ± 1.618% at P50; P10 vs P20 p=0.899; P10 vs P50 p=0.0472; P20 vs P50 p=0.0482]. The more the branches misaligned with lateral-medial axis the lower was their number, reaching a minimum for branches aligned with dorsal-ventral axis (75°-90°). P50 OPCs had the lowest number of branches with dorsal-ventral axis alignment but only significantly different from P10 cells [**Fig. 28D-F, J**; 14.3698 ± 0.838% at P10; 13.4630 ± 0.712% at P20; 11.8987 ± 0.454% at P50; P10 vs P20 p=0.360; P10 vs P50 p=0.0421; P0 vs P50 p=0.223].

Next, we investigated whether different process alignment has any influence on the lengths of the branches. Contrary to the counts, we found no statistical differences in branch lengths, except for branches closely aligned with the dorsal-ventral axis (75°-90°) where P50 cells had significantly shorter branches when compared with the P20 cells [**Fig. 28G-I, K**; 2.360 ± 0.0959μm at P10; 2.403 ±

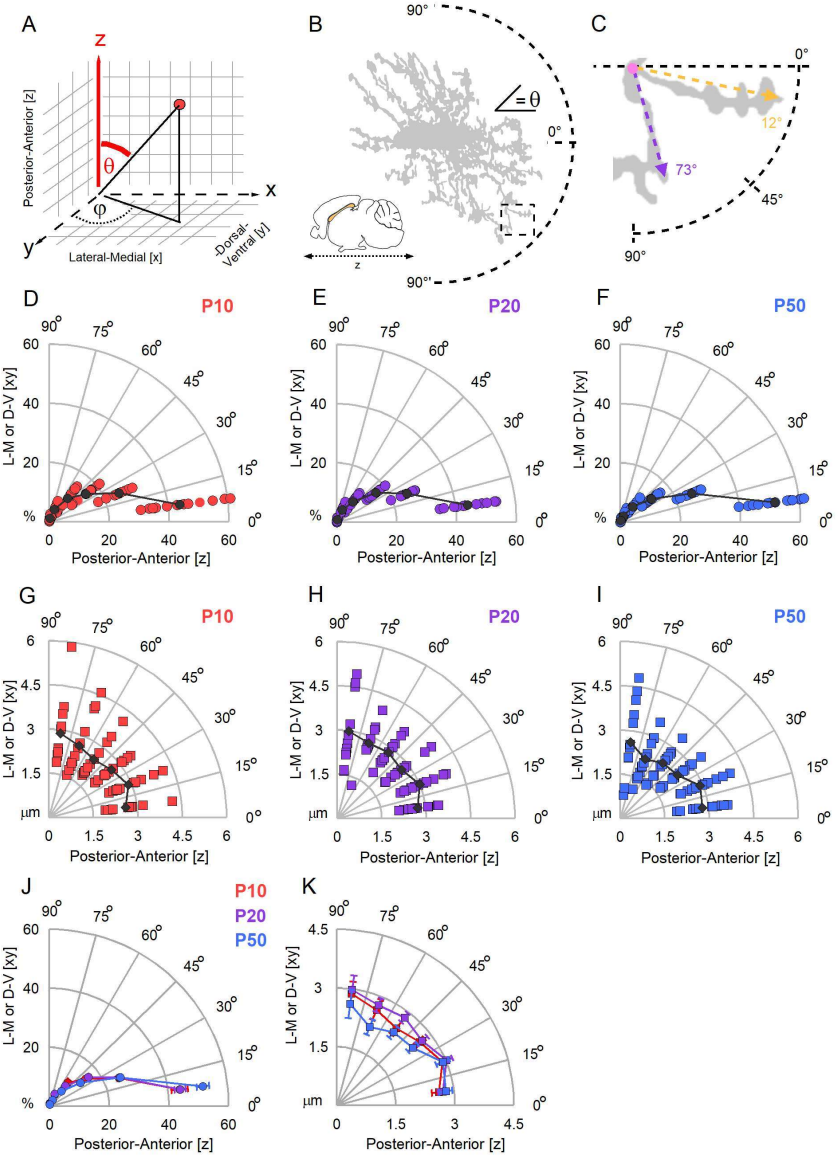
A
z
θ
x
φ
y
Posterior-Anterior [z]
Lateral-Medial [x]
Dorsal-Ventral [y]
B
90°
= θ
0°
90°
z
C
0°
12°
73°
45°
90°
D
P10
E
P20
F
P50
L-M or D-V [xy]
Posterior-Anterior [z]
G
P10
H
P20
I
P50
µm
J
P10
P20
P50
K

Figure 29. OPCs show preference for but no change in branch length while facing the anterior-posterior body axis. (A): Anterior-posterior axis mapped onto a spherical coordinate system corresponds to the z axis (colored red) and the elevation angle θ. Please note that the planar angle φ is ignored in the analysis. (B): Example of a cell in a sagittal view with angular values of θ added. Perfect alignment with the anterior-posterior axis occurs when the value of θ=0°. The inset is enlarged in C. (C): Inset from (B), enlarged part of the process with the θ values for 2 different branches. The direction of a branch is approximated by the direction of a vector spun between the beginning and the termination of the branch. Tortuosity of the branch is ignored. The color of the vector corresponds to the color of θ measurement. (D): Distribution of branches in alignment with anterior-posterior axis in the P10 age group. θ values are binned every 15° and plotted as a fraction (%) of all θ values measured per cell. Each red circle represents a % of θ values per 15° category in an individual cell. Black marker represents the group average, n=13, N=7. (E): Similar to (D) for the P20 age group, n=12, N=8. (F): Similar to (D) for the P50 age group, n=13, N=8. (G): The average length of branches in alignment with the anterior-posterior axis in the P10 age group. θ values are binned every 15° and branch lengths within each category are averaged. Each red circle represents the length of branches within a 15° category, measured in an individual cell. Black circle represents the group average. (H): Similar to (G) for the P20 age group, n=12, N=8. (I): Similar to (G) for the P50 group, n=13, N=8. J): Summary of % of branches in alignment with anterior-posterior axis in all age groups. P10 in red, P20 in purple, P50 in blue. Each circle represents the group average ± SEM. Binning and fractions are identical to (D) – (E). (K): Summary of the lengths of branches in alignment with anterior-posterior axis in all age groups. P10 in red, P20 in purple, P50 in blue. Each circle represents the group average ± SEM. Binning and fractions are identical to (G) – (I).

0.118μm at P20; 1.961 ± 0.0786μm at P50; P10 vs P20 p=0.761; P10 vs P50 p=0.0138; P20 vs P50 p=0.0110]. We investigated this phenomenon further by calculating a ratio of lengths for dorsal-ventral aligned versus medial-lateral aligned branches. Ratios for P10 and P20 OPCs were nearly identical, 0.794 ± 0.069; 0.791 ± 0.052 respectively, and not statistically different (p=0.999). However, P50 cells (0.587 ± 0.026), were significantly different from both P10 and P20 cells (P10 vs P50 p=0.0219; P20 vs P50 p=, indicating a much stronger elongation/shortening of branches.

4.13 OPC processes show preferential alignment with the posterior-anterior body axis

Next we replicated the analysis for the azimuth angle θ. For the θ angle branches at 0° align with the posterior-anterior axis while 90° is used for branches which miss-align with the axis (regardless of their x-y alignment) [**Fig. 29A-C**].

First, we investigated how many branches aligned with the posterior-anterior axis. The overwhelming majority majority of branches aligned with the anterior-posterior axis in all groups. P50 OPCs had significantly more anterior-posterior aligned branches than P10 or P20 cells [**Fig. 29D-F, J**; 43.913 ± 2.787 at P10; 44.070 ± 1.863 at P20; 51.774 ± 2.159 at P50; P10 vs P20 p=0.761; P10 vs P50 p=0.0138; P20 vs p50 p=0.0110]. However, when we investigated the average lengths of the

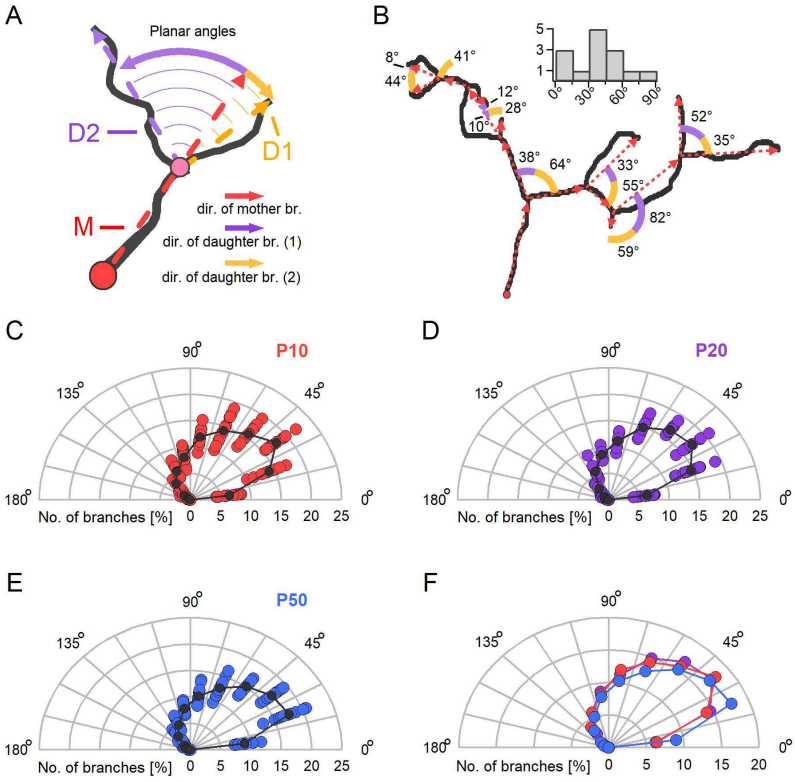

Figure 30. The majority of new branches show a direction preference which is preserved during development.
(A): Example of planar angle measurement to estimate the change in branch direction. The change of direction is measured at a branching point (pink circle) as an angle between the direction vector of the mother branch (M, red) and the direction vectors of its daughter branches (D1, orange; D2, violet). The angle measurements are indicated by colored arc arrows, color corresponding to respective daughter branches. (B): Example of a complex process with the changes to branch direction measured for every branch. Similar to (A), angular measurements for the first daughter branch are colored orange and for the complementary daughter branch in violet. Direction vectors for each branch are in red. The planar angle measurements for the example, binned every 15°, from 0° to 90°, are summarized in a histogram above the graph. (C): Distribution of the planar angle values measured in the P10 age group. Measurements are binned every 15°, with 0° indicating no change in branch direction and 180° indicates complete reversion in direction. Each red circle represents a % of angular values per 15° category in an individual cell. Black circle represents the group average, n=13, N=8 (D): Similar to (C) for the P20 age group, n=12, N=8. (E): Similar to (C) for the P50 age group, n=13, N=8. (F): Summary of (C) – (E) with group averages plotted together.

branches we found no significant differences between the groups [**Fig. 29G-I, K**; P10 vs P20 p=0.458 to 0.978; P10 vs P50].

4.14 The change in the direction of successive branches is developmentally preserved

OPCs have a highly ramified morphology, closely resembling morphology of neuronal dendrites. Dendrites branch extensively to reach their synaptic targets but usually display a preferred angle while branching (Cherniak, 1992; Rojo et al., 2016; Leguey et al., 2016). Therefore as our next step, we compared changes in the direction between successive branches by measuring the planar angle between pairs of branches sharing the same br. point [**Fig. 30A, B**]. In the analysis 0° indicates no change in the direction while 180° indicates complete reversion in direction.

Interestingly, we found that in both P10 and P20 cells the largest number of branches ~17% changed the direction by 30°-45° [**Fig. 30C-F**; 17.765 ± 0.535% at P10; 17.047 ± 0.538% at P20], followed closely by ~16% at 45°-60° [15.900 ± 0.515% at P10; 16.508 ± 0.300% at P20] and ~14% at 15°-30° [14.096 ± 0.533% at P10; 14.678 ± 0.576% at P20]. Few branches, ~6%, [6.378 ± 0.392% at P10; 6.186 ± 0.312% at P20] changed their direction by less than 15°. After the peak the number of branches facing broader angles progressively declined. There was very little difference between P10 and P20 cells regarding those values [**Fig. 30C-F**; 0°-120°, p=0.268 to 0.674]. However, the angles in P50 OPCs were slightly smaller. The largest number of branches, ~17.5%, changed the direction by 15°-30° [17.283 ± 0.649], followed by ~17% branches changing direction by 30°-45° [17.164 ± 0.393]. ~9% of angles were less than 15° [8.834 ± 0.378%]. This trend tested as significant at 0°-30° for P10 and P50 groups [p=0.0000554 to 0.00133] and remained significant till 75° between P20 and P50 [p=0.0000365 to 0.0368].

4.15 Change in the direction of branches is similar at all branch orders

Finally, we tested whether the change of directions is related to branch order. We measured the planar angle for all branches of each successive order [**Fig. 31A**]. Surprisingly, we found no consistent significant differences in the angle medians, neither within nor between groups, suggesting that OPCs preserve their branching pattern irrespective of the br. point position [**Fig. 31B-D**]. Interestingly, there seems to be a very minor increase in the planar angles with successive orders in the P10, and to a lesser extend P20 groups, but it is also not significant. P50 group does not seem to have this trend.

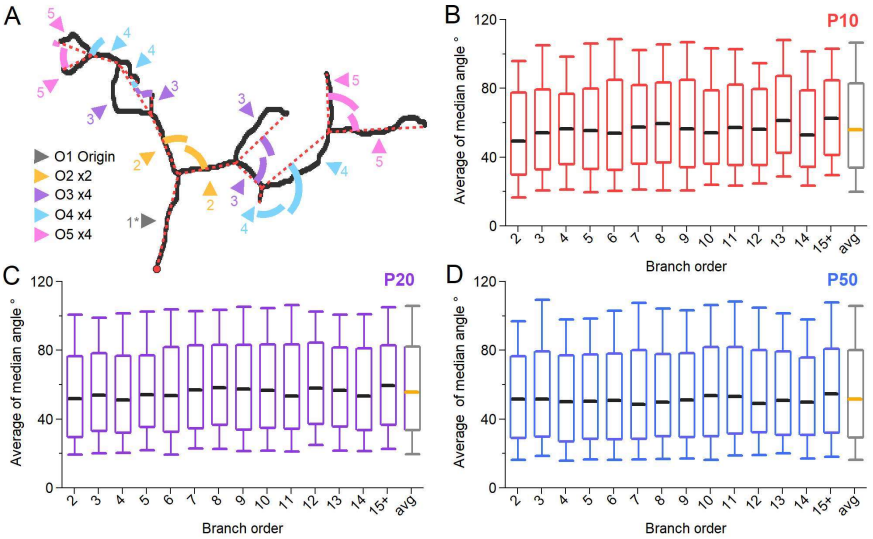

Figure 31. Changes in branch direction are not dependent on the position within a process (branch order) and do not change during development.

(A): Example of a complex process with the changes to branch direction measured for every branch color coded by branch order: order 1 in gray, order 2 in orange, order 3 in violet, order 4 in turquoise, order 5 in pink. Arrowheads point towards the branch for which the angle is measured and are colored based on the branch order. (B): Box plots summarizing the change in direction at increasing branch orders in the P10 age group. Each red box represents the 25th to 75th percentile, whiskers represent the 10th and 90th percentile and the black bar is median. Grey box plot represents the average among all orders, with the median in orange, n=13, N=7. (C): Similar to (B) in the P20 age group, n=12, N=8. (D): Similar to (B) in the P50 age group, n=13, N=8.

5. Discussion

During the period between P5 and P9, when callosal axons are growing into cortical layers and beginning to form arbors, pre-synaptic neuronal activity is crucial for the proper formation of their projections. Synapses with callosal OPCs are likely formed at this time, followed by an increasing wave of myelination starting 2-3 days later [**Fig. 32**].

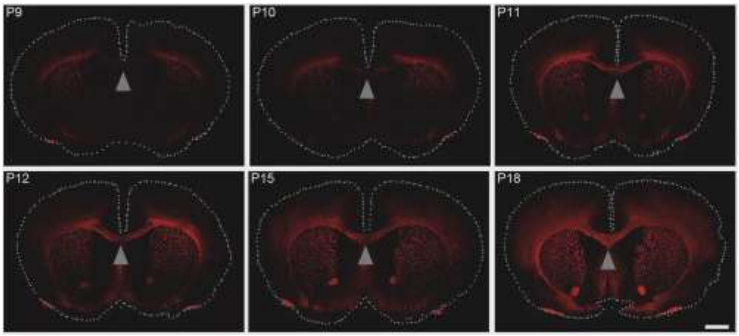

Figure 32. Myelination of corpus callosum during postnatal development. In red: MBP immunolabeling. Arrowheads indicate the center of corpus callosum. Adapted from: Chen et al., 2018.

5.1 Dendrite/process morphology is critical for synaptic signal integration

The electrical impact of small synaptic currents in OPCs is mainly determined by their passive electrical properties. In neurons, the extent of dendritic filtering of synaptic potentials is influenced by the overall structure of the dendritic tree, the membrane characteristics of the dendrites, and the location of the synapses. In most neurons, dendrites have a powerful effect on filtering synaptic potentials as they spread through them. Consequently, the potentials that are recorded at the soma are much smaller than the same events that are recorded in the dendrites. There are two factors that impact the difference between EPSPs recorded in dendrites versus those recorded in the soma. The first is related to the dendritic structure, which includes a relatively low density of charged particles in the cytoplasm that creates a significant longitudinal resistance. As a result, some current will follow alternate paths, such as the dendritic membrane capacitance and its resistance. Due to the significant number of dendritic branches and surface area in most dendritic trees, synaptic current is substantially lessened as it moves into dendritic branches en route to the soma. During callosal development we have seen a substantial, almost 11-fold, reduction in R_m (P10 vs P50), coupled with a 30-40% increase

in C_m [**Fig. 18**] indicating an expansion of the process structure (further confirmed by morphological analysis [**Fig. 25**; **Fig. 26**]), which are likely to cause a prominent reduction in synaptic signals reaching the soma. This effect of increased passive signal filtration in OPC processes could explain why the quantal EPSCs reported in **Fig. 16** remain comparable throughout callosal development, in spite of increased Ca^{2+} permeability and larger conductance (**Fig. 16**; **Fig. 17**, respectively), which should increase the magnitude of AMPAR signals (Greger et al., 2017; Zonouzi et al., 2011)

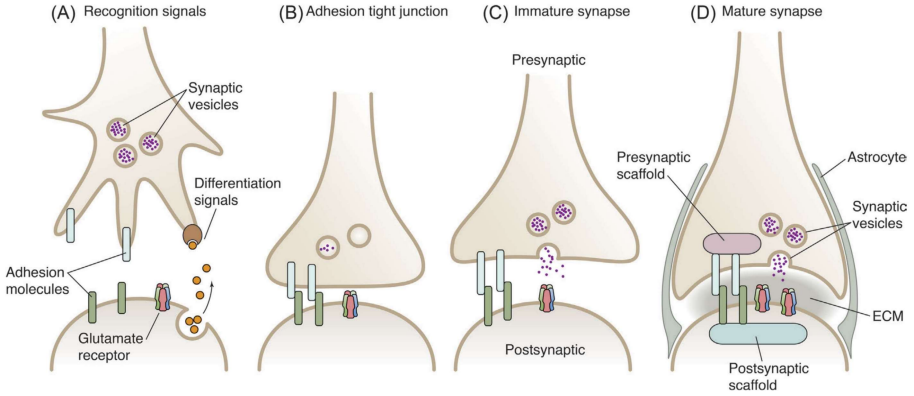

Figure 33. Stages of neuronal synapse formation. (A) Growth cone filopodia recognize and come into contact with a suitable postsynaptic target. (B) Growth cone filopodia retract allowing tight apposition of membranes through cell adhesion proteins. (C) The immature synapse has few presynaptic vesicles and postsynaptic density is small. (D) A mature synapse with dense extracellular matrix, large vesicle pool and pre- and postsynaptic scaffold. Often astrocyte processes envelop the synapse. Adapted from Sanes et al., 2019.

Repetitive synaptic input, as occuring during trains of presynaptic action potentials [**Fig. 19**; **Fig. 21**; **Fig. 22**], leads to cumulative synaptic depolarization of OPCs. Jabs et al. (2005) proposed that this depolarization may be substantial and reach the reversal potentials of synaptic neurotransmitter receptors. Moreover, during patch-clamp recordings, in line with our report, prominent outward currents in the range of several nA are observed upon depolarizing voltage steps to approximately −40 mV. Thus, it is clear that the voltage response of OPCs to synchronous activity of presynaptic neurons will not only be determined by the passive membrane properties but will likely be significantly modulated by voltage-activated ion channels. The recruitment of voltage-gated channels in OPCs by

synaptic input has not yet been experimentally addressed. Nevertheless, existing voltage-clamp data allow us to outline possible scenarios about electrical synaptic integration in OPCs.

5.2 Integration of synaptic input in OPC processes

The electrical integration of synaptic input in OPCs is likely to be modulated by three families of ion channels due to their pronounced amplitude. These families include A-type K^+ channels, delayed-rectifier (DR-type) K^+ channels, and fast voltage-activated Na^+ channels (Steinhauser et al., 1994b; Kressin et al., 1995; Yuan et al., 2002; Chittajallu et al., 2004; Jabs et al., 2005; Xie et al., 2007; De Biase et al., 2010; Kukley et al., 2010). Although voltage-activated Ca^{2+} channels and persistent sodium channels have also been identified in OPCs, their direct effect on synaptic potentials is likely small due to their low amplitude ranges (below 50 pA recorded in the soma at physiological ion concentrations), their contribution to local signal enhancement within process branches might be substantial (Akopian et al., 1996; Tong et al., 2009; Haberlandt et al., 2011).

The amplitudes of A-type, DR-type, and sodium channels are large enough to outcompete the maximal synaptic current amplitudes, indicating that these channels are well-suited to strongly modulate or abolish synaptic depolarizations. However, whether synaptic potentials recruit voltage-gated channels also depends on the gating kinetics and voltage range of activation of the channels. We provided a detailed analysis of these parameters throughout callosal development [**Fig. 18**]. We found that A-type K^+ channels are activated around membrane potential of -40 mV, rapidly open with a time constant of 0.5-1.5 ms, and deactivate with a time constant of 10-20 ms. In contrast, DR-type K^+ channels slowly activate with a time constant of approximately 10 ms when the membrane potential is depolarized above -20 mV and hardly inactivate. Finally, Na_v channels open very fast, in less than 0.5 ms, and also inactivate with a time constant around 2 ms. Notably, the activation threshold for Nav channels is -40 mV, similar to the threshold of A-type potassium channels. However, the relationship between these kinetic parameters and voltage ranges and their effect on synaptic input remains to be explored (Steinhauser et al., 1994b, Sun and Dietrich 2013).

After analyzing the gating properties of DR-type channels and the kinetics and amplitudes of synaptic conductance changes, it appears that glutamatergic synaptic potentials are unlikely to recruit large numbers of DR-type K^+ channels due to their slow activation. Conversely, A-type K^+ channels activate quickly enough to modulate synaptic potentials in neurons (Hoffman et al, 1997), which suggests that glutamatergic synaptic potentials triggered in response to synchronous action potentials in multiple presynaptic terminals may be reduced in amplitude or shortened by enhanced repolarization through A-type channels. This modulation may be frequency-dependent for repetitive release events because A-type potassium channels rapidly inactivate. Therefore this modulation is

unsustainable at higher frequencies, which could allow A-type channels to function as an input frequency detector (Sun and Dietrich, 2013).

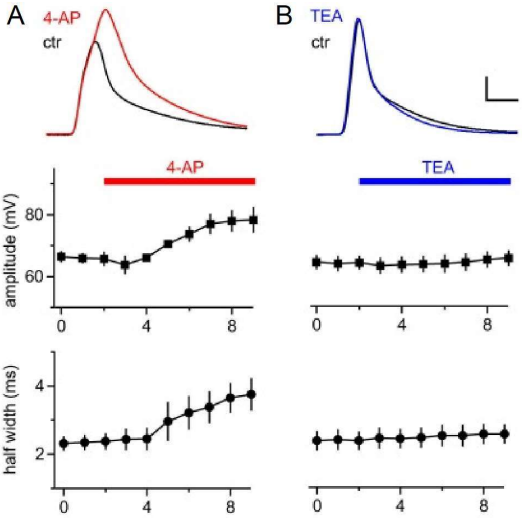

Figure 34. A-type K+ channels shorten mock PSPs in OPCs. (A) Blocking A-type K+ channels with 4 mM 4-AP strongly broadens and increases amplitudes of mock PSPs. (B) Application of 10 mM TEA to block delayed-rectifier K+ channels does not have effects on the mock PSPs. Scale bars: 15 mV, 3 ms. (C) Time-course of the average amplitude and half width of the mock PSPs during application of 4-AP and TEA. Adapted from Sun et al., 2016.

Once a neuron's membrane potential surpasses a specific threshold, action potentials and/or rapid spike-like depolarizations are initiated by fast Na_v channels. Synaptic integration in neurons predominantly results in action potentials, which are characterized by three properties: (1) All-or-none behavior, where an adequate level of depolarization results in a full action potential while inadequate levels lead to no response; (2) Action potentials are brief and fast, typically lasting 1-2 ms, and overshoot in amplitude; (3) The amplitude and kinetics of action potentials are highly consistent, meaning that action potentials can be generated over a wide range of frequencies without reduction in amplitude or broadening of the waveform (Sun and Dietrich, 2013). For those reasons, integration of synaptic input is substantially influenced by the all-or-none nature of neuronal firing. The size of the electrical response is determined by the summation of individual synaptic potentials below the threshold; once the accumulated input reaches the action potential threshold, the number of active synapses is largely insignificant. In addition, action potentials' amplitude and speed are significantly higher than synaptic potentials, which allows an effective activation of other voltage-gated ion channels, such as calcium channels. Neuronal input summation has been further complicated by the

discovery of back-propagating action potentials which can infiltrate dendritic compartments and potentially modulate synaptic signals (Stuart et al., 1997; Spruston et al., 2013).

The fairly high density of Na_v channels in OPCs has led to a proposition that similar mechanisms might be involved in signal summation and attenuation in OPC processes (effectively behaving as dendrites). Therefore the capacity of OPCs to generate action potentials is a major question. In cerebellar white matter, a single study has reported the existence of action potential-like depolarizations in a subpopulation of OPCs, upon large current injections (Karadottir et al., 2008). However, other studies did not observe action potentials in these cells and currently it is widely accepted that OPCs are not capable of generating action potential-like spikes outside specific experimental conditions (Bergles et al., 2000; Chittajallu et al., 2004; Lin and Bergles, 2004; Lin et al., 2005; Ziskin et al., 2007; Mangin et al., 2008; Ge et al., 2009; Tong et al., 2009; De Biase et al., 2010, 2011). Despite the absence of action potentials, these channels may serve as amplifiers of synaptic input (Sun et al., 2013). It is known that OPCs express a variable amount of voltage-activated Na^+ channels (Steinhauser et al., 1992; Gallo et al., 1996; Bergles et al., 2000; Diers-Fenger et al., 2001; Chittajallu et al., 2004; Lin and Bergles, 2004; Ge et al., 2006; Karadottir et al., 2008; Kukley et al., 2008; Ge et al., 2009; De Biase et al., 2010; Kukley et al., 2010; Clarke et al., 2012).

In whole-cell current clamp recordings, rectangular shaped current injections are typically used to characterize OPCs. Upon stronger current injections, many investigators report the generation of additional bump-like depolarizations in OPCs, which ride on the exponentially relaxing membrane potential. These bump-like events occur with a delay of > 10 ms to the onset of the current injection, and their amplitude rarely exceeds 10 mV. Additionally, they typically last longer than 20 ms and therefore do not meet the criteria for action potentials. It is likely that voltage-activated sodium channels underlie these bump-like events and also amplify and/or accelerate the rising phase of synaptic potentials in OPCs. This may allow Na^+ channels to enhance certain larger synaptic events and facilitate their discrimination against background activity. It remains to be tested whether sodium channels can activate quickly enough to enhance synaptic input before the large amplitude A-type current counteracts the depolarization, and this will depend largely on the exact kinetics, amplitudes, and membrane time constants involved (Chittajallu et al., 2004; Mangin et al., 2008; Ge et al., 2009; Tong et al., 2009; De Biase et al., 2010; Clarke et al., 2012; Sun and Dietrich, 2013).

Neuron-OPC synapses have a fully functional synaptic release machinery that can repetitively release neurotransmitter in response to trains of presynaptic action potentials, leading to a barrage of synaptic potentials in OPCs. During these barrages, A-type potassium channels and fast sodium channels are expected to rapidly inactivate. However, DR-type potassium channels are well-suited to

counteract this repetitive synaptic activity, as they have sufficient time to activate and remain activated throughout the activity.

DR-type channels may play a role in setting the steady state or plateau membrane potential in OPCs in certain brain regions where the cells experience strong and enduring synaptic input. The frequency-response curve of OPCs may be shaped by the voltage dependence of DR-type channels, potentially leading to a resonance behavior similar to that seen in M-type potassium channels in hippocampal neurons (Hu et al., 2002; Peters et al., 2005).

As OPCs persist into adulthood, they tend to downregulate voltage-gated ion channels and increase the expression of un-gated leak channels, which lowers the cell's input resistance (**Fig.** ; Kressin et al., 1995; Maldonado et al., 2013). While the increase in synaptic input for a certain period may compensate for the drop in input resistance, the eventual expression of background potassium channels (leak channels) will short-circuit the depolarization from synaptic input. Therefore, during adulthood (P50), synaptic potentials in OPCs are less likely to be shaped by voltage-gated channels, as the depolarization from synaptic input may not reach the threshold for activating voltage-gated channels, and the density of voltage-gated channels is likely too low to substantially impact the membrane potential of OPCs. Interestingly, recent works, consistent with our data, indicated that Nav density is developmentally driven, peaking around the time of myelination and declining afterwards but reaching a stable, unchanging density in adulthood (**Fig. 18**; Spitzer et al., 2019).

During the transition from OPCs to pre-myelinating oligodendrocytes, leak channels are down-regulated while voltage-activated channels remain active, making OPCs more receptive to synaptic input. This process occurs during a period when synaptic transmission onto OPCs increases, suggesting that there is a brief developmental window where individual OPCs experience significant synaptic depolarization and shaping by voltage-gated ion channels. Similar developmental changes in ion channel expression have been observed for differentiating A2B5+ O-2A progenitor cells in vitro. Given the strong similarities between oligodendroglial precursor cells in vitro and OPCs in situ, it raises the possibility that OPCs co-cultured with neurons may also form functional synaptic connections, providing a valuable model to study the roles of individual neuron-NG2 cell synapses over time frames that are not feasible with slice experiments.

It should be noted that the predictions about the recruitment of voltage-gated channels by synaptic potentials in OPCs requires experimental verification. The interplay of membrane and gating time constants and voltage dependencies within an individual cell can have a crucial impact on the outcome. Nonetheless, it is expected that the primary purpose of voltage-gated channels is to shape synaptic potentials. It will be intriguing to see whether this shaping serves to dampen or enhance synaptic input in a frequency-independent manner or allows OPCs to differentiate between

glutamatergic and GABAergic transmission, both of which are depolarizing (Sontheimer et al., 1989; Barres et al., 1990). Thus far, no investigations have been conducted to determine the local integration or electrical properties of processes in OPCs.

While the small geometry of OPC processes leads to more pronounced filtering and attenuation along the processes in absolute terms, voltage propagation is comparable to neurons when corrected for the typically shorter processes of OPCs (i.e., 30-50 µm vs. 300 µm maximal length). Therefore, in terms of electronic compactness, OPCs may be considered a miniature rendition of neurons, fully capable of downscaled dendritic computation (Losonczy and Magee, 2006; Wierenga et al., 2008; Routh et al., 2009). OPC may require dendritic computation to effectively myelinate neighboring axons via synaptic transmission. Recently, in vivo imaging of Ca^{2+} activity in single Zebrafish OPCs revealed the existence of Ca^{2+} microdomains (MDs) where the majority of Ca^{2+} signaling happened (Li et al., 2022). This signaling is extremely rarely translated into Ca^{2+} elevations in the soma. Upon differentiation of the OPC Ca^{2+} signals within those MD hotspots predicted myelin formation with 32 ± 9% accuracy (Li et al., 2022). Therefore local synaptic integration by OPCs likely serves a dual purpose: identifying and selectively responding to the synaptic activity of individual axons, and producing a local response in the dendrite that specifically interacts with the corresponding axon. This response could initiate enwrapping or repelling of the axon (Hughes and Appel, 2019).

5.3 Ca^{2+} signaling in OPC processes contributes to synaptic signaling

Ca^{2+} signals in OPCs gradually increase with input strength, enabling them to encode the level of synaptic activity. Unlike neurons, both locally induced and global Ca^{2+} signals in OPCs decay with a time constant of several seconds, whereas in neurons, Ca^{2+} levels typically return to baseline within a few hundred milliseconds. Therefore it has been postulated that Ca^{2+} signals in OPCs, characterized by their low incremental amplitude, slow return to baseline, and reliable occurrence even in distal processes, play a crucial role in effectively integrating synaptic input of a wide range of frequencies across their dendritic tree (Sun et al., 2016).

Although previous studies have shown the presence of VGCCs in OPCs (Haberlandt et al., 2011; Cheli et al., 2014; Larson et al., 2016), only recently it was demonstrated that synaptic-like depolarizations can trigger rapid and robust Ca^{2+} signals in both the soma and processes of OPCs (Sun et al., 2016). These Ca^{2+} signals are mediated by low-threshold VGCCs: (1) they were triggered exclusively by current injections; (2) they appeared when cells were depolarized to -40 mV; (3) they were blocked by Ni^{2+}/Cd^{2+} and a cocktail of R- and T-type channel blockers SNX-482 and TTA-P2; (4) they were potentiated by blocking K^+ channels and showed a rapid rise, indicating that the Ca^{2+} source was active for only a few milliseconds; (5) they were resistant to blocking Na^+/Ca^{2+} exchangers or Ca^{2+}

stores by 10 μM KB-R7943 and thapsigargin. The Ca^{2+} signals recorded in OPCs are different from the Ca^{2+} store-mediated Ca^{2+} elevations seen in astrocytes, which occur and decay over several seconds.

The Ca^{2+} signals in OPC processes induced by local synaptic stimulation or glutamate uncaging are comparable in kinetics and magnitude to those elicited by somatic current injections. This suggests that they also arise from VGCC recruitment. Glutamate receptors could serve as a source of Ca^{2+} entry if more widespread receptor activation was achieved in line with previous observations (see Ge et al., 2006) although Sun et al., 2016 believe that due to the conditions used in their study, (the response was enhanced by 4-AP and the glutamate uncaging protocol alone did not trigger Ca^{2+} responses) glutamate receptors were not a likely source of Ca^{2+}.

The activity of A-type K^+ channels is known to restrict Ca^{2+} signals in OPCs, which has previously led to the conclusion that synaptically-driven Ca^{2+} signals in these cells are unlikely to occur (Velez-Fort et al., 2010; Haberlandt et al., 2011). However, data from Sun et al., 2016 suggests that under control conditions, A-type channels reduce the effectiveness of synaptic input by shortening and decreasing the associated Ca^{2+} signals after the synaptic depolarization. This indicates that the impact of synaptic transmission on Ca^{2+} signaling in OPCs is dependent on A-type K^+ channel activity. Given that Ca^{2+} plays a key role in the developmental behavior and gene expression of OPCs, it is likely that A-type K^+ channels regulate how neuronal transmitter release affects oligodendrogenesis and myelination (Pende et al., 1994; Paez et al., 2009; Paez et al., 2010).

Interestingly, this suggests that OPCs are most responsive to synaptic input from neurons when A-type channels are suppressed. This raises questions about how and under which conditions such suppression can be achieved. Activity of A-type channels can be reduced when membrane depolarization brings them into a state of inactivation. Thus, patterns of synaptic input that maximize inactivation of A-type channels enhance the impact of axonal activity on OPC behavior. Based on previous reports on the kinetics of A-type K^+ channels (Steinhauser et al., 1994b), the authors suggest that brief trains of action potentials (50–100 ms) should be very effective at inactivating A-type channels and opening the 'calcium-gate' in OPCs.

Further supporting the hypothesis of dendritic computation, in the study the absolute depolarization of the soma was clearly below the voltage range typically required to reliably induce Ca^{2+} signals and all Ca^{2+} signals recorded in dendrites, regardless of whether induced by synaptic stimulation, by a train of mock PSPs, by Gaussian distributed mock PSPs, or by glutamate uncaging, display a rapid rise, indicating that the Ca^{2+} source must be very close to the optical recording site in the processes. Additionally, Ca^{2+} signals induced in the soma rapidly spread into all dendrites and reached even the distal ends with undiminished amplitudes (Sun et al., 2016). This can only be

achieved if VGCCs are present all along the processes to regenerate the signal. No processes were found that did not generate Ca^{2+} responses, therefore indicating that most, if not all, OPC processes are equipped with VGCCs (Haberlandt et al., 2011; Sun et al., 2016).

The data suggests that voltage-dependent Ca^{2+} and K^+ channels in the processes of OPCs function as independent processing units. The localization of A-type channels in OPC processes further supports this view (measured indirectly; see Sun et al., 2016). When these channels were blocked with 4-AP, glutamate uncaging was able to recruit more Ca^{2+} channels by a stronger depolarization compared to control conditions, even though the resulting depolarization measured at the soma was negligible. Thus, 4-AP must have allowed for a larger depolarization of the local membrane in the dendrite in response to uncaging, which was not visible in the somatic recording. The most plausible explanation is that 4-AP was also acting on dendritic A-type K^+ channels, which rendered dendritic glutamate uncaging more effective in generating a larger local depolarization and recruiting dendritic VGCCs. Overall, these findings demonstrate that OPCs express voltage-dependent Ca^{2+} and K^+ channels in their dendrites, and these channels actively shape synaptic input as independent processing units.

5.4 Plasticity at OPC synapses

In our work we show a developmental change in the short-term plasticity of OPC synapses, changing from strong depression at juvenility (P10) to potentiation in adulthood (P50) [**Fig. 19**; **Fig. 21**]. Neuronal literature shows numerous examples of developmentally driven changes in the plasticity of central synapses [**Fig. 35**]. Based on this property, most synapses in the CNS can be divided into 2 subcategories, serving different functions: High-release probability synapses which usually undergo short term depression (STD, as in the cerebellum), functioning as high fidelity detectors of the initial input, desensitize if the input is present repeatedly. Low release probability synapses usually undergo potentiation (STP), therefore functioning as detectors of repetitive or periodic input (Regehr, 2012).

The underlying mechanism of STP is unknown. Since STP develops rapidly within seconds after stimulation, it is likely that rapid changes in synaptic strength may be an effect of phosphorylation of AMPARs which are already present within the synapse. It is, therefore, reasonable to consider phosphorylation by CaMKII as a candidate mechanism for STP and working memory, as this phosphorylation increases channel conductance of AMPARs (Hosokawa et al., 2014). GluA1 knockout mice experiments have shown a considerable deficiency in both STP and working memory, indicating a possible role of STP in working memory (Erickson et al., 2010; Sanderson, et al., 2009). However, in neurons, STP is also linked to NMDARs activation, while OPC synapses typically do not contain NMDARs (De Biase et al., 2010).

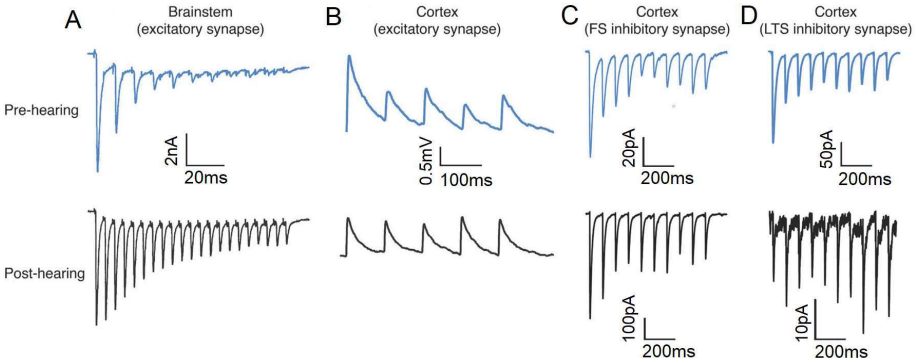

Figure 35. Development of short-term synaptic plasticity in the auditory system, before and after the onset of hearing. (A) AMPAR-mediated excitatory postsynaptic currents recorded in auditory brain stem MNTB neurons in response to a 200Hz stimulus train. Examples are shown from pre-hearing (P9)and post-hearing (P14) neurons. Before the onset of hearing, synaptic depression and failures were observed, but the depression was reduced after hearing onset with no failures. (B) Excitatory postsynaptic potentials (EPSP) recorded in auditory cortex Layer 3 pyramidal neurons in response to stimulation of a second Layer 3 neuron. In P11, stimulation of the presynaptic neuron at 10Hz evoked EPSPs that declined in amplitude (STD). At P28, stimulation at the same rate did not produce STD. (C) Inhibitory postsynaptic currents (IPSC) were recorded in auditory cortex Layer 3 pyramidal neurons in response to stimulation of either FS (left) or LTS (right) inhibitory interneurons. In P10 cortex, stimulation of either inhibitory neuron led to STD. After the onset of hearing the FS-evoked response led to STP. Adopted from: Sanes et al., 2019.

Currently very little is known about STP at neuron-OPC synapses during callosal development. During adulthood the synapses tend to strongly potentiate and in gray matter may display some characteristics of long term potentiation (LTP) upon repetitive stimulation (Ge et al., 2006). OPC synapses share certain similarities with immature neuronal synapses, which usually have limited vesicular pool, no clear post-synaptic density (PSD) and much tighter apposition of pre- and postsynaptic membranes (adhesion junction), resulting in fast kinetics of synaptic currents. In contrast, mature, well established synapses contain large pools of synaptic vesicles, clear PSD and broader cleft resulting in slower rise times of EPSC (Sanes et al., 2019). The qEPSC currents of OPCs in all investigated ages displayed a striking similarity to those at young neuronal synapses with a very sharp rise time of ~0.5ms which is 3-4 times faster than most neuronal synapses in the cortex or hippocampus (Silberberg et al., 2004; Fricker and Miles, 2000). OPC NG2 protein contains neurexin-like domains which serve as adhesive modules for synapse assembly (Trotter et al., 2010) and PDZ binding motif interacting with AMPAR anchoring GRIP, commonly expressed at neuronal synapses

(Dong et al., 1997). In addition, OPCs interact with axons through N-cadherins, required for the maintenance of nascent dendrite arbors. This view is further supported by the finding that OPCs do not disintegrate their connections during cell division and inherit existing synapses (Kukley et al., 2008). However, it is likely that neuron-OPC synapses might be unstable over time due to the high migration rate of OPCs (Hughes et al., 2013).

A defining characteristic of synapses in their activity profile upon repeated activation by action potentials, where successive stimuli can lead to either short-term facilitation (STP) or short-term depression (STD). This short-term plasticity (STP) plays a crucial role in temporal computation (Deng and Klyachko, 2011). Multiple mechanisms have been proposed to explain differences in STP: changes in the responsiveness of receptors to neurotransmitter binding, alterations in calcium signaling and the sensitivity of vesicle fusion have been observed at various neuronal synapses. Presynaptic STD is often attributed to synapses with high probability release, where a single AP causes a significant depletion of the readily releasable pool (RRP). Conversely, presynaptic STP is often linked to synapses with low initial release probability and a rapid increase in release probability during successive APs can be caused by regulation of calcium channels (Catterall et al., 2013; Holbro et al., 2009), saturation of local calcium buffers (Matveev et al., 2004), or accumulation of intracellular calcium (Deperrois and Graupner, 2020; Zucker and Regehr, 2002). Throughout callosal development neuronal-glial synapses change from ones unable to sustain long periods of continuous glutamate release (STD) to ones able to sustain such activity (STP). Interestingly, in our study the release probability to single pulses at the synapses is comparable at all age groups (0.0975 +/- 0.0272 at P10, 0.0956 +/- 0.0152 at P20, 0.0736 +/- 0.0186 at P50), therefore the synapses can be considered as having low release probability throughout callosal development. The presence of STD at P10 strongly suggests that the pool of available vesicles might be small during early development and is expanded during later developmental stages. This mimics developments at neuronal synapses undergoing STP, where the number of available vesicles triples during synapse maturation. However, the STP developing at P20, and likely complete by P50, is probably involving additional mechanisms linked with Ca^{2+} regulation responsible for the priming reflected in the change of the EPSC onsets [**Fig. 20**].

5.5 Vesicle pool in short-term plasticity

The properties of presynaptic vesicles play a crucial role in determining synaptic efficacy and contribute to short-term plasticity. Vesicles are often grouped into functional pools, but there is no universally agreed-upon classification (Schneggenburger et al. 2002; Rizzoli and Betz, 2005; Becherer and Rettig, 2006; Schweizer and Ryan, 2006). In this discussion, we will adopt the terminology used by Betz (Rizzoli and Betz, 2005).

Each active zone of a presynaptic terminal usually contains hundreds of vesicles. The recycling pool (RP) constitutes a fraction (usually 10-20%) of these vesicles and is released during sustained high-frequency activation. The readily releasable pool (RRP) is immediately available upon presynaptic cell stimulation. The remaining vesicles, known as the non recycling pool (NRP), are difficult to release. The size of the RRP can be determined by applying a hypertonic sucrose solution (Rosenmund and Stevens, 1996) or by using a large sustained elevation of presynaptic calcium produced by depolarization or calcium uncaging (Schneggenburger et al., 2002; Rizzoli and Betz, 2005; Fioravante and Regehr, 2011). The RRP typically consists of several percent of the vesicles within a presynaptic bouton (Rizzoli and Betz, 2005; Becherer and Rettig, 2006; Schweizer and Ryan, 2006). In some synapses, the RRP is divided into fast and slow vesicle pools, which are differentially recruited and differ in their propensity to release (Wu and Borst, 1999; Sakaba and Neher, 2001). The different vesicle pools may be due to the distance from voltage-gated calcium channels (Wadel et al., 2007).

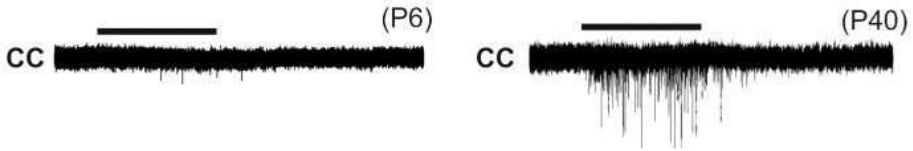

Figure 36. Developmental differences in vesicular release in corpus callosum. (left) Sucrose application to callosal fibers leads to low number of synaptic vesicles release at P6. (right) The same concentration of sucrose, applied over the same time releases large number of vesicles at P40. Adapted from: De Biase et al., 2010.

Our results from the 100Hz train stimulations in the P10 age group suggested limited vesicle availability [**Fig. 19G-I, K**; **Fig. 21J-L, N; Fig. 36**]. Synaptic responses displayed deep depression and became exceedingly rare. Furthermore the median EPSC onset was delayed by more than 1ms with a high variance. During callosal development synaptic depression changed into potentiation, onset delays progressively changed into brief increase in release speed, more prominent at P50 than at P20 [**Fig. 20**]. Our view is indirectly supported by previous experiments in CC, where puff application of sucrose (causing vesicular release through osmotic shock) to the callosal fibers triggered release of a small number of mEPSCs in P6 OPCs but a much higher number, with larger amplitudes at P40 [**Fig. 36**] (De Biase, 2010).

5.6 OPCs are highly dynamic cells, continuously migrating through the brain

OPCs are a highly dynamic population in the resting brain surveying their local environment with motile filopodia, and they continuously migrate through the brain parenchyma while maintaining exclusive territories through self-repulsion (Hughes et al., 2013). Whenever OPCs are removed from the population through differentiation or death, they are rapidly replaced through the proliferation of an immediate neighbor. High density of these progenitors throughout the CNS contributes to tissue repair and efficient generation of oligodendrocytes. Individual OPCs occupy non-overlapping domains, and they are distributed in a grid-like or tiled manner. However, mechanisms which limit the growth of these progenitors, given that the grid is constantly reorganized, are currently unknown. Homotypic repulsive interactions through transmembrane receptors, such as MEGFs and DSCAM (Kay et al., 2012; Fuerst et al., 2008), regulate the mosaic spacing of neurons in vertebrates and invertebrates alike. Similar interactions are likely to play a crucial role in both establishing and maintaining the density of OPCs since the selective ablation of individual cells is sufficient to trigger a rapid invasion of the territory of the removed cell, and contact between OPC processes was always followed by retraction. Homotypic repulsion would also provide the means to establish and maintain the radial orientation of their processes (Lefebvre et al., 2012; Hughes et al., 2013) Enhanced access to mitogens, such as platelet-derived growth factor (PDGF), may be a mechanism through which proliferation of these progenitors may be triggered. In vitro studies have shown that oligodendrocyte progenitors display a decrease in proliferation with increasing density of platelet-derived growth factor (PDGF) (Calver et al., 1998; Baron et al., 2000), indicating that direct interactions may regulate their growth. Although molecules like netrin and semaphorins have been identified to affect the dispersion and differentiation of oligodendrocyte progenitors during development (Spassky et al., 2002), the mechanisms responsible for maintaining their density in the adult CNS remain to be discovered. Given the extensive overlap of OPC processes with other tiling glial cells like astrocytes and microglia, it is probable that distinct molecular pathways control the distribution and density of different glial cell types.

Continuous imaging of OPCs in the cortex has revealed that the entire OPC network undergoes continuous reorganization, due to cell loss and their inherent pressure to actively survey the surrounding environment (Hughes et al., 2013). Individual cell migration was triggered by local events, such as the differentiation, death, or displacement of neighboring cells, rather than large-scale attractive or repulsive gradients. The local proliferation of neighboring cells was the primary mechanism for maintaining the OPC population and migration of single cells over long distances was not observed, consistent with the remarkable self-repulsion of these cells. OPCs are equipped with

dynamic filopodia, which extend along their processes and from their somata, to explore the local envi-

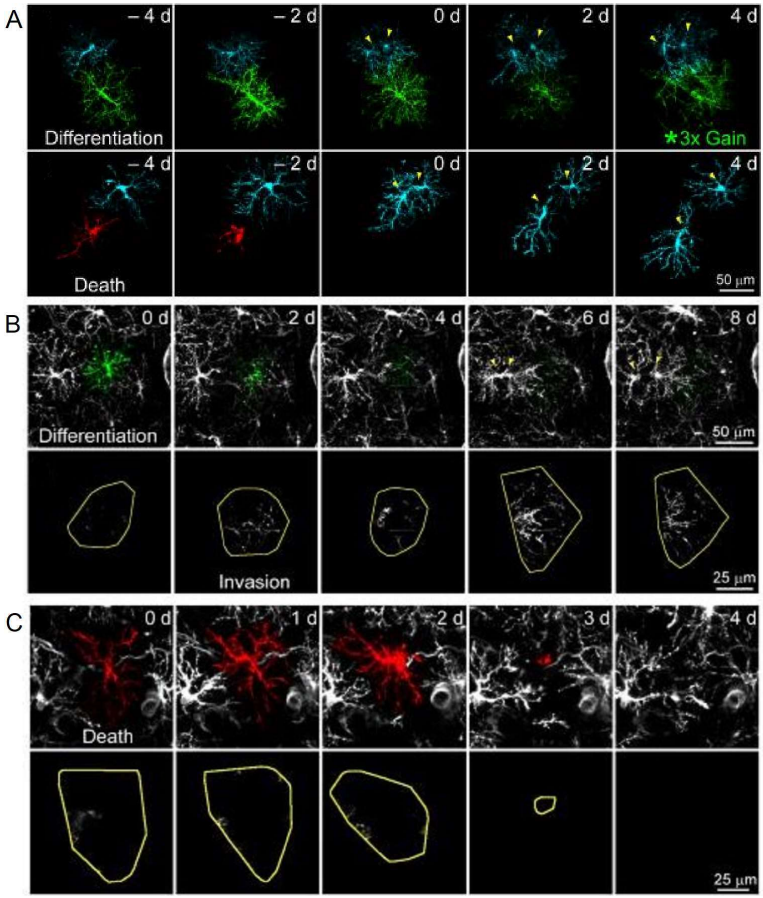

Figure 37. OPC density is maintained through local proliferation. (A) Images from time-lapse images showing OPC differentiation (green cell) or death (red cell) is associated with proliferation (yellow arrowheads) of a neighboring OPC (cyan). The intensity for the differentiating cell at day 4 has been increased 3x to highlight the morphological change. (B) Top: In vivo time-lapse images of an individual OPC (pseudo-colored green) that differentiated into an oligodendrocyte during the 8 day imaging period. Note that differentiation resulted in processes extension and proliferation (yellow arrowheads) of the neighboring OPCs surrounding the differentiating cell. Bottom: Montage showing the territory of the differentiating cell

(yellow) overlaid with the processes of neighboring OPCs (white) that entered the territory of the differentiating cell. Note that there was extensive invasion of cell territory very early in the differentiation process. (C) Top: In vivo time-lapse images of an individual OPC (pseudo-colored red) that died during the 4 day imaging period. Bottom: Montage showing the territory of the dying cell (yellow) overlaid with the processes of neighboring OPCs (white) that entered the territory of the dying cell.

-ronment and evaluate the density of other OPCs, the state of myelination of nearby axons, and the viability of oligodendrocytes. The preservation of a high density OPC network in the adult CNS may enable them to detect demyelinated axons and play a role in oligodendrocyte regeneration, which is impaired in many chronically demyelinated white matter lesions in multiple sclerosis (MS) (Chang et al., 2000; Franklin et al., 1997). The restoration of OPC numbers in such lesions may be therapeutically advantageous in MS (Boyd et al., 2013; Kirby et al., 2019).

Due to the high motility and constant movement through the parenchyma it was suggested that synapses between OPCs and axons are continually remodeled, likely on a time scale of days to weeks. While the role of this rapid communication in vivo is unclear, glutamatergic signaling has been shown to influence the proliferation and differentiation of these progenitors in vivo (Nagy et al., 2018; Gibson et al., 2014). As OPCs occupy non-overlapping domains, the continual reorganization of their processes may enable them to sample the activity of a greater proportion of axons, potentially allowing for learning-induced changes in myelination and rapid replacement of degenerating oligodendrocytes. In vivo genetic fate tracing studies have shown that OPCs continue to generate oligodendrocytes in the adult CNS, albeit at a lower rate than during early postnatal life. Time-lapse imaging has confirmed that OPCs in the cortex of 5-month-old mice continue to differentiate into oligodendrocytes at a low rate (Kang et al., 2010; Rivers et al., 2008; Young et al., 2013). In vitro studies have indicated that oligodendrocytes are generated through asymmetric division of oligodendrocyte progenitors, but the steps leading to oligodendrogenesis in vivo have remained uncertain. Through long-term imaging, it has been discovered that the majority of OPCs in the adult cortex directly differentiate into oligodendrocytes. This suggests that proliferation of OPCs in vivo is not necessarily a direct reflection of oligodendrogenesis, but rather a homeostatic response to replace progenitors that have differentiated or died (Hughes et al., 2013).

6. Conclusions

In the present study we found that synaptic properties of callosal OPCs change remarkably during development. Most of the changes display characteristics reported for various neuronal synapses. Changes in the synaptic properties are linked with a gradual shift in OPC intrinsic properties, which change in a way suggesting that OPCs become less responsive to the synaptic input. Therefore the shift in synaptic plasticity reported in our work, from STD to STP, could highlight a change in the mode of OPC activation: in adulthood, contrary to juvenility, to overcome the higher passive signal filtering introduced by substantial decrease in R_m and V_m concerted activation of multiple synaptic inputs might be necessary. Interestingly, the dramatic changes in the properties of synaptic input are accompanied by a remarkable stability of OPC morphology and branching.

Therefore, understanding the mechanisms by which synaptic signaling regulates OPC proliferation and differentiation at distinct developmental stages could be of fundamental importance to evaluate the role of those cells in health and disease.

7. Future perspectives

In the future, research on the development of the oligodendrocyte lineage should focus on expanding our knowledge of the molecular factors that determine lineage specification, as well as intrinsic and extrinsic regulators of cell proliferation and differentiation. Additionally, studying transcription factors that modulate myelin gene expression will be crucial. It is important to determine whether transcriptional and developmental programs are synaptically regulated in this population of glial progenitors, and if AMPAR activity or Ca^{2+} influx through these channels selectively affect specific phases of OPC development. Further research should investigate whether postsynaptic specializations in OPCs are similar to those in neurons. Especially for callosal projection neurons it would be worthwhile to investigate whether ipsi- and contralateral neuronal synapses share similarities with CPN synapses onto callosal OPC. The study of these synapses has significant potential for clinical translation, as it may enhance our understanding of neurological and developmental disorders involving white matter.

Moreover, recent studies suggest that oligodendrocyte precursor cells (OPCs) have additional functions beyond serving as progenitors for oligodendrocytes. OPCs have been observed in non-myelinated regions and have been shown to migrate to sites of injury where they contribute to scar formation, similar to microglia (Hughes et al., 2013). Furthermore, studies indicate that OPCs can transform into inflammatory OPCs (iOPCs) that present exogenous antigens through MHC class I and II when exposed to inflammatory cytokines, suggesting that they may play a role in modulating tissue inflammation (Kirby et al., 2019; Falcão et al., 2018; Jin et al., 2018). OPCs share many features with microglia, such as a similar density, grid-like distribution with non-overlapping domains, ramified and radially-oriented processes, and high motility with dynamic filopodia (Hughes et al., 2013). Given their robust dynamics and broad distribution, OPCs are well-positioned to modify neural circuits. Recent discovery of phagosome-like structures inside OPC processes and the continuous presence of OPCs throughout the CNS, which retain similar morphology and dynamics, raises the possibility that they may have the ability to modify circuits and clear cellular debris induced by injury or normal aging (Buchanan et al., 2022; Jin et al., 2018).

8. References

Agnati LF, Guidolin D, Guescini M, Genedani S, Fuxe K. Understanding wiring and volume transmission. Brain Res Rev. 2010;64(1):137-159. doi:10.1016/j.brainresrev.2010.03.003

Aguirre A, Gallo V. Postnatal neurogenesis and gliogenesis in the olfactory bulb from NG2-expressing progenitors of the subventricular zone [published correction appears in J Neurosci. 2004 Dec 1;24(48):1 p following 10973]. J Neurosci. 2004;24(46):10530-10541. doi:10.1523/JNEUROSCI.3572-04.2004

Aguirre AA, Chittajallu R, Belachew S, Gallo V. NG2-expressing cells in the subventricular zone are type C-like cells and contribute to interneuron generation in the postnatal hippocampus. J Cell Biol. 2004;165(4):575-589. doi:10.1083/jcb.200311141

Akopian G, Kressin K, Derouiche A, Steinhäuser C. Identified glial cells in the early postnatal mouse hippocampus display different types of Ca2+ currents. Glia. 1996;17(3):181-194. doi:10.1002/(SICI)1098-1136(199607)17:3<181::AID-GLIA1>3.0.CO;2-4

Alonso G. Prolonged corticosterone treatment of adult rats inhibits the proliferation of oligodendrocyte progenitors present throughout white and gray matter regions of the brain. Glia. 2000;31(3):219-231. doi:10.1002/1098-1136(200009)31:3<219::aid-glia30>3.0.co;2-r

Attali B, Wang N, Kolot A, Sobko A, Cherepanov V, Soliven B. Characterization of delayed rectifier Kv channels in oligodendrocytes and progenitor cells. J Neurosci. 1997;17(21):8234-8245. doi:10.1523/JNEUROSCI.17-21-08234.1997

Baron W, Metz B, Bansal R, Hoekstra D, de Vries H. PDGF and FGF-2 signaling in oligodendrocyte progenitor cells: regulation of proliferation and differentiation by multiple intracellular signaling pathways. Mol Cell Neurosci. 2000;15(3):314-329. doi:10.1006/mcne.1999.0827

Barres BA, Koroshetz WJ, Swartz KJ, Chun LL, Corey DP. Ion channel expression by white matter glia: the O-2A glial progenitor cell. Neuron. 1990;4(4):507-524. doi:10.1016/0896-6273(90)90109-s

Barritt DS, Pearn MT, Zisch AH, et al. The multi-PDZ domain protein MUPP1 is a cytoplasmic ligand for the membrane-spanning proteoglycan NG2. J Cell Biochem. 2000;79(2):213-224. doi:10.1002/1097-4644(20001101)79:2<213::aid-jcb50>3.0.co;2-g

Baucum AJ 2nd. Proteomic Analysis of Postsynaptic Protein Complexes Underlying Neuronal Plasticity. ACS Chem Neurosci. 2017;8(4):689-701. doi:10.1021/acschemneuro.7b00008

Becherer U, Rettig J. Vesicle pools, docking, priming, and release. Cell Tissue Res. 2006;326(2):393-407. doi:10.1007/s00441-006-0243-z

Beekman JM, Coffer PJ. The ins and outs of syntenin, a multifunctional intracellular adaptor protein. J Cell Sci. 2008;121(Pt 9):1349-1355. doi:10.1242/jcs.026401

Bekar LK, Loewen ME, Cao K, et al. Complex expression and localization of inactivating Kv channels in cultured hippocampal astrocytes. J Neurophysiol. 2005;93(3):1699-1709. doi:10.1152/jn.00850.2004

Belachew S, Chittajallu R, Aguirre AA, et al. Postnatal NG2 proteoglycan-expressing progenitor cells are intrinsically multipotent and generate functional neurons. J Cell Biol. 2003;161(1):169-186. doi:10.1083/jcb.200210110

Berger T, Schnitzer J, Kettenmann H. Developmental changes in the membrane current pattern, K+ buffer capacity, and morphology of glial cells in the corpus callosum slice. J Neurosci. 1991;11(10):3008-3024. doi:10.1523/JNEUROSCI.11-10-03008.1991

Berger T, Schnitzer J, Orkand PM, Kettenmann H. Sodium and Calcium Currents in Glial Cells of the Mouse Corpus Callosum Slice. Eur J Neurosci. 1992;4(12):1271-1284. doi:10.1111/j.1460-9568.1992.tb00153.x

Berger T. AMPA-type glutamate receptors in glial precursor cells of the rat corpus callosum: ionic and pharmacological properties. Glia. 1995;14(2):101-114. doi:10.1002/glia.440140205

Bergles DE, Roberts JD, Somogyi P, Jahr CE. Glutamatergic synapses on oligodendrocyte precursor cells in the hippocampus. Nature. 2000;405(6783):187-191. doi:10.1038/35012083

Bergles DE, Jabs R, Steinhäuser C. Neuron-glia synapses in the brain. Brain Res Rev. 2010;63(1-2):130-137. doi:10.1016/j.brainresrev.2009.12.003

Berry M, Hubbard P, Butt AM. Cytology and lineage of NG2-positive glia. J Neurocytol. 2002;31(6-7):457-467. doi:10.1023/a:1025735513560

Biederer T, Kaeser PS, Blanpied TA. Transcellular Nanoalignment of Synaptic Function. Neuron. 2017;96(3):680-696. doi:10.1016/j.neuron.2017.10.006

Blanz J, Schweizer M, Auberson M, et al. Leukoencephalopathy upon disruption of the chloride channel CIC-2. J Neurosci. 2007;27(24):6581-6589. doi:10.1523/JNEUROSCI.0338-07.2007

Borges K, Wolswijk G, Ohlemeyer C, Kettenmann H. Adult rat optic nerve oligodendrocyte progenitor cells express a distinct repertoire of voltage- and ligand-gated ion channels. J Neurosci Res. 1995;40(5):591-605. doi:10.1002/jnr.490400504

Boucsein C, Zacharias R, Färber K, Pavlovic S, Hanisch UK, Kettenmann H. Purinergic receptors on microglial cells: functional expression in acute brain slices and modulation of microglial activation in vitro. Eur J Neurosci. 2003;17(11):2267-2276. doi:10.1046/j.1460-9568.2003.02663.x

Boyd A, Zhang H, Williams A. Insufficient OPC migration into demyelinated lesions is a cause of poor remyelination in MS and mouse models. Acta Neuropathol. 2013;125(6):841-859. doi:10.1007/s00401-013-1112-y

Buchanan J, Elabbady L, Collman F, et al. Oligodendrocyte precursor cells ingest axons in the mouse neocortex. Proc Natl Acad Sci U S A. 2022;119(48):e2202580119. doi:10.1073/pnas.2202580119

Butt AM, Kalsi A. Inwardly rectifying potassium channels (Kir) in central nervous system glia: a special role for Kir4.1 in glial functions. J Cell Mol Med. 2006;10(1):33-44. doi:10.1111/j.1582-4934.2006.tb00289.x

Butt AM, Pugh M, Hubbard P, James G. Functions of optic nerve glia: axoglial signalling in physiology and pathology. Eye (Lond). 2004;18(11):1110-1121. doi:10.1038/sj.eye.6701595

Buttigieg J, Eftekharpour E, Karimi-Abdolrezaee S, Fehlings MG. Molecular and electrophysiological evidence for the expression of BK channels in oligodendroglial precursor cells. Eur J Neurosci. 2011;34(4):538-547. doi:10.1111/j.1460-9568.2011.07789.x

Cahoy JD, Emery B, Kaushal A, et al. A transcriptome database for astrocytes, neurons, and oligodendrocytes: a new resource for understanding brain development and function. J Neurosci. 2008;28(1):264-278. doi:10.1523/JNEUROSCI.4178-07.2008

Calver AR, Hall AC, Yu WP, et al. Oligodendrocyte population dynamics and the role of PDGF in vivo. Neuron. 1998;20(5):869-882. doi:10.1016/s0896-6273(00)80469-9

Catterall WA, Leal K, Nanou E. Calcium channels and short-term synaptic plasticity. J Biol Chem. 2013;288(15):10742-10749. doi:10.1074/jbc.R112.411645

Chang A, Nishiyama A, Peterson J, Prineas J, Trapp BD. NG2-positive oligodendrocyte progenitor cells in adult human brain and multiple sclerosis lesions. J Neurosci. 2000;20(17):6404-6412. doi:10.1523/JNEUROSCI.20-17-06404.2000

Chang SY, Zagha E, Kwon ES, et al. Distribution of Kv3.3 potassium channel subunits in distinct neuronal populations of mouse brain. J Comp Neurol. 2007;502(6):953-972. doi:10.1002/cne.21353

Chatterjee N, Stegmüller J, Schätzle P, et al. Interaction of syntenin-1 and the NG2 proteoglycan in migratory oligodendrocyte precursor cells. J Biol Chem. 2008;283(13):8310-8317. doi:10.1074/jbc.M706074200

Cheli VT, Santiago González DA, Spreuer V, Paez PM. Voltage-gated Ca2+ entry promotes oligodendrocyte progenitor cell maturation and myelination in vitro. Exp Neurol. 2015;265:69-83. doi:10.1016/j.expneurol.2014.12.012

Chen TJ, Kula B, Nagy B, et al. In Vivo Regulation of Oligodendrocyte Precursor Cell Proliferation and Differentiation by the AMPA-Receptor Subunit GluA2. Cell Rep. 2018;25(4):852-861.e7. doi:10.1016/j.celrep.2018.09.066

Cherniak C. Local optimization of neuron arbors. Biol Cybern. 1992;66(6):503-510. doi:10.1007/BF00204115

Chever O, Djukic B, McCarthy KD, Amzica F. Implication of Kir4.1 channel in excess potassium clearance: an in vivo study on anesthetized glial-conditional Kir4.1 knock-out mice. J Neurosci. 2010;30(47):15769-15777. doi:10.1523/JNEUROSCI.2078-10.2010

Chittajallu R, Chen Y, Wang H, et al. Regulation of Kv1 subunit expression in oligodendrocyte progenitor cells and their role in G1/S phase progression of the cell cycle. Proc Natl Acad Sci U S A. 2002;99(4):2350-2355. doi:10.1073/pnas.042698399

Chittajallu R, Aguirre A, Gallo V. NG2-positive cells in the mouse white and grey matter display distinct physiological properties. J Physiol. 2004;561(Pt 1):109-122. doi:10.1113/jphysiol.2004.074252

Chklovskii DB. Synaptic connectivity and neuronal morphology: two sides of the same coin. Neuron. 2004;43(5):609-617. doi:10.1016/j.neuron.2004.08.012

Clapham DE, Julius D, Montell C, Schultz G. International Union of Pharmacology. XLIX. Nomenclature and structure-function relationships of transient receptor potential channels. Pharmacol Rev. 2005;57(4):427-450. doi:10.1124/pr.57.4.6

Clarke LE, Young KM, Hamilton NB, Li H, Richardson WD, Attwell D. Properties and fate of oligodendrocyte progenitor cells in the corpus callosum, motor cortex, and piriform cortex of the mouse. J Neurosci. 2012;32(24):8173-8185. doi:10.1523/JNEUROSCI.0928-12.2012

Collins MO, Husi H, Yu L, et al. Molecular characterization and comparison of the components and multiprotein complexes in the postsynaptic proteome. J Neurochem. 2006;97 Suppl 1:16-23. doi:10.1111/j.1471-4159.2005.03507.x

Davalos D, Grutzendler J, Yang G, et al. ATP mediates rapid microglial response to local brain injury in vivo. Nat Neurosci. 2005;8(6):752-758. doi:10.1038/nn1472

Dawson MR, Levine JM, Reynolds R. NG2-expressing cells in the central nervous system: are they oligodendroglial progenitors?. J Neurosci Res. 2000;61(5):471-479. doi:10.1002/1097-4547(20000901)61:5<471::AID-JNR1>3.0.CO;2-N

Dawson MR, Polito A, Levine JM, Reynolds R. NG2-expressing glial progenitor cells: an abundant and widespread population of cycling cells in the adult rat CNS. Mol Cell Neurosci. 2003;24(2):476-488. doi:10.1016/s1044-7431(03)00210-0

Dayer AG, Cleaver KM, Abouantoun T, Cameron HA. New GABAergic interneurons in the adult neocortex and striatum are generated from different precursors. J Cell Biol. 2005;168(3):415-427. doi:10.1083/jcb.200407053

De Biase LM, Nishiyama A, Bergles DE. Excitability and synaptic communication within the oligodendrocyte lineage. J Neurosci. 2010;30(10):3600-3611. doi:10.1523/JNEUROSCI.6000-09.2010

De Biase LM, Kang SH, Baxi EG, et al. NMDA receptor signaling in oligodendrocyte progenitors is not required for oligodendrogenesis and myelination. J Neurosci. 2011;31(35):12650-12662. doi:10.1523/JNEUROSCI.2455-11.2011

Del Castillo, J., & Katz, B. (1954). Quantal components of the end-plate potential. The Journal of physiology, 124(3), 560–573.

Deng PY, Klyachko VA. The diverse functions of short-term plasticity components in synaptic computations. Commun Integr Biol. 2011;4(5):543-548. doi:10.4161/cib.4.5.15870

Deng W, Wang H, Rosenberg PA, Volpe JJ, Jensen FE. Role of metabotropic glutamate receptors in oligodendrocyte excitotoxicity and oxidative stress. Proc Natl Acad Sci U S A. 2004;101(20):7751-7756. doi:10.1073/pnas.0307850101

Deperrois N, Graupner M. Short-term depression and long-term plasticity together tune sensitive range of synaptic plasticity. PLoS Comput Biol. 2020;16(9):e1008265. Published 2020 Sep 25. doi:10.1371/journal.pcbi.1008265

Derkach V, Barria A, Soderling TR. Ca2+/calmodulin-kinase II enhances channel conductance of alpha-amino-3-hydroxy-5-methyl-4-isoxazolepropionate type glutamate receptors. Proc Natl Acad Sci U S A. 1999;96(6):3269-3274. doi:10.1073/pnas.96.6.3269

Diers-Fenger M, Kirchhoff F, Kettenmann H, Levine JM, Trotter J. AN2/NG2 protein-expressing glial progenitor cells in the murine CNS: isolation, differentiation, and association with radial glia. Glia. 2001;34(3):213-228. doi:10.1002/glia.1055

Dimou L, Simon C, Kirchhoff F, Takebayashi H, Götz M. Progeny of Olig2-expressing progenitors in the gray and white matter of the adult mouse cerebral cortex. J Neurosci. 2008;28(41):10434-10442. doi:10.1523/JNEUROSCI.2831-08.2008

Djukic B, Casper KB, Philpot BD, Chin LS, McCarthy KD. Conditional knock-out of Kir4.1 leads to glial membrane depolarization, inhibition of potassium and glutamate uptake, and enhanced short-term synaptic potentiation. J Neurosci. 2007;27(42):11354-11365. doi:10.1523/JNEUROSCI.0723-07.2007

Dong H, O'Brien RJ, Fung ET, Lanahan AA, Worley PF, Huganir RL. GRIP: a synaptic PDZ domain-containing protein that interacts with AMPA receptors. Nature. 1997;386(6622):279-284. doi:10.1038/386279a0

Du J, Tao-Cheng JH, Zerfas P, McBain CJ. The K+ channel, Kv2.1, is apposed to astrocytic processes and is associated with inhibitory postsynaptic membranes in hippocampal and cortical principal neurons and inhibitory interneurons. Neuroscience. 1998;84(1):37-48. doi:10.1016/s0306-4522(97)00519-8

Duan S, Anderson CM, Keung EC, Chen Y, Chen Y, Swanson RA. P2X7 receptor-mediated release of excitatory amino acids from astrocytes. J Neurosci. 2003;23(4):1320-1328. doi:10.1523/JNEUROSCI.23-04-01320.2003

Duguid IC, Pankratov Y, Moss GW, Smart TG. Somatodendritic release of glutamate regulates synaptic inhibition in cerebellar Purkinje cells via autocrine mGluR1 activation. J Neurosci. 2007;27(46):12464-12474. doi:10.1523/JNEUROSCI.0178-07.2007

Erickson MA, Maramara LA, Lisman J. A single brief burst induces GluR1-dependent associative short-term potentiation: a potential mechanism for short-term memory. J Cogn Neurosci. 2010;22(11):2530-2540. doi:10.1162/jocn.2009.21375

Etxeberria A, Mangin JM, Aguirre A, Gallo V. Adult-born SVZ progenitors receive transient synapses during remyelination in corpus callosum. Nat Neurosci. 2010;13(3):287-289. doi:10.1038/nn.2500

Falcão AM, van Bruggen D, Marques S, et al. Disease-specific oligodendrocyte lineage cells arise in multiple sclerosis. Nat Med. 2018;24(12):1837-1844. doi:10.1038/s41591-018-0236-y

Feliciangeli S, Tardy MP, Sandoz G, et al. Potassium channel silencing by constitutive endocytosis and intracellular sequestration. J Biol Chem. 2010;285(7):4798-4805. doi:10.1074/jbc.M109.078535

Feliciangeli S, Chatelain FC, Bichet D, Lesage F. The family of K2P channels: salient structural and functional properties. J Physiol. 2015;593(12):2587-2603. doi:10.1113/jphysiol.2014.287268

Fernández-Chacón R, Königstorfer A, Gerber SH, et al. Synaptotagmin I functions as a calcium regulator of release probability. Nature. 2001;410(6824):41-49. doi:10.1038/35065004

Fiacco TA, McCarthy KD. Multiple Lines of Evidence Indicate That Gliotransmission Does Not Occur under Physiological Conditions. J Neurosci. 2018;38(1):3-13. doi:10.1523/JNEUROSCI.0016-17.2017

Fioravante D, Regehr WG. Short-term forms of presynaptic plasticity. Curr Opin Neurobiol. 2011;21(2):269-274. doi:10.1016/j.conb.2011.02.003

Fleig A, Chubanov V. TRPM7. Handb Exp Pharmacol. 2014;222:521-546. doi:10.1007/978-3-642-54215-2_21

Franklin RJ, Gilson JM, Blakemore WF. Local recruitment of remyelinating cells in the repair of demyelination in the central nervous system. J Neurosci Res. 1997;50(2):337-344. doi:10.1002/(SICI)1097-4547(19971015)50:2<337::AID-JNR21>3.0.CO;2-3

Fricker D, Miles R. EPSP amplification and the precision of spike timing in hippocampal neurons. Neuron. 2000;28(2):559-569. doi:10.1016/s0896-6273(00)00133-1

Fröhlich N, Nagy B, Hovhannisyan A, Kukley M. Fate of neuron-glia synapses during proliferation and differentiation of NG2 cells. J Anat. 2011;219(1):18-32. doi:10.1111/j.1469-7580.2011.01392.x

Fuerst PG, Koizumi A, Masland RH, Burgess RW. Neurite arborization and mosaic spacing in the mouse retina require DSCAM. Nature. 2008;451(7177):470-474. doi:10.1038/nature06514

Fulton D, Paez PM, Fisher R, Handley V, Colwell CS, Campagnoni AT. Regulation of L-type Ca++ currents and process morphology in white matter oligodendrocyte precursor cells by golli-myelin proteins. Glia. 2010;58(11):1292-1303. doi:10.1002/glia.21008

Fusco FR, Martorana A, Giampà C, et al. Cellular localization of TRPC3 channel in rat brain: preferential distribution to oligodendrocytes. Neurosci Lett. 2004;365(2):137-142. doi:10.1016/j.neulet.2004.04.070

Gallo V, Zhou JM, McBain CJ, Wright P, Knutson PL, Armstrong RC. Oligodendrocyte progenitor cell proliferation and lineage progression are regulated by glutamate receptor-mediated K+ channel block. J Neurosci. 1996;16(8):2659-2670. doi:10.1523/JNEUROSCI.16-08-02659.1996

Gallo V, Mangin JM, Kukley M, Dietrich D. Synapses on NG2-expressing progenitors in the brain: multiple functions?. J Physiol. 2008;586(16):3767-3781. doi:10.1113/jphysiol.2008.158436

Gan Q, Watanabe S. Synaptic Vesicle Endocytosis in Different Model Systems. Front Cell Neurosci. 2018;12:171. Published 2018 Jun 28. doi:10.3389/fncel.2018.00171

Gautier HO, Evans KA, Volbracht K, et al. Neuronal activity regulates remyelination via glutamate signalling to oligodendrocyte progenitors. Nat Commun. 2015;6:8518. Published 2015 Oct 6. doi:10.1038/ncomms9518

Ge WP, Yang XJ, Zhang Z, et al. Long-term potentiation of neuron-glia synapses mediated by Ca2+-permeable AMPA receptors. Science. 2006;312(5779):1533-1537. doi:10.1126/science.1124669

Ge WP, Zhou W, Luo Q, Jan LY, Jan YN. Dividing glial cells maintain differentiated properties including complex morphology and functional synapses. Proc Natl Acad Sci U S A. 2009;106(1):328-333. doi:10.1073/pnas.0811353106

Geha S, Pallud J, Junier MP, et al. NG2+/Olig2+ cells are the major cycle-related cell population of the adult human normal brain. Brain Pathol. 2010;20(2):399-411. doi:10.1111/j.1750-3639.2009.00295.x

Ghiani CA, Yuan X, Eisen AM, et al. Voltage-activated K+ channels and membrane depolarization regulate accumulation of the cyclin-dependent kinase inhibitors p27(Kip1) and p21(CIP1) in glial progenitor cells. J Neurosci. 1999;19(13):5380-5392. doi:10.1523/JNEUROSCI.19-13-05380.1999

Gibson EM, Purger D, Mount CW, et al. Neuronal activity promotes oligodendrogenesis and adaptive myelination in the mammalian brain. Science. 2014;344(6183):1252304. doi:10.1126/science.1252304

Gilbert P, Kettenmann H, Schachner M. gamma-Aminobutyric acid directly depolarizes cultured oligodendrocytes. J Neurosci. 1984;4(2):561-569. doi:10.1523/JNEUROSCI.04-02-00561.1984

Greger IH, Watson JF, Cull-Candy SG. Structural and Functional Architecture of AMPA-Type Glutamate Receptors and Their Auxiliary Proteins. Neuron. 2017;94(4):713-730. doi:10.1016/j.neuron.2017.04.009

Guo F, Ma J, McCauley E, Bannerman P, Pleasure D. Early postnatal proteolipid promoter-expressing progenitors produce multilineage cells in vivo. J Neurosci. 2009;29(22):7256-7270. doi:10.1523/JNEUROSCI.5653-08.2009

Guo F, Maeda Y, Ma J, et al. Pyramidal neurons are generated from oligodendroglial progenitor cells in adult piriform cortex. J Neurosci. 2010;30(36):12036-12049. doi:10.1523/JNEUROSCI.1360-10.2010

Gupta RK, Kanungo M. Glial molecular alterations with mouse brain development and aging: up-regulation of the Kir4.1 and aquaporin-4. Age (Dordr). 2013;35(1):59-67. doi:10.1007/s11357-011-9330-5

Gustafsson B, Asztely F, Hanse E, Wigström H. Onset Characteristics of Long-Term Potentiation in the Guinea-Pig Hippocampal CA1 Region in Vitro. Eur J Neurosci. 1989;1(4):382-394. doi:10.1111/j.1460-9568.1989.tb00803.x

Haberlandt C, Derouiche A, Wyczynski A, et al. Gray matter NG2 cells display multiple Ca2+-signaling pathways and highly motile processes. PLoS One. 2011;6(3):e17575. Published 2011 Mar 24. doi:10.1371/journal.pone.0017575

Hamilton N, Vayro S, Wigley R, Butt AM. Axons and astrocytes release ATP and glutamate to evoke calcium signals in NG2-glia. Glia. 2010;58(1):66-79. doi:10.1002/glia.20902

Harris KM, Weinberg RJ. Ultrastructure of synapses in the mammalian brain. Cold Spring Harb Perspect Biol. 2012;4(5):a005587. Published 2012 May 1. doi:10.1101/cshperspect.a005587

Hartveit E, Veruki ML. Studying properties of neurotransmitter receptors by non-stationary noise analysis of spontaneous postsynaptic currents and agonist-evoked responses in outside-out patches. Nat Protoc. 2007;2(2):434-448. doi:10.1038/nprot.2007.47

Hibino H, Fujita A, Iwai K, Yamada M, Kurachi Y. Differential assembly of inwardly rectifying K+ channel subunits, Kir4.1 and Kir5.1, in brain astrocytes. J Biol Chem. 2004;279(42):44065-44073. doi:10.1074/jbc.M405985200

Hirbec H, Perestenko O, Nishimune A, et al. The PDZ proteins PICK1, GRIP, and syntenin bind multiple glutamate receptor subtypes. Analysis of PDZ binding motifs. J Biol Chem. 2002;277(18):15221-15224. doi:10.1074/jbc.C200112200

Hirbec H, Martin S, Henley JM. Syntenin is involved in the developmental regulation of neuronal membrane architecture. Mol Cell Neurosci. 2005;28(4):737-746. doi:10.1016/j.mcn.2004.12.005

Hoffman DA, Magee JC, Colbert CM, Johnston D. K+ channel regulation of signal propagation in dendrites of hippocampal pyramidal neurons. Nature. 1997;387(6636):869-875. doi:10.1038/43119

Hoffmann A, Grimm C, Kraft R, et al. TRPM3 is expressed in sphingosine-responsive myelinating oligodendrocytes. J Neurochem. 2010;114(3):654-665. doi:10.1111/j.1471-4159.2010.06644.x

Holbro N, Grunditz A, Oertner TG. Differential distribution of endoplasmic reticulum controls metabotropic signaling and plasticity at hippocampal synapses. Proc Natl Acad Sci U S A. 2009;106(35):15055-15060. doi:10.1073/pnas.0905110106

Holtzclaw LA, Gallo V, Russell JT. AMPA receptors shape Ca2+ responses in cortical oligodendrocyte progenitors and CG-4 cells. J Neurosci Res. 1995;42(1):124-130. doi:10.1002/jnr.490420114

Horner PJ, Power AE, Kempermann G, et al. Proliferation and differentiation of progenitor cells throughout the intact adult rat spinal cord. J Neurosci. 2000;20(6):2218-2228. doi:10.1523/JNEUROSCI.20-06-02218.2000

Horner PJ, Thallmair M, Gage FH. Defining the NG2-expressing cell of the adult CNS. J Neurocytol. 2002;31(6-7):469-480. doi:10.1023/a:1025739630398

Hosokawa T, Mitsushima D, Kaneko R, Hayashi Y. Stoichiometry and phosphoisotypes of hippocampal AMPA-type glutamate receptor phosphorylation. Neuron. 2015;85(1):60-67. doi:10.1016/j.neuron.2014.11.026

Hu H, Vervaeke K, Storm JF. Two forms of electrical resonance at theta frequencies, generated by M-current, h-current and persistent Na+ current in rat hippocampal pyramidal cells. J Physiol. 2002;545(3):783-805. doi:10.1113/jphysiol.2002.029249

Hughes AN, Appel B. Oligodendrocytes express synaptic proteins that modulate myelin sheath formation. Nat Commun. 2019;10(1):4125. Published 2019 Sep 11. doi:10.1038/s41467-019-12059-y

Husi H, Ward MA, Choudhary JS, Blackstock WP, Grant SG. Proteomic analysis of NMDA receptor-adhesion protein signaling complexes. Nat Neurosci. 2000;3(7):661-669. doi:10.1038/76615

Jabs R, Pivneva T, Hüttmann K, et al. Synaptic transmission onto hippocampal glial cells with hGFAP promoter activity. J Cell Sci. 2005;118(Pt 16):3791-3803. doi:10.1242/jcs.02515

Jentsch TJ. CLC chloride channels and transporters: from genes to protein structure, pathology and physiology. Crit Rev Biochem Mol Biol. 2008;43(1):3-36. doi:10.1080/10409230701829110

Jin X, Riew TR, Kim HL, Choi JH, Lee MY. Morphological characterization of NG2 glia and their association with neuroglial cells in the 3-nitropropionic acid-lesioned striatum of rat. Sci Rep. 2018;8(1):5942. Published 2018 Apr 13. doi:10.1038/s41598-018-24385-0

Kaksonen M, Roux A. Mechanisms of clathrin-mediated endocytosis. Nat Rev Mol Cell Biol. 2018;19(5):313-326. doi:10.1038/nrm.2017.132

Kalsi AS, Greenwood K, Wilkin G, Butt AM. Kir4.1 expression by astrocytes and oligodendrocytes in CNS white matter: a developmental study in the rat optic nerve. J Anat. 2004;204(6):475-485. doi:10.1111/j.0021-8782.2004.00288.x

Kang SH, Fukaya M, Yang JK, Rothstein JD, Bergles DE. NG2+ CNS glial progenitors remain committed to the oligodendrocyte lineage in postnatal life and following neurodegeneration. Neuron. 2010;68(4):668-681. doi:10.1016/j.neuron.2010.09.009

Káradóttir R, Attwell D. Neurotransmitter receptors in the life and death of oligodendrocytes. Neuroscience. 2007;145(4):1426-1438. doi:10.1016/j.neuroscience.2006.08.070

Káradóttir R, Cavelier P, Bergersen LH, Attwell D. NMDA receptors are expressed in oligodendrocytes and activated in ischaemia. Nature. 2005;438(7071):1162-1166. doi:10.1038/nature04302

Káradóttir R, Hamilton NB, Bakiri Y, Attwell D. Spiking and nonspiking classes of oligodendrocyte precursor glia in CNS white matter. Nat Neurosci. 2008;11(4):450-456. doi:10.1038/nn2060

Kay JN, Chu MW, Sanes JR. MEGF10 and MEGF11 mediate homotypic interactions required for mosaic spacing of retinal neurons. Nature. 2012;483(7390):465-469. Published 2012 Mar 11. doi:10.1038/nature10877

Kessaris N, Fogarty M, Iannarelli P, Grist M, Wegner M, Richardson WD. Competing waves of oligodendrocytes in the forebrain and postnatal elimination of an embryonic lineage. Nat Neurosci. 2006;9(2):173-179. doi:10.1038/nn1620

Kettenmann H, Gilbert P, Schachner M. Depolarization of cultured oligodendrocytes by glutamate and GABA. Neurosci Lett. 1984;47(3):271-276. doi:10.1016/0304-3940(84)90525-1

Kettenmann H, Blankenfeld GV, Trotter J. Physiological properties of oligodendrocytes during development. Ann N Y Acad Sci. 1991;633:64-77. doi:10.1111/j.1749-6632.1991.tb15596.x

Kim E, Sheng M. PDZ domain proteins of synapses. Nat Rev Neurosci. 2004;5(10):771-781. doi:10.1038/nrn1517

Kirby L, Jin J, Cardona JG, et al. Oligodendrocyte precursor cells present antigen and are cytotoxic targets in inflammatory demyelination. Nat Commun. 2019;10(1):3887. Published 2019 Aug 29. doi:10.1038/s41467-019-11638-3

Knutson P, Ghiani CA, Zhou JM, Gallo V, McBain CJ. K+ channel expression and cell proliferation are regulated by intracellular sodium and membrane depolarization in oligodendrocyte progenitor cells. J Neurosci. 1997;17(8):2669-2682. doi:10.1523/JNEUROSCI.17-08-02669.1997

Kofuji P, Ceelen P, Zahs KR, Surbeck LW, Lester HA, Newman EA. Genetic inactivation of an inwardly rectifying potassium channel (Kir4.1 subunit) in mice: phenotypic impact in retina. J Neurosci. 2000;20(15):5733-5740. doi:10.1523/JNEUROSCI.20-15-05733.2000

Kougioumtzidou E, Shimizu T, Hamilton NB, et al. Signalling through AMPA receptors on oligodendrocyte precursors promotes myelination by enhancing oligodendrocyte survival. Elife. 2017;6:e28080. Published 2017 Jun 13. doi:10.7554/eLife.28080

Krapivinsky G, Medina I, Krapivinsky L, Gapon S, Clapham DE. SynGAP-MUPP1-CaMKII synaptic complexes regulate p38 MAP kinase activity and NMDA receptor-dependent synaptic AMPA receptor potentiation. Neuron. 2004;43(4):563-574. doi:10.1016/j.neuron.2004.08.003

Kressin K, Kuprijanova E, Jabs R, Seifert G, Steinhäuser C. Developmental regulation of Na+ and K+ conductances in glial cells of mouse hippocampal brain slices. Glia. 1995;15(2):173-187. doi:10.1002/glia.440150210

Kukley M, Dietrich D. Kainate receptors and signal integration by NG2 glial cells. Neuron Glia Biol. 2009;5(1-2):13-20. doi:10.1017/S1740925X09990081

Kukley M, Capetillo-Zarate E, Dietrich D. Vesicular glutamate release from axons in white matter. Nat Neurosci. 2007;10(3):311-320. doi:10.1038/nn1850

Kukley M, Kiladze M, Tognatta R, et al. Glial cells are born with synapses. FASEB J. 2008;22(8):2957-2969. doi:10.1096/fj.07-090985

Kukley M, Nishiyama A, Dietrich D. The fate of synaptic input to NG2 glial cells: neurons specifically downregulate transmitter release onto differentiating oligodendroglial cells. J Neurosci. 2010;30(24):8320-8331. doi:10.1523/JNEUROSCI.0854-10.2010

Kula B, Chen TJ, Kukley M. Glutamatergic signaling between neurons and oligodendrocyte lineage cells: Is it synaptic or non-synaptic?. Glia. 2019;67(11):2071-2091. doi:10.1002/glia.23617

Kung LH, Gong K, Adedoyin M, et al. Evidence for glutamate as a neuroglial transmitter within sensory ganglia. PLoS One. 2013;8(7):e68312. Published 2013 Jul 2. doi:10.1371/journal.pone.0068312

Larson VA, Zhang Y, Bergles DE. Electrophysiological properties of NG2(+) cells: Matching physiological studies with gene expression profiles. Brain Res. 2016;1638(Pt B):138-160. doi:10.1016/j.brainres.2015.09.010

Lasiene J, Matsui A, Sawa Y, Wong F, Horner PJ. Age-related myelin dynamics revealed by increased oligodendrogenesis and short internodes. Aging Cell. 2009;8(2):201-213. doi:10.1111/j.1474-9726.2009.00462.x

Lefebvre JL, Kostadinov D, Chen WV, Maniatis T, Sanes JR. Protocadherins mediate dendritic self-avoidance in the mammalian nervous system. Nature. 2012;488(7412):517-521. doi:10.1038/nature11305

Leguey I, Bielza C, Larrañaga P, et al. Dendritic branching angles of pyramidal cells across layers of the juvenile rat somatosensory cortex. J Comp Neurol. 2016;524(13):2567-2576. doi:10.1002/cne.23977

Lei S, Czerwinska E, Czerwinski W, Walsh MP, MacDonald JF. Regulation of NMDA receptor activity by F-actin and myosin light chain kinase. J Neurosci. 2001;21(21):8464-8472. doi:10.1523/JNEUROSCI.21-21-08464.2001

Levine JM, Card JP. Light and electron microscopic localization of a cell surface antigen (NG2) in the rat cerebellum: association with smooth protoplasmic astrocytes. J Neurosci. 1987;7(9):2711-2720. doi:10.1523/JNEUROSCI.07-09-02711.1987

Levison SW, Young GM, Goldman JE. Cycling cells in the adult rat neocortex preferentially generate oligodendroglia. J Neurosci Res. 1999;57(4):435-446.

Li C, Xiao L, Liu X, et al. A functional role of NMDA receptor in regulating the differentiation of oligodendrocyte precursor cells and remyelination. Glia. 2013;61(5):732-749. doi:10.1002/glia.22469

Li J, Miramontes T, Czopka T, Monk K. Synapses and Ca2+ activity in oligodendrocyte precursor cells predict where myelin sheaths form. bioRxiv 2022.03.18.484955; doi: https://doi.org/10.1101/2022.03.18.484955

Li J, Miramontes T, Czopka T, Monk K. Synapses and Ca2+ activity in oligodendrocyte precursor cells predict where myelin sheaths form. BioRxiv 2022.03.18.484955; doi: https://doi.org/10.1101/2022.03.18.484955

Lin SC, Bergles DE. Physiological characteristics of NG2-expressing glial cells. J Neurocytol. 2002;31(6-7):537-549. doi:10.1023/a:1025799816285

Lin SC, Bergles DE. Synaptic signaling between GABAergic interneurons and oligodendrocyte precursor cells in the hippocampus. Nat Neurosci. 2004;7(1):24-32. doi:10.1038/nn1162

Lin SC, Bergles DE. Synaptic signaling between neurons and glia. Glia. 2004;47(3):290-298. doi:10.1002/glia.20060

Lin SC, Huck JH, Roberts JD, Macklin WB, Somogyi P, Bergles DE. Climbing fiber innervation of NG2-expressing glia in the mammalian cerebellum. Neuron. 2005;46(5):773-785. doi:10.1016/j.neuron.2005.04.025

Lin SC, Huck JH, Roberts JD, Macklin WB, Somogyi P, Bergles DE. Climbing fiber innervation of NG2-expressing glia in the mammalian cerebellum. Neuron. 2005;46(5):773-785. doi:10.1016/j.neuron.2005.04.025

Lisman J, Schulman H, Cline H. The molecular basis of CaMKII function in synaptic and behavioural memory. Nat Rev Neurosci. 2002;3(3):175-190. doi:10.1038/nrn753

Lisman J. Glutamatergic synapses are structurally and biochemically complex because of multiple plasticity processes: long-term potentiation, long-term depression, short-term potentiation and scaling. Philos Trans R Soc Lond B Biol Sci. 2017;372(1715):20160260. doi:10.1098/rstb.2016.0260

Llinás R, Sugimori M, Silver RB. Microdomains of high calcium concentration in a presynaptic terminal. Science. 1992;256(5057):677-679. doi:10.1126/science.1350109

Losonczy A, Magee JC. Integrative properties of radial oblique dendrites in hippocampal CA1 pyramidal neurons. Neuron. 2006;50(2):291-307. doi:10.1016/j.neuron.2006.03.016

Lujan R, Nusser Z, Roberts JD, Shigemoto R, Somogyi P. Perisynaptic location of metabotropic glutamate receptors mGluR1 and mGluR5 on dendrites and dendritic spines in the rat hippocampus. Eur J Neurosci. 1996;8(7):1488-1500. doi:10.1111/j.1460-9568.1996.tb01611.x

Luyt K, Varadi A, Molnar E. Functional metabotropic glutamate receptors are expressed in oligodendrocyte progenitor cells. J Neurochem. 2003;84(6):1452-1464. doi:10.1046/j.1471-4159.2003.01661.x

Luyt K, Váradi A, Durant CF, Molnár E. Oligodendroglial metabotropic glutamate receptors are developmentally regulated and involved in the prevention of apoptosis. J Neurochem. 2006;99(2):641-656. doi:10.1111/j.1471-4159.2006.04103.x

Makara JK, Rappert A, Matthias K, Steinhäuser C, Spät A, Kettenmann H. Astrocytes from mouse brain slices express ClC-2- mediated Cl- currents regulated during development and after injury. Mol Cell Neurosci. 2003;23(4):521-530. doi:10.1016/s1044-7431(03)00080-0

Maldonado PP, Vélez-Fort M, Levavasseur F, Angulo MC. Oligodendrocyte precursor cells are accurate sensors of local K+ in mature gray matter. J Neurosci. 2013;33(6):2432-2442. doi:10.1523/JNEUROSCI.1961-12.2013

Maldonado PP, Vélez-Fort M, Angulo MC. Is neuronal communication with NG2 cells synaptic or extrasynaptic?. J Anat. 2011;219(1):8-17. doi:10.1111/j.1469-7580.2011.01350.x

Mangin JM, Kunze A, Chittajallu R, Gallo V. Satellite NG2 progenitor cells share common glutamatergic inputs with associated interneurons in the mouse dentate gyrus. J Neurosci. 2008;28(30):7610-7623. doi:10.1523/JNEUROSCI.1355-08.2008

Mangin JM, Li P, Scafidi J, Gallo V. Experience-dependent regulation of NG2 progenitors in the developing barrel cortex. Nat Neurosci. 2012;15(9):1192-1194. doi:10.1038/nn.3190

Marques S, Zeisel A, Codeluppi S, et al. Oligodendrocyte heterogeneity in the mouse juvenile and adult central nervous system. Science. 2016;352(6291):1326-1329. doi:10.1126/science.aaf6463

Massie A, Boillée S, Hewett S, Knackstedt L, Lewerenz J. Main path and byways: non-vesicular glutamate release by system xc(-) as an important modifier of glutamatergic neurotransmission. J Neurochem. 2015;135(6):1062-1079. doi:10.1111/jnc.13348

Matsui K, Jahr CE. Ectopic release of synaptic vesicles. Neuron. 2003;40(6):1173-1183. doi:10.1016/s0896-6273(03)00788-8

Matveev V, Zucker RS, Sherman A. Facilitation through buffer saturation: constraints on endogenous buffering properties. Biophys J. 2004;86(5):2691-2709. doi:10.1016/S0006-3495(04)74324-6

Meinrenken CJ, Borst JG, Sakmann B. Calcium secretion coupling at calyx of Held governed by nonuniform channel-vesicle topography. J Neurosci. 2002;22(5):1648-1667. doi:10.1523/JNEUROSCI.22-05-01648.2002

Mintz IM, Sabatini BL, Regehr WG. Calcium control of transmitter release at a cerebellar synapse. Neuron. 1995;15(3):675-688. doi:10.1016/0896-6273(95)90155-8

Mori T, Wakabayashi T, Takamori Y, Kitaya K, Yamada H. Phenotype analysis and quantification of proliferating cells in the cortical gray matter of the adult rat. Acta Histochem Cytochem. 2009;42(1):1-8. doi:10.1267/ahc.08037

Moura DMS, Brennan EJ, Brock R, Cocas LA. Neuron to Oligodendrocyte Precursor Cell Synapses: Protagonists in Oligodendrocyte Development and Myelination, and Targets for Therapeutics. Front Neurosci. 2022;15:779125. Published 2022 Jan 18. doi:10.3389/fnins.2021.779125

Müller J, Reyes-Haro D, Pivneva T, et al. The principal neurons of the medial nucleus of the trapezoid body and NG2(+) glial cells receive coordinated excitatory synaptic input. J Gen Physiol. 2009;134(2):115-127. doi:10.1085/jgp.200910194

Müller J, Reyes-Haro D, Pivneva T, et al. The principal neurons of the medial nucleus of the trapezoid body and NG2(+) glial cells receive coordinated excitatory synaptic input. J Gen Physiol. 2009;134(2):115-127. doi:10.1085/jgp.200910194

Nagy B, Hovhannisyan A, Barzan R, Chen TJ, Kukley M. Different patterns of neuronal activity trigger distinct responses of oligodendrocyte precursor cells in the corpus callosum. PLoS Biol. 2017;15(8):e2001993. Published 2017 Aug 22. doi:10.1371/journal.pbio.2001993

Neusch C, Rozengurt N, Jacobs RE, Lester HA, Kofuji P. Kir4.1 potassium channel subunit is crucial for oligodendrocyte development and in vivo myelination. J Neurosci. 2001;21(15):5429-5438. doi:10.1523/JNEUROSCI.21-15-05429.2001

Neusch C, Papadopoulos N, Müller M, et al. Lack of the Kir4.1 channel subunit abolishes K+ buffering properties of astrocytes in the ventral respiratory group: impact on extracellular K+ regulation [published correction appears in J Neurophysiol. 2006 Aug;96(2):965]. J Neurophysiol. 2006;95(3):1843-1852. doi:10.1152/jn.00996.2005

Nimmerjahn A, Kirchhoff F, Helmchen F. Resting microglial cells are highly dynamic surveillants of brain parenchyma in vivo. Science. 2005;308(5726):1314-1318. doi:10.1126/science.1110647

Nishiyama A, Lin XH, Giese N, Heldin CH, Stallcup WB. Co-localization of NG2 proteoglycan and PDGF alpha-receptor on O2A progenitor cells in the developing rat brain. J Neurosci Res. 1996;43(3):299-314. doi:10.1002/(SICI)1097-4547(19960201)43:3<299::AID-JNR5>3.0.CO;2-E

Nishiyama A, Yu M, Drazba JA, Tuohy VK. Normal and reactive NG2+ glial cells are distinct from resting and activated microglia. J Neurosci Res. 1997;48(4):299-312. doi:10.1002/(sici)1097-4547(19970515)48:4<299::aid-jnr2>3.0.co;2-6

Nishiyama A, Watanabe M, Yang Z, Bu J. Identity, distribution, and development of polydendrocytes: NG2-expressing glial cells. J Neurocytol. 2002;31(6-7):437-455. doi:10.1023/a:1025783412651

Nishiyama A, Yang Z, Butt A. Astrocytes and NG2-glia: what's in a name?. J Anat. 2005;207(6):687-693. doi:10.1111/j.1469-7580.2005.00489.x

Nishiyama A, Komitova M, Suzuki R, Zhu X. Polydendrocytes (NG2 cells): multifunctional cells with lineage plasticity. Nat Rev Neurosci. 2009;10(1):9-22. doi:10.1038/nrn2495

Niswender CM, Conn PJ. Metabotropic glutamate receptors: physiology, pharmacology, and disease. Annu Rev Pharmacol Toxicol. 2010;50:295-322. doi:10.1146/annurev.pharmtox.011008.145533

Notomi T, Shigemoto R. Immunohistochemical localization of Ih channel subunits, HCN1-4, in the rat brain. J Comp Neurol. 2004;471(3):241-276. doi:10.1002/cne.11039

Nwaobi SE, Lin E, Peramsetty SR, Olsen ML. DNA methylation functions as a critical regulator of Kir4.1 expression during CNS development. Glia. 2014;62(3):411-427. doi:10.1002/glia.22613

Osterstock G, Le Bras B, Arulkandarajah KH, et al. Axoglial synapses are formed onto pioneer oligodendrocyte precursor cells at the onset of spinal cord gliogenesis. Glia. 2018;66(8):1678-1694. doi:10.1002/glia.23331

Ozerdem U, Grako KA, Dahlin-Huppe K, Monosov E, Stallcup WB. NG2 proteoglycan is expressed exclusively by mural cells during vascular morphogenesis. Dev Dyn. 2001;222(2):218-227. doi:10.1002/dvdy.1200

Paez PM, Fulton DJ, Spreur V, Handley V, Campagnoni AT. Multiple kinase pathways regulate voltage-dependent Ca2+ influx and migration in oligodendrocyte precursor cells. J Neurosci. 2010;30(18):6422-6433. doi:10.1523/JNEUROSCI.5086- 09.2010

Paez PM, Fulton D, Spreuer V, Handley V, Campagnoni AT. Modulation of canonical transient receptor potential channel 1 in the proliferation of oligodendrocyte precursor cells by the golli products of the myelin basic protein gene. J Neurosci. 2011;31(10):3625-3637. doi:10.1523/JNEUROSCI.4424-10.2011

Panagiotakos G, Alshamy G, Chan B, et al. Long-term impact of radiation on the stem cell and oligodendrocyte precursors in the brain. PLoS One. 2007;2(7):e588. Published 2007 Jul 11. doi:10.1371/journal.pone.0000588

Papouin T, Oliet SH. Organization, control and function of extrasynaptic NMDA receptors. Philos Trans R Soc Lond B Biol Sci. 2014;369(1654):20130601. doi:10.1098/rstb.2013.0601

Parri HR, Gould TM, Crunelli V. Sensory and cortical activation of distinct glial cell subtypes in the somatosensory thalamus of young rats. Eur J Neurosci. 2010;32(1):29-40. doi:10.1111/j.1460-9568.2010.07281.x

Passlick S, Trotter J, Seifert G, Steinhäuser C, Jabs R. The NG2 Protein Is Not Required for Glutamatergic Neuron-NG2 Cell Synaptic Signaling. Cereb Cortex. 2016;26(1):51-57. doi:10.1093/cercor/bhu171

Patneau DK, Wright PW, Winters C, Mayer ML, Gallo V. Glial cells of the oligodendrocyte lineage express both kainate- and AMPA-preferring subtypes of glutamate receptor. Neuron. 1994;12(2):357-371. doi:10.1016/0896-6273(94)90277-1

Pende M, Holtzclaw LA, Curtis JL, Russell JT, Gallo V. Glutamate regulates intracellular calcium and gene expression in oligodendrocyte progenitors through the activation of DL-alpha-amino-3-hydroxy-5-methyl-4-isoxazolepropionic acid receptors. Proc Natl Acad Sci U S A. 1994;91(8):3215-3219. doi:10.1073/pnas.91.8.3215

Pernía-Andrade AJ, Goswami SP, Stickler Y, Fröbe U, Schlögl A, Jonas P. A deconvolution-based method with high sensitivity and temporal resolution for detection of spontaneous synaptic currents in vitro and in vivo. Biophys J. 2012;103(7):1429-1439. doi:10.1016/j.bpj.2012.08.039

Peters HC, Hu H, Pongs O, Storm JF, Isbrandt D. Conditional transgenic suppression of M channels in mouse brain reveals functions in neuronal excitability, resonance and behavior. Nat Neurosci. 2005;8(1):51-60. doi:10.1038/nn1375

Polito A, Reynolds R. NG2-expressing cells as oligodendrocyte progenitors in the normal and demyelinated adult central nervous system. J Anat. 2005;207(6):707-716. doi:10.1111/j.1469-7580.2005.00454.x

Psachoulia K, Jamen F, Young KM, Richardson WD. Cell cycle dynamics of NG2 cells in the postnatal and ageing brain. Neuron Glia Biol. 2009;5(3-4):57-67. doi:10.1017/S1740925X09990354

Regehr WG. Short-term presynaptic plasticity. Cold Spring Harb Perspect Biol. 2012;4(7):a005702. Published 2012 Jul 1. doi:10.1101/cshperspect.a005702

Reimann F, Ashcroft FM. Inwardly rectifying potassium channels. Curr Opin Cell Biol. 1999;11(4):503-508. doi:10.1016/S0955-0674(99)80073-8

Reiner A, Levitz J. Glutamatergic Signaling in the Central Nervous System: Ionotropic and Metabotropic Receptors in Concert. Neuron. 2018;98(6):1080-1098. doi:10.1016/j.neuron.2018.05.018

Rieger A, Deitmer JW, Lohr C. Axon-glia communication evokes calcium signaling in olfactory ensheathing cells of the developing olfactory bulb. Glia. 2007;55(4):352-359. doi:10.1002/glia.20460

Rivers LE, Young KM, Rizzi M, et al. PDGFRA/NG2 glia generate myelinating oligodendrocytes and piriform projection neurons in adult mice. Nat Neurosci. 2008;11(12):1392-1401. doi:10.1038/nn.2220

Rizo J, Südhof TC. The membrane fusion enigma: SNAREs, Sec1/Munc18 proteins, and their accomplices--guilty as charged?. Annu Rev Cell Dev Biol. 2012;28:279-308. doi:10.1146/annurev-cellbio-101011-155818

Rizzoli SO, Betz WJ. Synaptic vesicle pools. Nat Rev Neurosci. 2005;6(1):57-69. doi:10.1038/nrn1583

Rojo C, Leguey I, Kastanauskaite A, et al. Laminar Differences in Dendritic Structure of Pyramidal Neurons in the Juvenile Rat Somatosensory Cortex. Cereb Cortex. 2016;26(6):2811-2822. doi:10.1093/cercor/bhv316

Rosenmund C, Stevens CF. Definition of the readily releasable pool of vesicles at hippocampal synapses. Neuron. 1996;16(6):1197-1207. doi:10.1016/s0896-6273(00)80146-4

Rosenmund C, Rettig J, Brose N. Molecular mechanisms of active zone function. Curr Opin Neurobiol. 2003;13(5):509-519. doi:10.1016/j.conb.2003.09.011

Routh BN, Johnston D, Harris K, Chitwood RA. Anatomical and electrophysiological comparison of CA1 pyramidal neurons of the rat and mouse. J Neurophysiol. 2009;102(4):2288-2302. doi:10.1152/jn.00082.2009

Rozov A, Zilberter Y, Wollmuth LP, Burnashev N. Facilitation of currents through rat Ca2+-permeable AMPA receptor channels by activity-dependent relief from polyamine block. J Physiol. 1998;511 (Pt 2)(Pt 2):361-377. doi:10.1111/j.1469-7793.1998.361bh.x

Rusakov DA, Kullmann DM. Extrasynaptic glutamate diffusion in the hippocampus: ultrastructural constraints, uptake, and receptor activation. J Neurosci. 1998;18(9):3158-3170. doi:10.1523/JNEUROSCI.18-09-03158.1998

Saab AS, Tzvetavona ID, Trevisiol A, et al. Oligodendroglial NMDA Receptors Regulate Glucose Import and Axonal Energy Metabolism. Neuron. 2016;91(1):119-132. doi:10.1016/j.neuron.2016.05.016

Sahel A, Ortiz FC, Kerninon C, Maldonado PP, Angulo MC, Nait-Oumesmar B. Alteration of synaptic connectivity of oligodendrocyte precursor cells following demyelination. Front Cell Neurosci. 2015;9:77. Published 2015 Mar 17. doi:10.3389/fncel.2015.00077

Sakaba T, Neher E. Calmodulin mediates rapid recruitment of fast-releasing synaptic vesicles at a calyx-type synapse. Neuron. 2001;32(6):1119-1131. doi:10.1016/s0896-6273(01)00543-8

Sanderson DJ, Good MA, Skelton K, et al. Enhanced long-term and impaired short-term spatial memory in GluA1 AMPA receptor subunit knockout mice: evidence for a dual-process memory model [published correction appears in Learn Mem. 2009;16(8):508]. Learn Mem. 2009;16(6):379-386. Published 2009 May 23. doi:10.1101/lm.1339109

Sanes HD, Reh AT, Harris WA, Landgraf M, Chapter 8 - Synapse Formation, Editor(s): Sanes HD, Reh AT, Harris WA, Landgraf M, Development of the Nervous System (Fourth Edition), Academic Press, 2019, Pages 227-267, ISBN 9780128039960, https://doi.org/10.1016/B978-0-12-803996-0.00008-3.

Santoro B, Chen S, Luthi A, et al. Molecular and functional heterogeneity of hyperpolarization-activated pacemaker channels in the mouse CNS. J Neurosci. 2000;20(14):5264-5275. doi:10.1523/JNEUROSCI.20-14-05264.2000

Sattler R, Xiong Z, Lu WY, MacDonald JF, Tymianski M. Distinct roles of synaptic and extrasynaptic NMDA receptors in excitotoxicity. J Neurosci. 2000;20(1):22-33. doi:10.1523/JNEUROSCI.20-01-00022.2000

Savtchouk I, Volterra A. Gliotransmission: Beyond Black-and-White. J Neurosci. 2018;38(1):14-25. doi:10.1523/JNEUROSCI.0017-17.2017

Scanziani M, Salin PA, Vogt KE, Malenka RC, Nicoll RA. Use-dependent increases in glutamate concentration activate presynaptic metabotropic glutamate receptors. Nature. 1997;385(6617):630-634. doi:10.1038/385630a0

Schmidt K, Eulitz D, Veh RW, Kettenmann H, Kirchhoff F. Heterogeneous expression of voltage-gated potassium channels of the shaker family (Kv1) in oligodendrocyte progenitors. Brain Res. 1999;843(1-2):145-160. doi:10.1016/s0006-8993(99)01938-1

Schneggenburger R, Sakaba T, Neher E. Vesicle pools and short-term synaptic depression: lessons from a large synapse. Trends Neurosci. 2002;25(4):206-212. doi:10.1016/s0166-2236(02)02139-2

Schweizer FE, Ryan TA. The synaptic vesicle: cycle of exocytosis and endocytosis. Curr Opin Neurobiol. 2006;16(3):298-304. doi:10.1016/j.conb.2006.05.006

Seifert G, Hüttmann K, Binder DK, et al. Analysis of astroglial K+ channel expression in the developing hippocampus reveals a predominant role of the Kir4.1 subunit. J Neurosci. 2009;29(23):7474-7488. doi:10.1523/JNEUROSCI.3790-08.2009

Shah MM. Cortical HCN channels: function, trafficking and plasticity. J Physiol. 2014;592(13):2711-2719. doi:10.1113/jphysiol.2013.270058

Shen K, Cowan CW. Guidance molecules in synapse formation and plasticity. Cold Spring Harb Perspect Biol. 2010;2(4):a001842. doi:10.1101/cshperspect.a001842

Sheng M, Kim E. The postsynaptic organization of synapses. Cold Spring Harb Perspect Biol. 2011;3(12):a005678. Published 2011 Dec 1. doi:10.1101/cshperspect.a005678

Sheng M, Sala C. PDZ domains and the organization of supramolecular complexes. Annu Rev Neurosci. 2001;24:1-29. doi:10.1146/annurev.neuro.24.1.1

Sherman SM. The function of metabotropic glutamate receptors in thalamus and cortex. Neuroscientist. 2014;20(2):136-149. doi:10.1177/1073858413478490

Sholl DA. Dendritic organization in the neurons of the visual and motor cortices of the cat. J Anat. 1953;87(4):387-406.

Silberberg G, Wu C, Markram H. Synaptic dynamics control the timing of neuronal excitation in the activated neocortical microcircuit. J Physiol. 2004;556(Pt 1):19-27. doi:10.1113/jphysiol.2004.060962

Simpson PB, Armstrong RC. Intracellular signals and cytoskeletal elements involved in oligodendrocyte progenitor migration. Glia. 1999;26(1):22-35.

Soliven B. Calcium signalling in cells of oligodendroglial lineage. Microsc Res Tech. 2001;52(6):672-679. doi:10.1002/jemt.1051

Sontheimer H, Trotter J, Schachner M, Kettenmann H. Channel expression correlates with differentiation stage during the development of oligodendrocytes from their precursor cells in culture. Neuron. 1989;2(2):1135-1145. doi:10.1016/0896-6273(89)90180-3

Spampinato SF, Merlo S, Chisari M, Nicoletti F, Sortino MA. Glial metabotropic glutamate receptor-4 increases maturation and survival of oligodendrocytes. Front Cell Neurosci. 2015;8:462. Published 2015 Jan 14. doi:10.3389/fncel.2014.00462

Spassky N, de Castro F, Le Bras B, et al. Directional guidance of oligodendroglial migration by class 3 semaphorins and netrin-1. J Neurosci. 2002;22(14):5992-6004. doi:10.1523/JNEUROSCI.22-14-05992.2002

Spitzer SO, Sitnikov S, Kamen Y, et al. Oligodendrocyte Progenitor Cells Become Regionally Diverse and Heterogeneous with Age. Neuron. 2019;101(3):459-471.e5. doi:10.1016/j.neuron.2018.12.020

Spruston N, Häusser M, Stuart G, Chapter 11 - Information Processing in Dendrites and Spines, Editor(s): Larry R. Squire, Darwin Berg, Floyd E. Bloom, Sascha du Lac, Anirvan Ghosh, Nicholas C. Spitzer, Fundamental Neuroscience (Fourth Edition), Academic Press, 2013, Pages 231-260, ISBN 9780123858702, https://doi.org/10.1016/B978-0-12-385870-2.00011-1

Stallcup WB, Beasley L. Bipotential glial precursor cells of the optic nerve express the NG2 proteoglycan. J Neurosci. 1987;7(9):2737-2744. doi:10.1523/JNEUROSCI.07-09-02737.1987

Stegmüller J, Werner H, Nave KA, Trotter J. The proteoglycan NG2 is complexed with alpha-amino-3-hydroxy-5-methyl-4-isoxazolepropionic acid (AMPA) receptors by the PDZ glutamate receptor interaction protein (GRIP) in glial progenitor cells. Implications for glial-neuronal signaling. J Biol Chem. 2003;278(6):3590-3598. doi:10.1074/jbc.M210010200

Steinhäuser C, Berger T, Frotscher M, Kettenmann H. Heterogeneity in the Membrane Current Pattern of Identified Glial Cells in the Hippocampal Slice. Eur J Neurosci. 1992;4(6):472-484. doi:10.1111/j.1460-9568.1992.tb00897.x

Steinhäuser C, Jabs R, Kettenmann H. Properties of GABA and glutamate responses in identified glial cells of the mouse hippocampal slice. Hippocampus. 1994;4(1):19-35. doi:10.1002/hipo.450040105

Stubblefield EA, Benke TA. Distinct AMPA-type glutamatergic synapses in developing rat CA1 hippocampus. J Neurophysiol. 2010;104(4):1899-1912. doi:10.1152/jn.00099.2010

Südhof TC. Synaptotagmins: why so many?. J Biol Chem. 2002;277(10):7629-7632. doi:10.1074/jbc.R100052200

Sudhof TC. The synaptic vesicle cycle. Annu Rev Neurosci. 2004;27:509-547. doi:10.1146/annurev.neuro.26.041002.131412

Sun W, Dietrich D. Synaptic integration by NG2 cells. Front Cell Neurosci. 2013;7:255. Published 2013 Dec 20. doi:10.3389/fncel.2013.00255

Sun W, Matthews EA, Nicolas V, Schoch S, Dietrich D. NG2 glial cells integrate synaptic input in global and dendritic calcium signals. Elife. 2016;5:e16262. Published 2016 Sep 19. doi:10.7554/eLife.16262

Surges R, Brewster AL, Bender RA, Beck H, Feuerstein TJ, Baram TZ. Regulated expression of HCN channels and cAMP levels shape the properties of the h current in developing rat hippocampus. Eur J Neurosci. 2006;24(1):94-104. doi:10.1111/j.1460-9568.2006.04880.x

Szatkowski M, Barbour B, Attwell D. Non-vesicular release of glutamate from glial cells by reversed electrogenic glutamate uptake. Nature. 1990;348(6300):443-446. doi:10.1038/348443a0

Tamura Y, Kataoka Y, Cui Y, Takamori Y, Watanabe Y, Yamada H. Multi-directional differentiation of doublecortin- and NG2-immunopositive progenitor cells in the adult rat neocortex in vivo. Eur J Neurosci. 2007;25(12):3489-3498. doi:10.1111/j.1460-9568.2007.05617.x

Tan AM, Zhang W, Levine JM. NG2: a component of the glial scar that inhibits axon growth. J Anat. 2005;207(6):717-725. doi:10.1111/j.1469-7580.2005.00452.x

Tang X, Taniguchi K, Kofuji P. Heterogeneity of Kir4.1 channel expression in glia revealed by mouse transgenesis. Glia. 2009;57(16):1706-1715. doi:10.1002/glia.20882

Tang AH, Chen H, Li TP, Metzbower SR, MacGillavry HD, Blanpied TA. A trans-synaptic nanocolumn aligns neurotransmitter release to receptors. Nature. 2016;536(7615):210-214. doi:10.1038/nature19058

Tekki-Kessaris N, Woodruff R, Hall AC, et al. Hedgehog-dependent oligodendrocyte lineage specification in the telencephalon. Development. 2001;128(13):2545-2554. doi:10.1242/dev.128.13.2545

Thyssen A, Hirnet D, Wolburg H, Schmalzing G, Deitmer JW, Lohr C. Ectopic vesicular neurotransmitter release along sensory axons mediates neurovascular coupling via glial calcium signaling. Proc Natl Acad Sci U S A. 2010;107(34):15258-15263. doi:10.1073/pnas.1003501107

Tong XP, Li XY, Zhou B, et al. Ca(2+) signaling evoked by activation of Na(+) channels and Na(+)/Ca(2+) exchangers is required for GABA-induced NG2 cell migration. J Cell Biol. 2009;186(1):113-128. doi:10.1083/jcb.200811071

Trapp BD, Nishiyama A, Cheng D, Macklin W. Differentiation and death of premyelinating oligodendrocytes in developing rodent brain. J Cell Biol. 1997;137(2):459-468. doi:10.1083/jcb.137.2.459

Trotter J, Karram K, Nishiyama A. NG2 cells: Properties, progeny and origin. Brain Res Rev. 2010;63(1-2):72-82. doi:10.1016/j.brainresrev.2009.12.006

Trueta C, De-Miguel FF. Extrasynaptic exocytosis and its mechanisms: a source of molecules mediating volume transmission in the nervous system. Front Physiol. 2012;3:319. Published 2012 Sep 4. doi:10.3389/fphys.2012.00319

Tsaur ML, Chou CC, Shih YH, Wang HL. Cloning, expression and CNS distribution of Kv4.3, an A-type K+ channel alpha subunit. FEBS Lett. 1997;400(2):215-220. doi:10.1016/s0014-5793(96)01388-9

Usowicz MM, Gallo V, Cull-Candy SG. Multiple conductance channels in type-2 cerebellar astrocytes activated by excitatory amino acids. Nature. 1989;339(6223):380-383. doi:10.1038/339380a0

van Tilborg E, de Theije CGM, van Hal M, et al. Origin and dynamics of oligodendrocytes in the developing brain: Implications for perinatal white matter injury. Glia. 2018;66(2):221-238. doi:10.1002/glia.23256

Vautier F, Belachew S, Chittajallu R, Gallo V. Shaker-type potassium channel subunits differentially control oligodendrocyte progenitor proliferation. Glia. 2004;48(4):337-345. doi:10.1002/glia.20088

Vélez-Fort M, Audinat E, Angulo MC. Functional alpha 7-containing nicotinic receptors of NG2-expressing cells in the hippocampus. Glia. 2009;57(10):1104-1114. doi:10.1002/glia.20834

Vélez-Fort M, Maldonado PP, Butt AM, Audinat E, Angulo MC. Postnatal switch from synaptic to extrasynaptic transmission between interneurons and NG2 cells. J Neurosci. 2010;30(20):6921-6929. doi:10.1523/JNEUROSCI.0238-10.2010

Viaene AN, Petrof I, Sherman SM. Activation requirements for metabotropic glutamate receptors. Neurosci Lett. 2013;541:67-72. doi:10.1016/j.neulet.2013.02.004

Wadel K, Neher E, Sakaba T. The coupling between synaptic vesicles and Ca2+ channels determines fast neurotransmitter release. Neuron. 2007;53(4):563-575. doi:10.1016/j.neuron.2007.01.021

Wahl-Schott C, Biel M. HCN channels: structure, cellular regulation and physiological function. Cell Mol Life Sci. 2009;66(3):470-494. doi:10.1007/s00018-008-8525-0

Wake H, Ortiz FC, Woo DH, Lee PR, Angulo MC, Fields RD. Nonsynaptic junctions on myelinating glia promote preferential myelination of electrically active axons. Nat Commun. 2015;6:7844. Published 2015 Aug 4. doi:10.1038/ncomms8844

Walz W. Chloride/anion channels in glial cell membranes. Glia. 2002;40(1):1-10. doi:10.1002/glia.10125

Wang D, Hiesinger PR. The vesicular ATPase: a missing link between acidification and exocytosis. J Cell Biol. 2013;203(2):171-173. doi:10.1083/jcb.201309130

Wang C, Pralong WF, Schulz MF, et al. Functional N-methyl-D-aspartate receptors in O-2A glial precursor cells: a critical role in regulating polysialic acid-neural cell adhesion molecule expression and cell migration. J Cell Biol. 1996;135(6 Pt 1):1565-1581. doi:10.1083/jcb.135.6.1565

Wang W, Gao XF, Xiao L, Xiang ZH, He C. K(V)7/KCNQ channels are functionally expressed in oligodendrocyte progenitor cells. PLoS One. 2011;6(7):e21792. doi:10.1371/journal.pone.0021792

Wang W, Putra A, Schools GP, et al. The contribution of TWIK-1 channels to astrocyte K(+) current is limited by retention in intracellular compartments. Front Cell Neurosci. 2013;7:246. Published 2013 Dec 9. doi:10.3389/fncel.2013.00246

Weerth SH, Holtzclaw LA, Russell JT. Signaling proteins in raft-like microdomains are essential for Ca2+ wave propagation in glial cells. Cell Calcium. 2007;41(2):155-167. doi:10.1016/j.ceca.2006.06.006

Wierenga CJ, Becker N, Bonhoeffer T. GABAergic synapses are formed without the involvement of dendritic protrusions. Nat Neurosci. 2008;11(9):1044-1052. doi:10.1038/nn.2180

Wigley R, Butt AM. Integration of NG2-glia (synantocytes) into the neuroglial network. Neuron Glia Biol. 2009;5(1-2):21-28. doi:10.1017/S1740925X09990329

Williamson AV, Compston DA, Randall AD. Analysis of the ion channel complement of the rat oligodendrocyte progenitor in a commonly studied in vitro preparation. Eur J Neurosci. 1997;9(4):706-720. doi:10.1111/j.1460-9568.1997.tb01419.x

Wu LG, Borst JG. The reduced release probability of releasable vesicles during recovery from short-term synaptic depression. Neuron. 1999;23(4):821-832. doi:10.1016/s0896-6273(01)80039-8

Xie M, Lynch DT, Schools GP, Feustel PJ, Kimelberg HK, Zhou M. Sodium channel currents in rat hippocampal NG2 glia: characterization and contribution to resting membrane potential. Neuroscience. 2007;150(4):853-862. doi:10.1016/j.neuroscience.2007.09.057

Yamagata A, Goto-Ito S, Sato Y, et al. Structural insights into modulation and selectivity of transsynaptic neurexin-LRRTM interaction. Nat Commun. 2018;9(1):3964. Published 2018 Sep 27. doi:10.1038/s41467-018-06333-8

Yoo AS, Krieger C, Kim SU. Process extension and intracellular Ca2+ in cultured murine oligodendrocytes. Brain Res. 1999;827(1-2):19-27. doi:10.1016/s0006-8993(99)01282-2

Young KM, Psachoulia K, Tripathi RB, et al. Oligodendrocyte dynamics in the healthy adult CNS: evidence for myelin remodeling. Neuron. 2013;77(5):873-885. doi:10.1016/j.neuron.2013.01.006

Yuan X, Eisen AM, McBain CJ, Gallo V. A role for glutamate and its receptors in the regulation of oligodendrocyte development in cerebellar tissue slices. Development. 1998;125(15):2901-2914. doi:10.1242/dev.125.15.2901

Yuan X, Chittajallu R, Belachew S, Anderson S, McBain CJ, Gallo V. Expression of the green fluorescent protein in the oligodendrocyte lineage: a transgenic mouse for developmental and physiological studies. J Neurosci Res. 2002;70(4):529-545. doi:10.1002/jnr.10368

Zhang Y, Chen K, Sloan SA, et al. An RNA-sequencing transcriptome and splicing database of glia, neurons, and vascular cells of the cerebral cortex [published correction appears in J Neurosci. 2015 Jan 14;35(2):846-6]. J Neurosci. 2014;34(36):11929-11947. doi:10.1523/JNEUROSCI.1860- 14.2014

Zhou Q, Xiao M, Nicoll RA. Contribution of cytoskeleton to the internalization of AMPA receptors. Proc Natl Acad Sci U S A. 2001;98(3):1261-1266. doi:10.1073/pnas.98.3.1261

Zhou M, Schools GP, Kimelberg HK. Development of GLAST(+) astrocytes and NG2(+) glia in rat hippocampus CA1: mature astrocytes are electrophysiologically passive. J Neurophysiol. 2006;95(1):134-143. doi:10.1152/jn.00570.2005

Zhou M, Xu G, Xie M, et al. TWIK-1 and TREK-1 are potassium channels contributing significantly to astrocyte passive conductance in rat hippocampal slices. J Neurosci. 2009;29(26):8551-8564. doi:10.1523/JNEUROSCI.5784-08.2009

Zhu X, Hill RA, Nishiyama A. NG2 cells generate oligodendrocytes and gray matter astrocytes in the spinal cord. Neuron Glia Biol. 2008;4(1):19-26. doi:10.1017/S1740925X09000015

Zhu X, Hill RA, Dietrich D, Komitova M, Suzuki R, Nishiyama A. Age-dependent fate and lineage restriction of single NG2 cells. Development. 2011;138(4):745-753. doi:10.1242/dev.047951

Ziskin JL, Nishiyama A, Rubio M, Fukaya M, Bergles DE. Vesicular release of glutamate from unmyelinated axons in white matter. Nat Neurosci. 2007;10(3):321-330. doi:10.1038/nn1854

Zonouzi M, Renzi M, Farrant M, Cull-Candy SG. Bidirectional plasticity of calcium-permeable AMPA receptors in oligodendrocyte lineage cells. Nat Neurosci. 2011;14(11):1430-1438. Published 2011 Oct 9. doi:10.1038/nn.2942

Zucker RS, Regehr WG. Short-term synaptic plasticity. Annu Rev Physiol. 2002;64:355-405. doi:10.1146/annurev.physiol.64.092501.114547